2017

Capillary Assembly Of Microparticles On Curved Fluid Interfaces

Iris Bi Liu
University of Pennsylvania, liubi@seas.upenn.edu

Recommended Citation

Liu, Iris Bi, "Capillary Assembly Of Microparticles On Curved Fluid Interfaces" (2017). *Publicly Accessible Penn Dissertations*. 2436.
https://repository.upenn.edu/edissertations/2436

Capillary Assembly Of Microparticles On Curved Fluid Interfaces

Abstract

There's a great interest in studying particle assembly on fluid interfaces for their properties to stabilize droplets in food, cosmetics, and oil industry, and to form permeable capsules in pharmaceutical industry. Capillary interaction holds tremendous promise as a tool to orient and assemble microparticles on interfaces between two immiscible fluids. Microparticles trapped at an interface deform the interface around them due to particle geometry, surface roughness, external fields and body forces. When particle deformations overlap, capillary interaction arise to minimize the interfacial deformation, hence minimizing energy. In literature, anisotropic shaped particles has been reported that their interactions depend strongly on the particle shape and curvature fields where particles adsorb can orient and attract particles to high curvature regions. However, less is known about particles of other shapes that don't disturb the interface as much as those anisotropic particles. In my thesis, I aim to use curvature field as a means to direct assemblies of particles with less pronounced deformation on interfaces. On curved oil-water interfaces, I study capillary attraction of microdisks and spheres that are pinned at the three-phase contact line due to surface roughness. These particles have radius much smaller comparing to the radius of curvature; they induce nanometric deformation on the interface and still create significant interface distortion and capillary interactions. To understand structure formation, I develop theory for pair interactions of particles on curved interfaces where capillary curvature interaction competes with particle pair interaction. Furthermore, I delve into interactions of large microdisks with curvature fields in both experiments and theory to explore capillary repulsion owing to the interaction of higher order modes with curvature fields. Lastly, I show the elastocapillary interactions of microcylinders on a thin film of uniform nematic liquid crystals. In all the studies described above, interface curvature, in particular, finite deviatoric curvature plays a central role in assembly and in guiding structure formation. The concepts studied here are fundamental and provide guidance in understanding, building, and designing colloidal structures with functionalities that have potential applications in various fields.

Degree Type
Dissertation

Degree Name
Doctor of Philosophy (PhD)

Graduate Group
Chemical and Biomolecular Engineering

First Advisor
Kathleen J. Stebe

Keywords
Anisotropic particles, Capillarity, Colloids

Subject Categories
Chemical Engineering

CAPILLARY ASSEMBLY OF MICROPARTICLES ON CURVED FLUID INTERFACES

Iris Bi Liu

A DISSERTATION

in

Chemical and Biomolecular Engineering

Presented to the Faculties of the University of Pennsylvania

in

Partial Fulfillment of the Requirements for the

Degree of Doctor of Philosophy

2017

Supervisor of Dissertation

Kathleen J. Stebe,
Richer and Elizabeth Goodwin Professor of Engineering and Applied Science

Graduate Group Chairperson

John C. Crocker, Professor of Chemical and Bimolecular Engineering

Dissertation Committee

Tobias Baumgart, Associate Professor in Physical & Biological Chemistry

Daeyeon Lee, Professor of Chemical and Biomolecular Engineering

Ravi Radhakrishnan, Professor of Bioengineering

CAPILLARY ASSEMBLY OF MICROPARTICLES ON CURVED FLUID INTERFACES

ACKNOWLEDGEMENT

I would like to sincerely thank my thesis advisor Prof. Kathleen Stebe for her guidance, enthusiasm, dedication and time throughout my doctoral studies. Without her vision and curiosity, my knowledge would not have progressed to allow me the intellectual foundation and ability to work with detail, thought, and rigor.

I would like to thank my committee members, Drs. Tobias Baumgart, Daeyeon Lee, and Ravi Radhakrishnan. It has been helpful to have a committee composed of excellent scientists that are not only interested in my thesis work, but also served as mentors in my career preparation.

To all the past and present members of the Stebe Lab, I am grateful for all of your help during the past five years. I would like to sincerely thank Nima Sharifi-Mood, Lu Yao and Giulia Bigazzi for being excellent and supportive collaborators in the capillarity studies. I would also like to thank Mohamed A. Gharbi, Francesca Serra, Yimin Luo, Nathan Bade, and Yu Xia and Hye-Na Kim from Shu Yang's Lab for being productive collaborators in the liquid crystal projects. I would like to thank my collaborators from the Kumar Lab, Denise Wong and Edward Steager for always being thoughtful in the robotics projects. I would also like to extend my acknowledgement to Tianyi Yao and Sambeeta Das who will continue this collaboration between our group and the robotics group. I am especially appreciative of Drs. Randall Kamien, Shu Yang and Vijay Kumar for the invaluable discussions and innovative ideas.

I would like to thank all my amazing friends in Philadelphia, with whom I shared many memorable moments filled with laughters, music, food, and drinks. Special thanks to my dearest officemates, Ningwei Li and Liana Vaccari, for making my graduate school experience more enjoyable.

My greatest support has been from my family, with special acknowledgements to my parents and grandparents. I am very grateful for your support, encouragement and understanding. I want to thank my cat, Hebe, for being really fat and cozy. Finally, I would like to thank my fiancé, Erte Xi, for your love and support; none of this would been possible without you.

ABSTRACT

CAPILLARY ASSEMBLY OF MICROPARTICLES ON CURVED FLUID INTERFACES

Iris Bi Liu

Kathleen J. Stebe

There's a great interest in studying particle assembly on fluid interfaces for their properties to stabilize droplets in food, cosmetics, and oil industry, and to form permeable capsules in pharmaceutical industry. Capillary interaction holds tremendous promise as a tool to orient and assemble microparticles on interfaces between two immiscible fluids. Microparticles trapped at an interface deform the interface around them due to particle geometry, surface roughness, external fields and body forces. When particle deformations overlap, capillary interaction arise to minimize the interfacial deformation, hence minimizing energy. In literature, anisotropic shaped particles has been reported that their interactions depend strongly on the particle shape; and curvature fields where particles adsorb can orient and attract particles to high curvature regions. However, less is known about particles of other shapes that don't disturb the interface as much as those anisotropic particles. In my thesis, I aim to use curvature field as a means to direct assemblies of particles with less pronounced deformation on interfaces. On curved oil-water interfaces, I study capillary attraction of microdisks and spheres that are pinned at the three-phase contact line due to surface roughness. These particles have radius much smaller comparing to the radius of curvature; they induce nanometric deformation on the interface and still create significant interface distortion and capillary interactions. To understand structure formation, I develop theory for pair interactions of particles on curved interfaces where capillary curvature interaction competes with particle pair interaction. Furthermore, I delve into interactions of large microdisks with curvature fields in both experiments and theory to explore capillary repulsion owing to the interaction of higher order modes with curvature fields. Lastly, I show the elastocapillary interactions of microcylinders on a thin film of uniform nematic

liquid crystals. In all the studies described above, interface curvature, in particular, finite deviatoric curvature plays a central role in assembly and in guiding structure formation. The concepts studied here are fundamental and provide guidance in understanding, building, and designing colloidal structures with functionalities that have potential applications in various fields.

TABLE OF CONTENTS

LIST OF ILLUSTRATIONS

CHAPTER 1 : Introduction

1.1. Motivation

Over the past decade, the advent of complex colloids as building blocks has fueled intense interest in their organization and assembly to form new materials [1]. Anisotropic colloids with non-spherical shapes or patchy surfaces offer important degrees of freedom, including complex, directionally dependent potentials [1, 2]. Sophisticated assembly schemes include design of particle shape and chemistry to favor the formation of particular superstructures. For example, colloid shape can be designed to assemble into complex crystalline structures via emergent interactions owing to features like sharp edges and planar facets [3, 4], or to interact specifically via lock-and-key interactions [5]. Colloidal surface chemistry can be tailored, for example, via grafting of DNA [6, 7, 8, 9, 10] or tailored wetting [11, 12, 13, 14] to drive particular structure formation. These examples often exploit weak, $O(k_BT)$, interactions to direct assembly. In other modes of directed assembly, applied electro-magnetic fields guide assembly. Particle interactions with the field and with neighboring particles are typically very strong, and the resulting structures are often trapped. Particles or their assemblies orient and move along field lines to form superstructures with symmetries coupled to the field itself. Examples include para- or ferromagnetic colloids chaining along magnetic fields gradients [15, 16, 17] and dipolar particles chaining in electric field gradients [18, 19]. In our research, we focus on fields which can direct colloid assembly that rely on energy landscapes in confined soft matter. Examples include interface-shape mediated capillary energy fields for particles on fluid interfaces [20], membrane-shape mediated fields for colloids on lipid bilayer membranes [21], and elastic energy fields for colloids in confined nematic liquid crystals [22, 23, 24, 25]. These fields are remarkably versatile in their ability to guide microparticles into well defined structures. Furthermore, since they depend on the configuration of the soft matter in which they assemble, which can be dynamically tuned, they are routes to reconfigurable structures.

In this chapter, we discuss capillary interactions between microparticles at fluid interfaces. Classically, colloids trapped at fluid interfaces have been exploited to stabilize emulsions and foams [26]. The colloids can bring added functionality, for example, as catalysts [27] or as responsive structures to dynamically (de)stabilize emulsions [28]. Particles at interfaces can form disordered structures [29] or ordered monolayers [30]. For ordered systems, interface curvature imposes topological constraints [31, 32, 33]. Electrostatic interactions between particles are known to play important roles in structure formation at interfaces, as has been widely discussed [34, 35, 36, 37]. There are several excellent reviews that address these topics, which are outside the scope of this thesis [38, 39].

At the scale of hundreds of microns to millimeters, there are many familiar examples of capillary interactions. In nature, "water striders" exploit surface tension to support their weight, and propel themselves using hydrophobic legs [40]. The oft-cited Cheerios effect is another example, in which pieces of breakfast cereal cluster on the surface of a bowl of milk [41]. The heavy pieces distort the interface around them, and interact to lower the interfacial and gravitational potential energies [42, 43], although details in the interface deformation around the morsels of cereal probably play important roles in the near field. By dynamically tuning the interface around them, whirligig beetles raft to form chains and other structures [44], and waterlily leaf beetles larvae move along curved menisci [45]. These examples show that capillary interactions are highly shape dependent. The concept of designing particle shape to interact specifically was explored in an exciting body of work at this scale decades ago [46, 47, 48]. Particles were designed with faceted shapes; some facets were well wet, others were not. At fluid interfaces, to minimize the excess area, they assembled to bring well-wet facets in contact, and poorly wet facets in contact, to form well defined structures.

In thesis chapter, we focus on capillary interactions as a means of microparticle assembly. We focus on interactions between colloids up to tens of microns, including disks, spheres, cylinders and ellipsoids. When microparticles are introduced to the interface by spreading or sedimentation from a dense suspension, they can become trapped in disordered layers owing to the strength of near field capillary interactions between them to form a colloidal monolayer membrane. However, if particles are sparse, or are introduced by sequential addition, they can assemble in preferred configurations to form a range of structures. Furthermore, at this length scale, interface curvature acts like an external field; particles move along curvature gradient lines to particular sites and form structures related to the underlying curvature gradients. Thus, at the microscale, complex structures can be formed even from simply shaped particles without complex, tailored wetting conditions.

Here, we describe key concepts in the underlying physics of particles at fluid interfaces, drawing in part on notes prepared for the summer school 2015 International School of Physics "Enrico Fermi"[49]. We review recent advances in the literature, and identify open issues and areas of ongoing research in the field. This review will be published in the Annual Review of Condensed Matter Physics.

1.2. Simplifications owing to particle size

Capillary interactions occur between microparticles trapped at fluid interfaces as they move to minimize the interfacial area, or, in the event of contact line motion, the sum of the energies owing to interface area and wetting energies. These interactions are determined by the wetting configuration of the particle and the shape of the interface around the particle. Typically, because of their microscopic radii a, several forces or stresses can be neglected, simplifying analysis of the particle interaction. We enumerate several of these effects here.

(i) Particle weight or buoyancy can typically be neglected, i.e., the Bond number:

$$Bo = \rho g a^2 / \gamma \ll 1, \tag{1.1}$$

where γ is the surface tension, $\Delta\rho$ is the difference in fluid densities, and g is the acceleration due to gravity.

(ii) Particle inertia can typically be neglected. Once attached to fluid interfaces, particles typically move in creeping flow, with Reynolds number:

$$Re = \rho ua/\mu \ll 1, \tag{1.2}$$

where μ is a characteristics viscosity of the fluids near the interface and u is the particle velocity. In this case, the sum of forces on the particles is zero.

(iii) The interface shape is typically independent of particle velocity. The magnitude of viscous stresses compared to surface tension is negligible, with capillary number:

$$Ca = \mu u/\gamma \ll 1. \tag{1.3}$$

This allows quasi-static analysis; at any instant in time, capillary interactions are determined by the interface shape, which is determined only by the particle locations and contact line configurations.

(iv) Capillary interactions are often so strong that Brownian effects are negligible, that is, the Péclet number,

$$Pe = Ua/D \ll 1, \tag{1.4}$$

where D is the Stokes-Einstein diffusivity of the particle in the interface, and U is the characteristic velocity of particle migration. In this limit, in creeping flow, capillary forces are balanced by viscous drag. This equality allows particle paths to be analyzed to find energy lost to viscous dissipation, and to infer capillary energy landscapes along those paths.

(v) Particles can deform the interface, with distortions that decay over distances comparable to the particle radius. In analysis, the height h of the interface around the particle above a reference plane tangent to the interface is often described in a Monge gauge, i.e., interface height $h(\mathbf{r})$ is a single valued function, where $\mathbf{r}$ is a position vector on the interface. Interface slopes are often assumed small compared to unity. In this limit, the shape of the interface is governed by

$$\nabla^2 h = \frac{\Delta P}{\gamma}, \tag{1.5}$$

where ΔP is the pressure difference evaluated at the interface. For constant mean curvature interfaces, the interface obeys:

$$\nabla^2 h = 0. \tag{1.6}$$

There is, however, a body of work for particles on curved interfaces in which the particle-sourced distortions are assumed to decay slowly compared to the radius of curvature [50, 51], or to move along interfaces of finite slope [52]. We do not address those limits here.

In the following sections, we discuss theory for particles at interfaces and review key findings. While we refer to liquid-vapor interfaces, the theory applies equally to interfaces between immiscible fluids. We discuss, in turn, isolated particles, pair interactions on planar interfaces and particles at curved fluid interfaces.

1.3. Trapping of isolated particles on planar interfaces

Consider a particle in suspension near a planar fluid interface. When the particle attaches to the interface, it eliminates a patch of solid-liquid contact ΔA_{SL} and makes a hole in the interface of area ΔA_{LV}. Furthermore, it can make distortions in the surrounding interface with area δA. The net energy change or trapping energy is:

$$\Delta E = (\gamma_{SL} - \gamma_{SV})\Delta A_{SL} + \gamma \Delta A_{LV} + \gamma \delta A, \tag{1.7}$$

where γ_{SL} and γ_{SV} are the surface energies of the solid-liquid and solid-vapor surfaces. When the trapping energy is large compared to $k_B T$, the particle is trapped, i.e., it cannot spontaneously leave the interface. We will discuss the trapping energy for two scenarios shown in Figure 1.1.

1.3.1. Trapping energy for a sphere at equilibrium

The case of a perfect sphere at equilibrium on a planar interface with contact angle θ_0 is an important ideal limit. The particle can attach without deforming the surrounding interface, so $\delta A = 0$, and the contact line is simply a circle in the plane of the interface [30]. The trapping energy is:

$$\Delta E = -\gamma \pi a^2 (1 - |\cos\theta_0|)^2, \tag{1.8}$$

where θ_0 is defined by the balance of the surface energies tensions given by the Young's equation,

$$\cos\theta_0 = \frac{\gamma_{SV} - \gamma_{SL}}{\gamma}. \tag{1.9}$$

By attaching, the particle reduces the area of the liquid vapor interface, lowering the system energy. This effect is modulated by the particle wetting properties. The trapping energy is remarkably large. For example, for air-water interfaces, the surface tension is $\gamma = 72\ mN/m$ or 18 k_BT/nm^2. Typical trapping energies for microparticles can be $10^5 - 10^6\ k_BT$.

1.3.2. Contact line pinning

This simple picture is complicated by contact line pinning on nanoscopic sites of roughness or chemical heterogeneity, for which there is now strong experimental evidence, even for simple, apparently homogeneous spherical polystyrene microparticles [53]. Pinned contact lines alter trapping energies fundamentally, as particles with undulated contact lines distort the interface around them, so $\delta A \neq 0$. The implications of contact line distortion on isolated trapped particles are still being resolved [53, 54, 55]. For isolated particles, contact line pinning changes the trapping energy by the amount $\gamma\delta A$; this is termed a self-energy contribution [39]. As we discuss below, particle-sourced interface distortions are the source of capillary pair interactions. Here, we review recent literature on contact line pinning for particles at interfaces.

Spherical microparticle attachment to the interface occurs via a rapid snap-in event, followed by a slow wetting as the contact line moves toward equilibrium [53, 55, 56, 57, 58]. Snap-in includes a rapid opening or breaching of the interface, and the formation of a contact line on the particle surface. Immediately after snap-in, particles oscillate owing to inertia associated with this event. In experiments with glass microbeads with various surface chemistries and radii, snap-in occurred within 0.1ms, reflecting a balance of inertia and surface tension independent of particle wetting; the snap-in force however, depended on particle size and wetting [56]. Once the oscillations end, the contact line exhibits slow, glassy dynamics as it approaches equilibrium [53, 55]. Contact line motion occurs with negligible capillary number Ca based on contact line velocity, so viscous effects, typically important for contact line motion in dynamic spreading are negligible [59] . Using holographic imaging to track the position of a polystyrene colloid near a decane-water interface, the contact line was inferred to move slowly, logarithmically in time for particles close to equilibrium. Because of these slow kinetics, similar particles with differing breach times have different wetting positions in the interface. The observed logarithmic relaxation is consistent with a model in which the contact line is pinned at nanoscopic heterogeneities with hopping frequencies given in terms of Blake-Haynes model from molecular kinetic theory [60]. Further analysis and supporting molecular dynamics simulation reveals contact line relaxations are initially exponential with a visco-capillary time scale, then exhibit slow logarithmic aging like that captured in experiments, and finally exhibit exponential decay to equilibrium, suggesting that the glassy dynamics end [57]. Recent studies of particles made of different materials show that the glassy contact line dynamics are generic, but the energy of pinning sites varies strongly for different materials as presented in Ref. [55].

Contact line pinning may have important dynamical consequences even for isolated particles attached at the interface; pinned states, and associated enhanced dissipation owing either to contact line hopping or interaction of the undulated interface with capillary waves were invoked in a recent study reporting unexpectedly high drag on Brownian particles adsorbed from suspension in air at air-water interfaces [54].

1.3.3. Trapping energy for a particle with a pinned contact line

For spherical particles with pinned contact lines on planar interfaces, there are several unknown aspects that complicate evaluation of the trapping energy. These include the unknown angle characterizing the degree of immersion of the particle in the fluid, θ_{tr}, the unknown contact line shape, and the associated area of particle-sourced deformation in the interface δA. In the limit of small slopes, the shape of the contact line can be decomposed into Fourier modes [61], and δA can be found by determining the height h of the interface around the particle above the reference plane and evaluating the associated area for each mode. The shape of the interface is given by a decaying multipole expansion expressed in a polar coordinate system (r, ϕ) in the plane of the interface with origin at the center of the hole made by the particle in the interface. Each order of this expansion is excited by the corresponding Fourier mode at the contact line:

$$h(r,\phi) = b_0 \ln r + \sum_{m=1}^{\infty} c_m r^{-m} \cos(m\phi + \alpha_m), \tag{1.10}$$

where α_m is the phase angle of mode m. Since body forces and torques on the particles are negligible, mechanical equilibrium requires that $b_0 = c_1 = 0$. Thus the quadrupolar distortion is the first surviving mode in the interface distortion [61]. Letting h_{qp} be the amplitude of this mode, the interface height to leading order is:

$$h(r,\phi) = h_{qp} \frac{a^2}{r^2} \cos 2\phi. \tag{1.11}$$

This term describes the long-range interface distortion from any particle with an undulated contact line; the existence of this mode gives rise to universal behavior between interacting particles in the far field, and for small particles at curved fluid interfaces.

To evaluate the trapping energy for a particle, δA must be evaluated. Dividing the particle-free interface into two domains, $I + P$, where the domain P is occupied by the particle after attachment, and the domain I is outside of the contact line (Fig. 1.2), the area can be evaluated in the limit of small slopes:

$$\delta A \approx \iint_I \frac{\nabla h \cdot \nabla h}{2} r \mathrm{d}r \mathrm{d}\phi = \pi h_{qp}^2. \tag{1.12}$$

The trapping energy for the particle can be evaluated:

$$\Delta E_{planar} = -\gamma \pi a^2 (1 - |\cos \theta_{tr}|)^2 + \gamma \pi h_{qp}^2. \tag{1.13}$$

The first term is similar to the equilibrium case except that the angle characterizing the degree of immersion in the trapped state θ_{tr} replaces θ_0. The second term is the 'self energy' of the particle, the energy cost associated with the area of the distortion around the particle. Similar terms appear from the higher order modes in the multipole expansion [61, 62].

1.3.4. Non-spherical particles

The contributions to the trapping energy remain the same for complex shaped particles. These include the energy decrease owing to the hole in the interface, modulated by the particle wetting energies, and the energy owing to the excess area of the interface distortion. The evaluation of each contribution is difficult for many reasons. The equilibrium wetting configuration of complex shaped particles cannot typically be derived analytically [63, 64, 65]. Thus, the size of the hole in the interface, the height of the particle, and the interface distortion must typically be found via simulation. Furthermore, contact line pinning occurs on these particles, so, while simulated equilibrium wetting configurations lend guidance, they do not suffice to predict the dynamic state of the interface and the particle. There are, however, important simplifications that can be made to make some progress. Pinned contact lines around non-spherical particles can be decomposed into Fourier modes; interface distortions can be described in multipole expansions. For elongated particles, an expansion in ellipsoidal coordinates for a particular particle aspect ratio is appropriate [66]. The quadrupolar modes in this coordinate accurately describes the far field interface shape for elongated particles [63].

1.3.5. Key findings for isolated particles

Anisotropically shaped microparticles attach to interfaces via a process related to that for spheres. However, the highly non-uniform dynamic contact angle along the contact line contour as the particle enters the interface gives interesting dynamics [67]. An ellipsoidal microparticle enters the interface via a rolling motion consistent with non-uniform displacement of contact line segments; segments with greater differences between the θ_{tr} and θ_0 moved faster. These observations imply that differing, time dependent surface deformations can be made by similar particles. Complex shaped particles, whether they are adsorbed from suspension or spread via solvents can assume a variety of configurations [63, 68, 69, 70, 71, 72]. As a crude guiding principle, isolated particles assume orientations in which they make the largest hole in the interface with greater probability; e.g. elongated particles have their long axes in the plane of the interface. Examples

Anisotropic microparticles can make very strong distortions in fluid interfaces that can be imaged via interferometry [63, 69] and compared to simulated equilibrium wetting configurations [68]. Distortions around prolate ellipsoids and cylinders have quadrupolar symmetry. Observed interface shapes agree well with the height of quadrupolar modes in elliptical coordinates within a few radii of contact with the particle [63, 65], a fact that facilitates analysis. In the very near field, however, only simulations capture details [73], in particular near features like sharp edges and corners. In most simulations [65, 74], equilibrium contact angles are assumed in the near field, in spite of the importance of pinned contact lines. Finer features also play a role, including particle roughness [75]. To investigate these effects, particles designed to form wavy contact lines with wavelength and amplitude small compared to the particle length have been studied [76]; the distortions made by the wavy features decay over distances similar to their wavelength and change the energy landscape only in the near field around the particle These will have implications in pair interactions.

Finally, while the quadrupole is the leading order distortion for the interface in the far field absent external forces, there are particle configurations that excite higher order modes, e.g. simulations of cuboid-shaped particles show that, in certain orientations, particles excite well-defined hexapolar modes in the interface [74].

1.3.6. Summary

Particles become trapped at planar fluid interfaces. Perfectly smooth spheres with equilibrium wetting conditions leave the interface around them unperturbed. However, particles with pinned contact lines, patchy wetting or non-spherical shapes distort the interface around them. The associated self-energies contribute to the trapping energy of the particle. Distortions due to various particle features decay at different distances from the particle. All particles make quadrupolar distortions in the far field; higher order modes owing to complex contact line shapes decay more rapidly. Within a few particle radii of contact, features like particle elongation become apparent; closer still, contact line waviness due to particle geometry, roughness or pinning and sharp edges play a role [76]. The distortion fields around microparticles at interfaces play a central role in pair interactions, as is discussed in section 1.4.1 below.

1.4. Pairs of particles on planar interfaces

Particles interact at fluid interfaces to minimize the interfacial area. Interactions between capillary multipoles are often likened to those between charge multipoles except that like charges attract. In this rubric, regions above the reference plane are positive while those below the reference plane are negative. When distortions h from neighboring particles overlap, particles orient and migrate so that regions with "like charge" overlap. In this way, the slope of the interface, and the area δA owing to the distortions, decreases. (We revisit the analogy to electrostatics in section 3.6.3, below.) As particles approach, different parts of their distortion fields interact depending on their separation distance. Interactions first occur because of their quadrupolar modes. Closer to contact, higher order modes, near field distortions, and the presence of corners and edges play roles. Furthermore, rearrangement of wetting configurations and contributions from the associated solid-fluid wetting energies can, in principle, play a role. All of these have been discussed in prior literature [61, 39, 65, 62, 64]. Therefore, we discuss main concepts and findings in only a cursory manner here, and refer the interested reader to those reviews for a more thorough treatment.

Below, we derive the capillary energy of interaction between two colloidal particles with pinned contact lines on an otherwise planar interface, using the method of reflections, and compare this to the exact solution in bipolar coordinates. This treatment differs from the seminal work in the literature [61] in that we do not adopt the superposition approximation.

1.4.1. Method of reflections

Particles 1 and 2 of radius a are separated by distance r_{12}, with $a/r_{12} \ll 1$ (see Fig. 1.3a). Both particles have pinned contact lines with quadrupolar modes of amplitude h_{qp}. In isolation, the shape of the interface around each colloid can be expressed in terms of polar coordinates (r_1, ϕ_1) and (r_2, ϕ_2) located at the centers of the particles:

$$h_1 = h_{qp}\frac{a^2}{r_1^2}\cos 2(\phi_1 - \alpha_1) \tag{1.14}$$

and

$$h_2 = h_{qp}\frac{a^2}{r_2^2}\cos 2(\phi_2 - \alpha_2), \tag{1.15}$$

where α_1 and α_2 denote the phase angles of particles with respect to the line connecting particle centers. A Taylor Series expansion of the distortion owing to particle 2 near particle

1 yields:

$$h_2 = h_2|_{\mathbf{r}_{12}} + \mathbf{r}_1 \cdot \nabla h_2|_{\mathbf{r}_{12}} + \mathbf{r}_1 \cdot \left.\frac{\nabla\nabla h_2}{2}\right|_{\mathbf{r}_{12}} \cdot \mathbf{r}_1 + ..., \tag{1.16}$$

where $\mathbf{r}_1$ is the position vector from the origin at particle 1 and $\mathbf{r}_{12}$ is the vector from the origin to particle 2. In the above expression, the first two terms are changes to the height and slope; absent body forces and torques, particle 1 adjusts its height and tilt to eliminate these terms. The third term is the curvature field created by particle 2 in the vicinity of particle 1. This term is the leading order distortion made by particle 2 near 1, and defines the far field distortion h_∞ for particle 1 [77, 78]. The shape of the interface around particle 1 in the plane tangent to the interface can be found by solving this boundary value problem:

$$\nabla^2 h_1 = 0, \tag{1.17}$$

with the boundary condition at the contact line:

$$h_1(r_1 = a) = h_{qp} \cos 2(\phi_1 - \alpha_1), \tag{1.18}$$

and in the far field:

$$h_1(r_1 \to \infty) = h_\infty = 3h_{qp}\frac{a^2}{r_{12}^4} r_1^2 \cos 2(\phi_1 + \alpha_2). \tag{1.19}$$

We find:

$$h_1 = 3h_{qp}\frac{a^2}{r_{12}^4} r_1^2 \cos 2(\phi_1 + \alpha_2) + \eta_1 \tag{1.20}$$

and

$$\eta_1 = h_{qp}\frac{a^2}{r_1^2} \cos 2(\phi_1 - \alpha_1) - 3h_{qp}\frac{a^2}{r_{12}^4}\frac{a^4}{r_1^2} \cos 2(\phi_1 + \alpha_2). \tag{1.21}$$

The disturbance η_1 includes the particle sourced term and an induced or reflected term "undoing" the curvature created by particle 2.

To calculate the area associated with this disturbance field δA_1 around particle 1, we evaluate:

$$\delta A_1 \approx \iint\limits_I \frac{\nabla h_1 \cdot \nabla h_1}{2} r_1 \mathrm{d}r_1 \mathrm{d}\phi_1 - \iint\limits_I \frac{\nabla h_\infty \cdot \nabla h_\infty}{2} r_1 \mathrm{d}r_1 \mathrm{d}\phi_1. \tag{1.22}$$

δA_1 contains three terms; the self energy that occurs for isolated particles, a pair interaction energy that depends on r_{12}, and a higher order term that makes negligible contributions to leading order. Taking the difference in energies for finite r_{12} and for infinite separations, the capillary energy for particle 1 interacting with particle 2 to leading order is:

$$\Delta E_1 = -6\gamma\pi {h_{qp}}^2 \frac{a^4}{r_{12}^4} \cos 2(\alpha_1 + \alpha_2). \tag{1.23}$$

Particle 2 has an identical contribution, so:

$$\Delta E = 2\Delta E_1 = -12\gamma\pi {h_{qp}}^2 \frac{a^4}{r_{12}^4} \cos 2(\alpha_1 + \alpha_2). \tag{1.24}$$

The interface shape can be solved exactly in bipolar coordinates [62, 79] for pinned quadrupolar contact lines on both particles. The result, however, includes changes in height and slope from the neighboring particle that are not present absent body forces and torques. By amending the boundary condition at the contact line to remove these effects, the interface height and the excess area around both particles 1 and 2, δA can be calculated analytically. The resulting interaction energy is compared to the pair interaction energy in Equation 1.24 in Figure 1.3b. The two solutions agree for particles more than a radius from contact. However, very near to contact, there is a deviation between the two solutions which indicates the importance of higher order reflections in the near field.

The pair interaction energy between particles predicts that particles attract only if they are in mirror-symmetric orientations i.e., $\alpha_1 + \alpha_2 = 0^\circ$ (Fig. 1.3c). Particles that are misaligned rotate to assume mirror symmetry, and then migrate. For common fluid interfaces, $\gamma \sim 10k_BT/nm^2$. Particles with contact line distortions as small as $2nm$ can have more than $10k_BT$ of interaction at center to center separations of several radii. Microparticles with rough surfaces, anisotropic shapes or patchy wetting can have contact lines with far larger amplitude modes. The attractive capillary force corresponding to the energy expression of Equation 1.24 $\sim r_{12}^{-5}$. For particles moving in creeping flow, this force is counterbalanced by viscous drag $\sim dr_{12}/dt$. This balance requires that particles move with a power law $r_{12} \sim (t_f - t)^{1/6}$ [68].

1.4.2. Key findings of interactions on planar interfaces

The strong deformation fields around anisotropic particles make them excellent vehicles for studying capillary interactions. Here we focus on ellipsoids and cylinders, and the role of particle roughness. The dynamics of microparticle assembly were first observed for ellipsoids at a oil-water interface a decade ago [68], motivating interest in ellipsoidal particle assembly [65, 66, 73, 80, 81]. The particles, with major axis $\sim 10\mu m$ and minor axes $\sim 2\mu m$ interacted over distances as great as six particle lengths with weakly Brownian trajectories in the far field, and well determined paths in the near field. Particles approached in either tip-to-tip and side-to-side configurations. For tip-to-tip interactions, the particles obeyed the expected power law for interacting polar quadrupoles in the far field. For side-to-side arrangements, a lower exponent was reported; subsequent detailed simulation shows that contributions from higher order modes are significant at separations as large as four particle lengths [73]. The capillary energy change along a trajectory, inferred from viscous dissipation, was very strong, $\sim 10^4 k_BT$. Particles assemble tip-to-tip for polystyrene particles or side-to-side for silica coated particles [68]. The existence of these preferred alignments is an interesting feature, as the theory described in section 1.4.1 does not predict this effect. Theory for pairs of interacting elliptical quadrupoles does predict mirror symmetric approaches, tip-to-tip assembly at contact, and rotation to side-to-side alignment after contact [63]. Detailed simulation of the interface between ellipsoids near contact also predicts side-to-side assembly [65, 73]. Thus, near field capillary interactions favor side-to-side arrangements. The tip-to-tip arrangement might be enforced by electrostatic repulsion, known to be significant for polystyrene particles at oil-water interfaces. Indeed, particles with scant surface charge (PMMA microparticles) assemble side-to-side [72]. Similar arrangements have been reported for diverse ellipsoidal shaped objects, including mosquito eggs [66] and whirligig beetles [44]. The mechanics of these structures is rich. Particles chained tip-to-tip rotate freely while maintaining contact, while chains of side-to-side particles can bend weakly under compression.

Crowded interfaces of ellipsoids also have interesting behavior that we describe only briefly. Simulation of weakly non-spherical particles assuming pairwise additivity suggests that even nanometric deviation from sphericity can drive capillary assembly of ellipsoids into a variety of structures that include dendritic-trapped configurations, rafts and hexagonal lattices [82]. The rheology of rafts of ellipsoidal particles in tip-to-tip assembly differs from sphere-laden interfaces; particle monolayers are elastic at low surface area fractions and yield via a series of flipping events under compression [83], with major implications in important processes like convective assembly within evaporating drops [29].

Cylindrical microparticles interact over distances comparable to ten particle lengths, with excellent agreement with the power law for interacting polar quadrupoles in the far field as presented in Ref. [63] If the particles are already oriented end-to-end, they maintain that alignment until contact. If however, they are oriented side-to-side, they rotate while maintaining mirror symmetry to assemble to form a straight and rigid dimer. On sparse interfaces, long chains comprised of many cylinders form.

The chains of cylinders are remarkably rigid, failing to bend or break even under significant torque applied by rotating them in a magnetic field. To understand this effect, cylindrical microparticles near contact were compared to ellipsoidal particles near contact in simulation

[65]. Cylinders were simulated in an end-to-end alignment, and then in arrangements where they rotated from that arrangement. The steric barrier posed by the particle's sharp edges and the associated rearrangements of the capillary bridge between the particles give rise to a strong energy barrier to rotation that enforces the rigid end-to-end alignment. These features are absent on ellipsoids, which can roll over each other freely near contact; the associated energy landscape indicates that the capillary bond between pairs of ellipsoids is elastic, so chains of side-to-side ellipsoids are flexible, whereas chains of cylinders should remain aligned until they snap under applied torque.

It is interesting to ask whether particles come to contact, and what would limit their proximity. In an early study, particle roughness was suggested as a source of repulsive capillary interactions. Wavy contact lines pinned on the rough sites would create local disturbances near the particle, important only in the very near field [75]. When neighboring particles approach, these disturbances would interact. If they matched perfectly, with identical wavelengths, phases and amplitudes, particles would attract. However, if they differ, as would be expected for random roughness, particles would be repelled. This concept was recently demonstrated using particles with wavy edges [76]. In the far field, these particles experience the usual capillary attraction. However, when distortions from the wavy contact lines overlap, particles with differing undulations are repelled.

1.4.3. Summary

Particles with pinned contact lines interact via capillarity over remarkable distances. Anisotropic particles align as they migrate to preferred configurations. In the near field, details in the particle shape play major roles in determining the strength of the interactions, the distance of closest approach. In his analysis of particle interactions in the far field, Stamou noted that one particle moved in the curvature field of its neighbor [61]. In principle, however, any means of pinning or distorting the interface far from the particle can create a curvature field. It is a natural extension to consider particles on curved interfaces. This subject is the focus of this thesis.

1.5. Outline of Thesis

My research has focused on microparticles on curved fluid interfaces. Fluid interfaces serve as platforms for particles to interact with each other and with the curvature field to form structures with well-defined alignment and orientation at predefined locations. Particles at fluid interfaces interact via capillary interactions which arise from the overlapping of the deformation fields that they create on the fluid interfaces. These interactions depend strongly on the particle properties, including particle geometry and surface properties, and the interface shape. In this dissertation, I combine experiments and theory to study the behavior of microparticles at curved fluid interfaces.

Chapter 2 focuses on the interaction of a microdisk with curvature field. Mircrodisks have pinned contact line at the interface due to surface roughness of the particles. The particle interaction with curvature field is sourced from the undulated contact line. Experimental results are compared against theory to provide insights on capillary curvature interactions.

Chapter 3 studies the interaction of a microsphere on a curved interface. Two cases are discussed for a microsphere interaction with curvature field: equilibrium contact angle and pinned contact line. Experimental results are reported to show microspheres have pinned contact line and have similar interaction with curvature field as microdisks.

In the above studies, the disks and spheres are small compared to the radius of the micropost used to create the interface curvature. In Chapter 4, I relax this limit: I observe and report rich interactions of the particles with the interface curvature field. Some particles are attracted to zones of high curvature, others stop at an equilibrium location, while others are repelled from regions of high curvature by curvature field. I report analysis to explain these experimental observations.

Chapter 5 highlights the interaction of a pair of particles on a curved fluid interface. A full derivation of the pair interaction energy is provided. Interestingly, the pair interaction is simply the summation of the particle-curvature interaction with the particle-particle interaction. The contributions depends strongly on the curvature field and the particles separation distance.

Chapter 6 shifts focus to cylindrical particles on the air- nematic liquid crystal interface. Liquid crystals introduce complexity to the study, as particle orientaiton is influence by elastic energies associated with distortions on the nematic liquid crystal director field. In this study, I explore the microcylinders behavior on both the uniform planar and curved nematic interfaces. Capillarity compete and couple with elasticity on the interface to guide particle assembly. Here, I summarize regions of dominance for capillarity and elasticity.

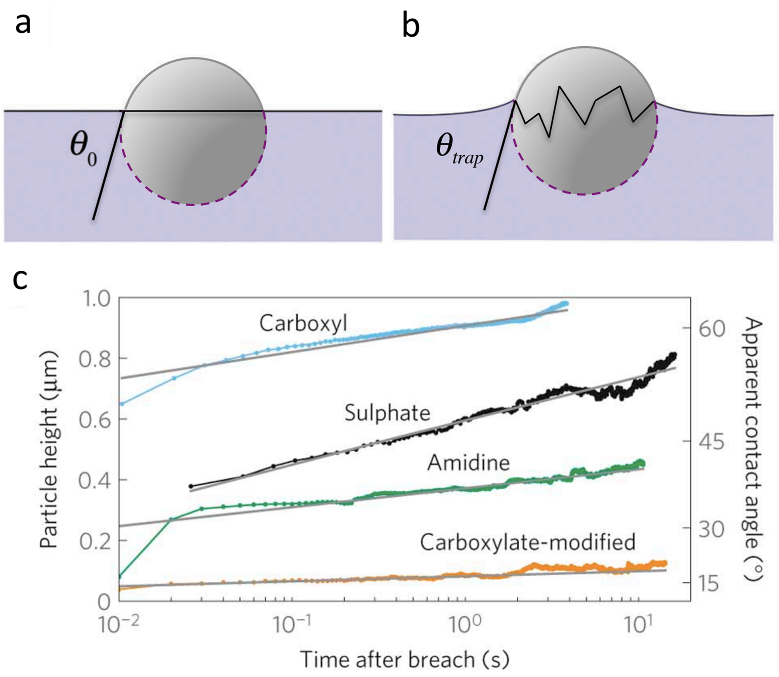

Figure 1.1: Particle trapped at a fluid interface. Schematic of particle adsorption on an interface with (a) an equilibrium contact angle, and (b) pinned contact line.

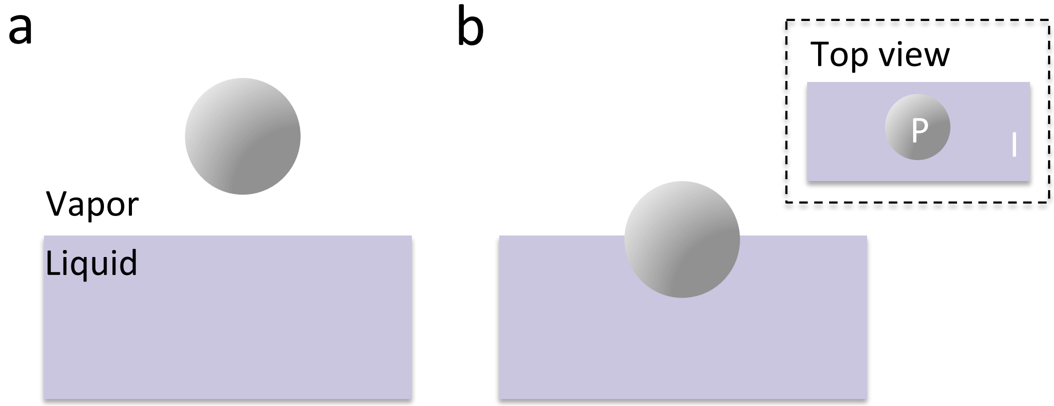

Figure 1.2: Schematic of a spherical particle (a) immersed in vapor phase and becomes (b) adsorbed to a vapor-liquid interface. Inset: top view of a particle (P, particle domain) on an interface (I).

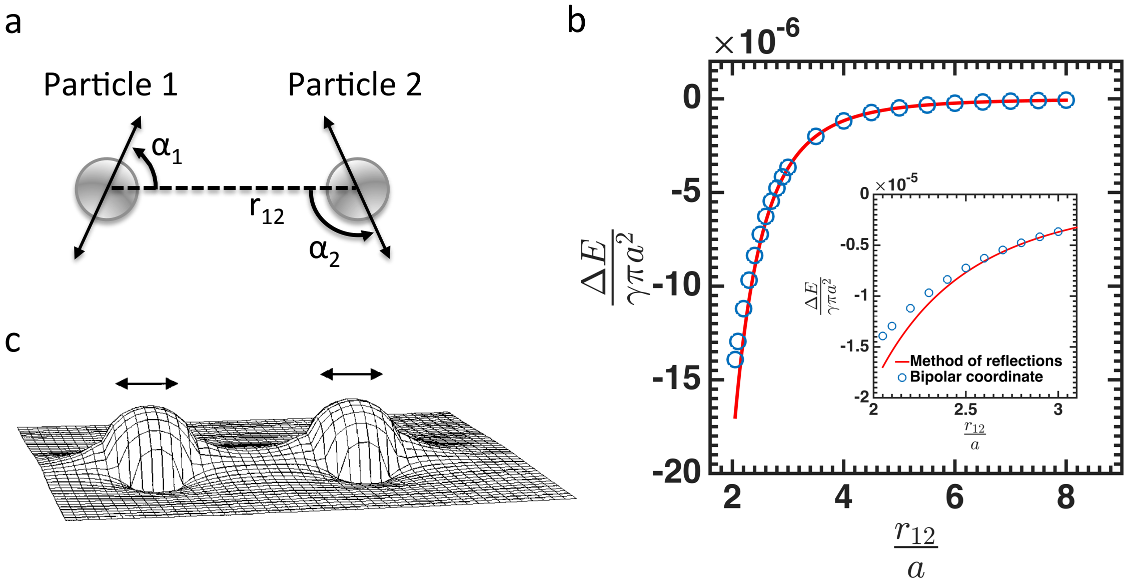

Figure 1.3: Schematic of pair of particles interacting with their quadrupoles. (a) Spheres separated by distance r_{12} align in mirror symmetric orientation where the doublesided arrows indicate the rise of the interface, and α_1 and α_2 define the phase angle for particle 1 and 2, respectively. (b) Non-dimensional interaction energy comparison between the method of reflections and the exact solution from bipolar coordinate calculation. Inset: Near field comparison of the two methods [49]. (c) A pair of interacting spheres with their quadrupoles co-aligned (rise-to-rise). Reprinted with permission from Reference [61] (https://doi.org/10.1103/PhysRevE.62.5263); copyright 2000 by the American Physical Society.

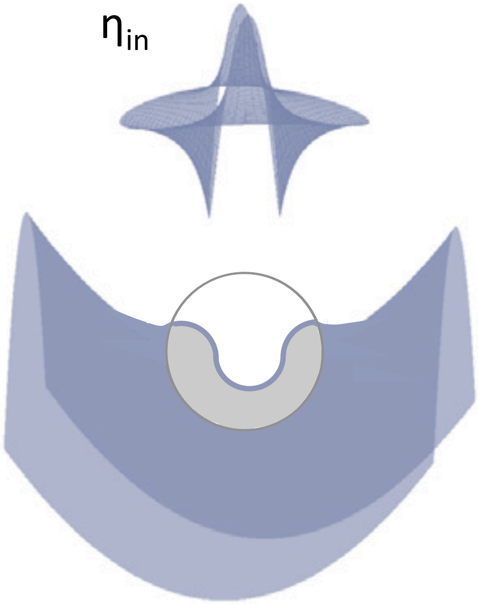

Figure 1.4: Schematic of a spherical particle with quadrupolar deformation on a curved interface where the particle-induced distortion is denoted η_{in}.

CHAPTER 2 : Curvature capillary attraction: Small disks at curved interfaces

2.1. Introduction

Capillary interactions are ubiquitous between microparticles at fluid interfaces. Classically, they are exploited in a wide range of technologies including stabilization of foams and Pickering emulsions [84] and in separations of materials in ore flotation [85]. Fundamentally, they provide insight into condensed matter physics, for example, the formation and evolution of 2D crystal structures [30, 86] and their topological constraints [32]. More recently, they are widely exploited in bottom up assembly schemes to organize particles for advanced materials applications [87].

Capillary interactions arise spontaneously between microparticles at interfaces. Typically, the effects of gravity are negligible compared to surface tension, i.e. the particle radius a is small compared to the capillary length based on the density of the fluid ρ, the interfacial tension γ, and the gravitational acceleration constant g, i.e. $\frac{a}{\sqrt{\frac{\gamma}{\rho g}}} \ll 1$. As reviewed in the Introduction to this thesis, on planar interfaces, capillary interactions are well understood [39, 64, 88, 89]. Particles adsorb and eliminate a patch of fluid interface. In addition, they perturb the shape and thereby increase the area of the interface around them if they have anisotropic surface energies [90], non-spherical shapes [68, 72, 91], or in principle, if they have spherical shapes but have contact lines pinned at some non-equilibrium position [61]. In the far field, when distortions from neighboring particles overlap, the area and therefore the energy of the interface typically decrease when the particles approach each other.

Capillary attraction in the limit of negligible gravity has been observed to orient and assemble Janus particles [90] and particles with complex shapes including ellipsoids [68, 72] and cylinders [68, 72, 91]. Rough particles also distort planar interfaces, creating disturbances which decay close to particle contact. The energies associated with these disturbances from neighboring particles can be attractive or repulsive. Far field capillary attraction and near field capillary repulsion can be used to define particle separation distances [75, 76].

There are important gaps in our understanding of curvature driven capillary migration. Fluid interfaces can be curved owing to confinement or body forces to display mean or deviatoric curvature fields that influence particle migration. Microparticles in the limit of negligible gravity have indeed been observed to migrate on curved interfaces. Cylindrical microparticles orient along principal axes and migrate to high curvature sites owing to their undulated contact lines [20]. A case of spherical micro particle migration in this limit has also been reported; the particle migrated along a curvature gradient to find an equilibrium position that is ascribed to a balance of capillary forces and weak gravitational forces [52]. From a theoretical perspective, the behavior of isotropic spheres with equilibrium wetting boundary conditions has been studied for several interface shapes, including interfaces with zero mean curvature [92], cylindrically-shaped interfaces [50], or interfaces with arbitrary curvatures [89, 93, 94]. In several of these theoretical studies, particles are predicted to migrate with curvature capillary energies which are quadratic in the deviatoric curvature field; in this work, we show that contributions of that order are identically zero for the case of pinned contact lines.

This limit may be broadly relevant. There is a growing body of evidence that colloidal particles can have pinned contact lines at fluid interfaces in experiment [53, 95, 96] and simulation [57, 97]. Here, we study migration of particles with pinned contact lines on interfaces with well-defined curvature fields, using a planar disk-shaped particle which pins the contact line at its sharp edges. On planar interfaces, the disks interact only weakly and only if they are in close proximity. When placed on curved interfaces, however, these particles experience significant capillary energies and move towards regions with higher curvature. Particle trajectories are highly reproducible and deterministic for isolated disks. Particles interact in the near field to form linear structures oriented along curvature gradients.

We derive a general theory for particles with pinned contact lines on a curved interface. Generally, by adsorbing to a fluid interface, a particle eliminates a patch of interface, replacing it with fluid-solid surfaces. The particle also creates a disturbance in order to satisfy its pinning boundary condition at the three phase contact line. For interfaces with finite mean curvature, this disturbance in interface height does work against the pressure jump at the interface. For a particle of roughly circular cross section, the pinned contact line shape can be described in terms of multipole expansion for the contact line height, with the leading order being the quadrupolar mode [61] (see Fig. 2.1(c) and (d)). For constant mean curvature interfaces, analysis predicts that a planar particle with a perfectly circular contact line will not migrate, and that planar particles with weak deviations from a circular contact line will migrate to regions of steepest curvature.

2.2. Experiments

Epoxy resin microdisks of radius $a = 5\mu m$ are fabricated using standard lithographic methods. A negative tone photoresist (SU-8 2002, MicroChem Corp.) was deposited onto a silicon wafer (Montco Silicon) by spin-coating. The photoresist was exposed to UV light (365 nm) on a tabletop mask aligner (OAI Model 100) through a photomask (Microtronics Inc., Fine Line Imaging). The samples then were heated using UV light to cure the polymer. Finally, the microdisks were released from the wafer via sonication.

Microdisks make only weak interface distortions on planar interfaces. Thus, when placed on planar interfaces, these particles fail to interact unless they are within ~ 10 radii of contact. We confirm that the disks have pinned contact lines by imaging the underside of a particle trapped in an interface (Fig. 2.2(a)). The image is acquired using a gel-trapping technique by placing a microparticle in the air aqueous interface of a warm ($50°C$) gellan solution which is then cooled to form a gel. PDMS is then poured over the particle, cross-linked, and lifted, making a negative mold of the interface and taking the particle with it. An SEM image of this assembly reveals that the particle pins the interface at its upper sharp edge. The disks are also rough on the nanometric scale; using an AFM (Bruker Icon) in tapping mode, we find the root mean square roughness over the surface area of the disks ranges from 18 to 32 nm (Fig. 2.2(b)).

To study particle migration, a host interface is formed with a well-defined curvature field using a technique reported previously [20] which we recapitulate briefly here. A curved oil-water interface is formed around a micropost of height H_m and radius R_m centered within a confining ring located several capillary lengths from the micropost. This structure is filled with water so that the contact line pins at the top of the micropost and the slope of the interface is $\psi \sim 15 - 18^\circ$ as measured using a goniometer (see Fig. 2.3(a)). The shape of the oil-water interface for distances from the micropost small compared to the capillary length obeys $h_0 = H_m - R_m \tan\psi \ln\frac{L}{R_m}$, where L is the radial distance measured from the micropost center. This interface (shown schematically in Fig. 2.3(b)) has zero mean curvature $H_0 = \frac{c_1+c_2}{2} = 0$, and deviatoric curvature $\Delta c_0 = c_1 - c_2$ which is finite and position dependent. The deviatoric curvature is greatest in magnitude close to the post, and decrease monotonically with distance from the post.

2.3. Results and Discussions

Disks are submerged in the oil phase, and allowed to sediment and attach to the interface. Particles, once attached, migrate up the curvature gradient along radial trajectories toward the micropost if they are isolated (Fig. 2.4(a)). Deviations from radial trajectories occur only for particles close to neighboring particles (within 10-15 radii) or close to disks that are already anchored on the micropost (Fig. 2.4(b)). Trajectories of isolated particles superpose when graphed in terms of (L, t_c), where t_c denotes time to contact defined as $t_c = t_0 - t$ and t_0 is the time when the disk reaches the edge of the post (Fig. 2.4(c)). The more complex trajectories owing to interaction with neighboring elements or floating aggregates are evident as deviations from the master L vs. t_c curve (see Fig. 2.4(d)).

Since the particle migrates in creeping flow, the capillary force on the particle is balanced by a drag force according to $F = C_D \mu a \frac{dL}{dt}$ where we adopt for C_D Lamb's drag coefficient for a disk on an interface [98] and the average viscosity of the two surrounding fluids μ, is used. The capillary energy ΔE is balanced by viscous dissipation, which is found by integrating the velocity of migration over the particle position for each particle trajectory.

In Figure 2.5 capillary energies extracted from these trajectories for isolated disks are plotted against $a\Delta c_0$. In this figure we report only regions of the trajectory far enough from the micropost to neglect hydrodynamic interactions [99]. The capillary energy plotted against $a\Delta c_0$ is linear; the root mean squared error of the linear fit is approximately $\sim 10^{-7}$ for each trajectory. This migration is in agreement with a simple functional form which we have derived previously for migration of cylindrical microparticles migrating in curvature fields [20]:

$$E = E_0 - \pi a^2 \gamma (\frac{h_p \Delta c_0}{2}) \tag{2.1}$$

where h_p is the amplitude of a quadrupolar distortion made by the particles. In our prior work on cylindrical microparticles, quadrupolar distortions were bounded by the equilibrium wetting configuration around the particles and thus could be associated with the particle shape. For the present case, we hypothesize that quadrupolar distortions are excited in the fluid interface owing to uncontrolled roughness of the particle, as suggested by Stamou et al. in their analysis of particles at planar interfaces [61]. The data in Figure 2.5 are consistent with particles with quadrupolar modes of $25 - 30$nm, a magnitude similar to the roughness of the particles, suggesting that particle roughness sets the scale for disturbances sourced by the particle into the interface. The curvature capillary energy associated with this weak distortion is appreciable; $\Delta E \sim 12,000 k_B T$, explaining the non-Brownian, deterministic paths observed for the disks.

In the experiments, the curvature of the host interface decreases monotonically with distance from the center of the micropost. For very small curvature, the capillary force driving upward migration is too small to overcome the downward pull of gravity, as reported by Blanc et al.; if a particle attaches to an interface far away from the micropost, the particle should not migrate [52]. We predict this threshold in our experiment by equating the gravitational force on the particle to the upward capillary force, $F_z = -\frac{\partial E}{\partial L}(\frac{dh_0}{dL})^{-1}$ and find that particles should fail to migrate for $L > 465\mu m$ and $h_p = 25$nm. This compares well to our experimental observation $L^{exp} \sim 308 - 449\mu m$.

Confronted by the observed linear dependence of the curvature capillary energy on $a\Delta c_0$, we derive the capillary energy in detail. Our work differs significantly from related work in the literature for spheres which reported quadratic dependence, i.e. proportional to $a^2 \Delta c_0{}^2$. Below, we show that, while, in principle, such a term might occur, its pre-factor is identically zero. To do so, we present a detailed discussion of capillary energy for weakly non-circular pinned contact lines on curved interfaces.

2.4. Theory

2.4.1. Disks with weakly roughened surfaces

We first consider the host interface without any particle. The free energy has two contributions,

$$E_1 = \gamma \oiint_D (1 + \frac{\nabla h_0 \cdot \nabla h_0}{2}) dA - \oiint_D \Delta p \ h_0 dA, \tag{2.2}$$

where h_0 is the height of the host interface prior to particle deposition, γ is the interfacial tension and D denotes the entire interfacial domain. In this expression, the first term is the energy due to the surface area assuming small slope $\epsilon = |\nabla h_0| \ll 1$ and the second term is the work done by the pressure jump across the interface Δp. When the particle is trapped at the interface, the free energy becomes

$$E_2 = \gamma_1 A_1 + \gamma_2 A_2 + \gamma \oiint_{D-P} (1 + \frac{\nabla h \cdot \nabla h}{2}) dA - \oiint_D \Delta p \ h dA, \tag{2.3}$$

where h is the height of interface after the particle is adsorbed, $\gamma_1 A_1$ and $\gamma_2 A_2$ are the product of the surface energies and wetted areas for the solid and the upper and lower fluids, respectively, P corresponds to the domain under the particle. The energy difference,

E between these two states is expressed

$$\begin{aligned} E =& \gamma_1 A_1 + \gamma_2 A_2 + \gamma[\oint_{\partial(D-P)} [\frac{1}{2}\eta\nabla\eta + \eta\nabla h_0]\cdot\mathbf{m}ds \\ & - \oiint_P (1+\frac{\nabla h_0 \cdot \nabla h_0}{2})dA + \oiint_P \frac{\Delta p}{\gamma}(h_0-\omega)dA] + O(\epsilon^4), \end{aligned} \tag{2.4}$$

where η is the disturbance field created by the particle, defined as $\eta = h - h_0$, ω is a shift of the particle center of mass perpendicular to the interface, $\partial(D-P)$ denotes the contours enclosing the domain D-P and $\mathbf{m}$ is the unit normal to these contours tangent to the interface pointing outward the domain. In Eq. 2.4, the first term is independent of particle position, the second term is the energy owing to the disturbance eta, the third term is the area of the hole in the interface created by particle adsorption and the final term is the pressure work (see Fig. 2.1 for detail).

The height of the host surface at any point satisfies the Young-Laplace equation,

$$2\gamma H = \Delta p, \tag{2.5}$$

where H is the mean curvature, $H = \frac{c_1+c_2}{2}$, and c_1 and c_2 are the principal curvatures. At any point on the interface, a polar coordinate (r,ϕ) can be defined tangent to the plane, where the origin for ϕ is along one of the principal axes. Adopting a Monge representation and utilizing Eq. 2.5, the interface height $h_0(r,\phi)$ for any surface can be expanded locally in this coordinate to be,

$$h_0(r,\phi) = \frac{r^2}{4}(2H_0 + \Delta c_0 \cos 2\phi), \tag{2.6}$$

where H_0 and $\Delta c_0 = c_1 - c_2$ are the mean and deviatoric curvatures of the host surface evaluated at particle center of mass. To solve for the disturbance field, Eq. 2.5 must be solved with respect to the boundary conditions at the three phase contact line Γ. The leading order mode of the contact line height is a quadrupolar undulation as the monopoly and dipolar terms are excluded by force and torque balances on the particle, respectively. This quadrupolar mode has an amplitude h_p (see Fig. 2.1(c), where we assume $h_p \ll a$. Higher order modes do not contribute to leading order and are not considered further.

In the most general case the disk cross section is non-circular; deviations in the contact line from a circular shape can be described as $\Gamma = a\left(1 + \sum_{n=1}^{\infty} \zeta_n \cos(n\phi - \alpha_n)\right)$, where α_n is a phase angle and $\zeta_n \ll 1$. Thus, the complete boundary condition is expressed,

$$h(r) = a\left(1 + \sum\nolimits_{n=1}^{\infty} \zeta_n \cos(n\phi - \alpha_n)\right) = h_p \frac{a^2}{r^2} \cos 2\phi. \tag{2.7}$$

We first derive an expression for trapping energy of a disk with a perfectly circular cross-section and weak roughness, and thereafter we extend the theory for weakly non-circular cases. Having defined the host interface as in Eq. 2.6, the area under the particle can be expressed as,

$$\oiint_P \left(1 + \frac{\nabla h_0 \cdot \nabla h_0}{2}\right) dA = \pi a^2 + \pi a^2 \left(\frac{1}{4} a^2 H_0^2 + \frac{1}{16} a^2 \Delta c_0^2\right) \tag{2.8}$$

where we linearized the surface metric. The determination of the remaining terms in Eq. 2.4 requires that we obtain the disturbance *eta* created by the particle by solving Eq. 2.5. For circular contact lines, the pinning boyndary condition can be expressed,

$$h(r = a) = \omega + h_p \cos 2\phi. \tag{2.9}$$

Far from the particle, the disturbance should decay to zero,

$$\lim_{r \to \infty}, h(r, \phi) \to h_0 = \frac{r^2}{4}(2H_0 + \Delta c_0 \cos 2\phi), \tag{2.10}$$

for which the general solution is

$$h(r, \phi) = \frac{r^2 H_0}{2} + \frac{\Delta c_0 \cos 2\phi}{4}\left(r^2 - \frac{a^4}{r^2}\right) + h_p \frac{a^2}{r^2} \cos 2\phi \tag{2.11}$$

where

$$\omega = \frac{a^2}{2} H_0. \tag{2.12}$$

To confirm these analytical expressions for h, we have preformed a numerical calculation based on a Green's function for the domain corresponding to the experimental setup, discussed in Ref. [100]; the numerically determined solution agrees excellently with the analysis. The disturbance due to the particle is

$$\eta = h_p \frac{a^2}{r^2} \cos 2\phi - \frac{\Delta c_0 \cos 2\phi}{4} \frac{a^4}{r^2}. \tag{2.13}$$

The derivatives of η and h_0 required to evaluate the remaining terms in the trapping energy are

$$\frac{\partial \eta}{\partial r} = -2h_p \frac{a^2}{r^3} \cos 2\phi + \frac{\Delta c_0 \cos 2\phi}{2} \frac{a^4}{r^3}, \tag{2.14}$$

$$\frac{\partial h_0}{\partial r} = \frac{r}{2}(2H_0 + \Delta c_0 \cos 2\phi), \tag{2.15}$$

The contour integral given in Eq. 2.4 can be evaluated as,

$$\begin{aligned} \oint_{\partial(D-P)} \frac{1}{2} \eta \nabla \eta \cdot \mathbf{m} ds &= \int_0^{2\pi} \frac{\eta r}{2} \frac{\partial \eta}{\partial r} \bigg|_{r\to\infty} d\phi - \int_0^{2\pi} \frac{\eta r}{2} \frac{\partial \eta}{\partial r} \bigg|_{r=a} d\phi \\ &= 0 + \pi(h_p^2 - \frac{h_p a^2 \Delta c_0}{2} + \frac{a^4 \Delta c_0^2}{16}), \end{aligned} \tag{2.16}$$

The first term inside the bracket is the self-energy of the quadrupolar roughness, a constant independent of curvature. The latter two terms depend on the curvature of the interface. To obtain a better insight into the effect of deviatoric curvature, we set $H_0 = 0$ and note that,

$$-\iint_P \left(\frac{\nabla h_0 \cdot \nabla h_0}{2}\right) dA = -\frac{1}{16}\pi a^4 \Delta c_0^2. \tag{2.17}$$

This is the excess area eliminated under the disk when it attaches to a saddle shaped interface and its magnitude is equal and opposite the quadratic term in Eq. 2.16. Hence, these terms cancel. We note that this is the case even for interfaces with non-zero mean curvature since in calculation of Eq. 2.17 terms include H_0 and Δc_0 never couple. The sole remaining contribution which could conceivably contribute a quadratic term in $a\Delta c_0$ is:

$$\oint_{\partial(D-P)} \eta \nabla h_0 \cdot \mathbf{m} ds = \int_0^{2\pi} \eta r \frac{\partial h_0}{\partial r}\bigg|_{r\to\infty} d\phi - \int_0^{2\pi} \eta r \frac{\partial h_0}{\partial r}\bigg|_{r=a} d\phi = 0 \tag{2.18}$$

To evaluate this expression, particular care must be taken to evaluate this expression at all contours enclosing the area. The integrand, a product of decaying and growing modes of the same power, is independent of radial position. Therefore, the evaluation of the integral at the inner and outer contours yields a value of zero, and there are no quadratic contributions to the free energy.

It remains to evaluate the pressure work contribution which can be written,

$$\begin{aligned}\iint_P \frac{\Delta p}{\gamma}(h_0 - \omega) dA &= 2H_0 \int_0^a r' dr' \int_0^{2\pi} (h_0 - \omega) d\phi \\ &= \frac{\pi a^4 H_0^2}{2} - \pi a^4 H_0^2 = -\frac{\pi a^4 H_0^2}{2},\end{aligned} \tag{2.19}$$

by substituting Eqs. 2.16, 2.18 and 2.19 in Eq. 2.4, the capillary energy of a particle with pinned circular contact line can be written as,

$$E = E_0 - \pi a^2 \gamma (\frac{3a^2 H_0^2}{4} + \frac{h_p \Delta c_0}{2}) \tag{2.20}$$

where $E_0 = \gamma_1 A_1 + \gamma_2 A_2 - \gamma \pi a^2 (1 - \frac{h_0^2}{a^2})$, is independent of curvature. The deviation of

Eq. 2.20, and its favorable comparison to experiment, is the main point of this paper. On interfaces with constant mean curvature, Eq. 2.20 reduces to Eq. 2.1, which is compared to experiment in Figure 2.5. Disks with pinned contact lines migrate solely because of roughness, with driving capillary energies proportional to the amplitude of the quadrupolar mode of the distortion that they excite in the interface.

Recall that the disks are not only rough but also have weakly noncircular edges. To ascertain the importance of this non-circularity, we modified the above calculation to discuss for slightly deformed disks. My collaborator, Dr. Sharifi-Mood, performed domain perturbation analysis and showed that the correction is on the order of 4-5 k_BT, i.e. $\sim 10^4$ times smaller than the observed curvature capillary energies. Numerical solution for the disturbance created by the particle in the interface agrees with the analytical solution, to with 2%. This confirms the analytical form for the disturbance created by the particle used to calculate the curvature capillary energy. For further details, please refer to Ref. [100].

2.5. Conclusions

We have performed experiments using disks with pinned contact lines on an interface with strong deviatoric curvature gradients. The particles migrated up to sites of high curvature with capillary energies that are linear in the deviatoric curvature Δc_0. This experimental finding is in contrast to prior work on spheres with equilibrium contact lines in the interface. To place this result in context, we derived an analytical expression for the curvature capillary migration energy, and show that it is indeed linear in the product $h_p \Delta c_0$, where h_p is the amplitude of the quadrupolar mode of the particle sourced disturbance. The values for h_p inferred from the energy data correspond to the scale of the particle roughness as determined by AFM. Our analysis shows definitively that no quadratic term in deviatoric curvature is present in the migration energy, a marked difference from prior work in the literature. This analysis can be extended to pair interactions of particles on curved interfaces. Qualitatively, the formation of chains along the curvature gradient direction evident in Figure 2.4 can be readily be explained. The quadrupole owing to roughness aligns along the principal axes of the interface, so interacting particles chain along the radial direction. Finally, these results for disks have important implications for spheres with pinned contact lines; we address this issue in the next chapter.

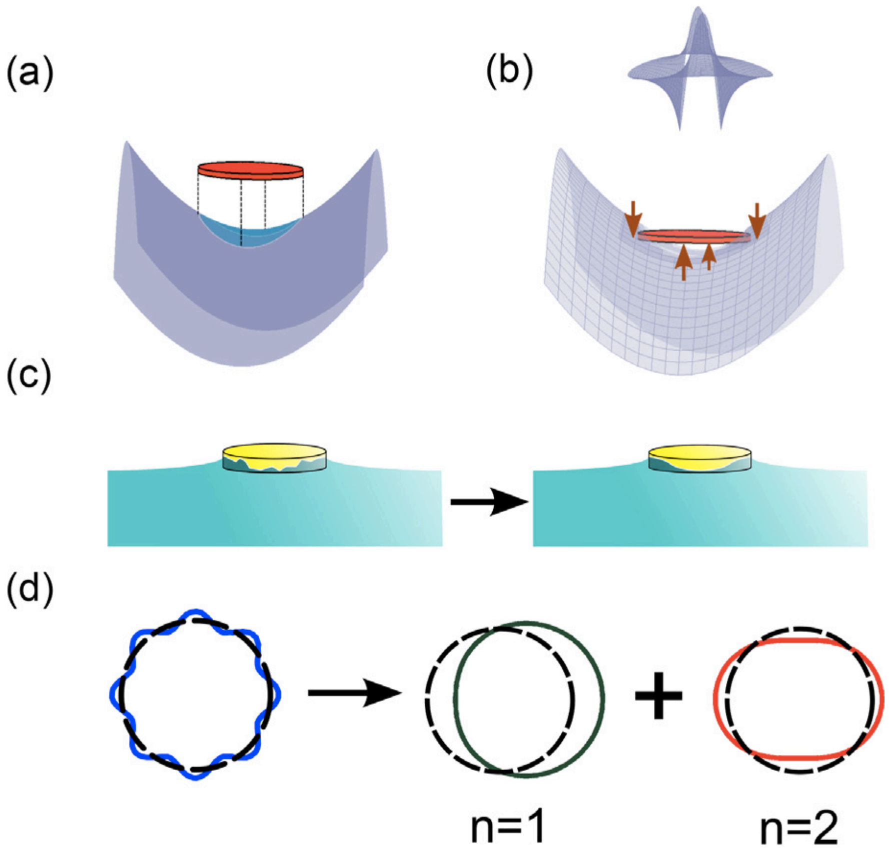

Figure 2.1: Schematic representations of (a) area of the hole under the host surface, (b) curvature induced distortion of the pinned contact line, (c) height undulations of contact line e.g. due to particle roughness and (d) non-circular contact line (top view) shape decomposition into dipolar ($n = 1$, $\Gamma_1 = a(1 + \xi_1 \cos\phi)$), and quadrupolar ($n = 2$, $\Gamma_2 = a(1 + \xi_2 \cos 2\phi)$) modes.

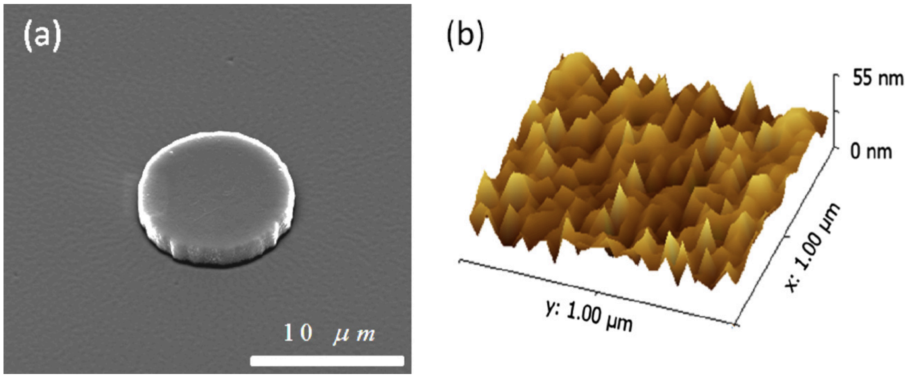

Figure 2.2: (a) SEM image of a microdisk and PDMS negative of the air-water interface showing contact line pinning. (b) AFM reveals nanoscopic roughness of the disk surfaces of with RMS values ranging of 18-32 nm.

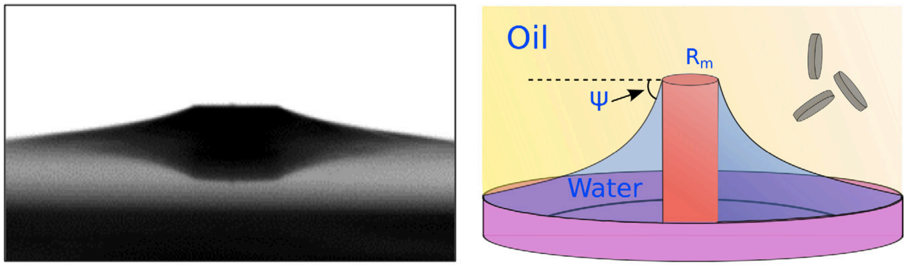

(a) (b)

Figure 2.3: The curved interface (a) side view of the curved interface. (b) Schematic of the curved interface molded around a micropost. The principal curvatures are greatest in magnitude close to the post, and decrease monotonically with distance from the post.

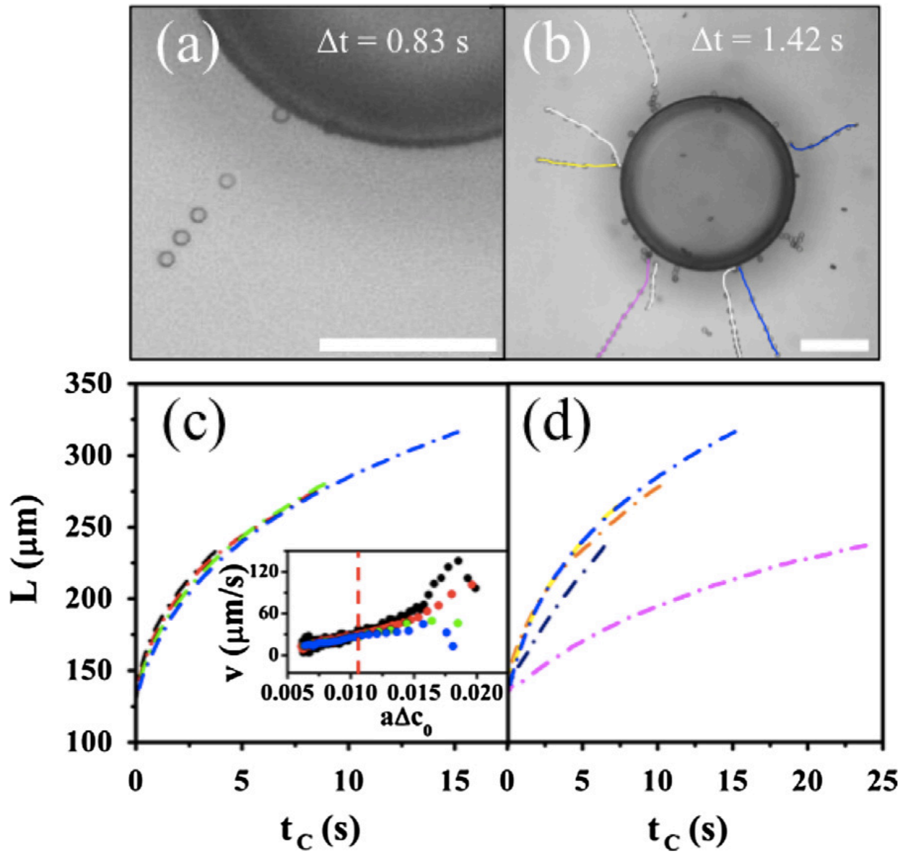

Figure 2.4: Time stamped images (a) of a microdisk trajectory, and (b) of multiple trajectories around a crowded micropost. Particles chain at micropost along the radial direction. (c) Trajectories of isolated disk migrating in the curvature field. (d) Trajectories for disks migrating on a crowded interface. Colors for trajectories in (c) and (d) correspond to trajectories of similar colors in (b). (scale bar= 100 μm).

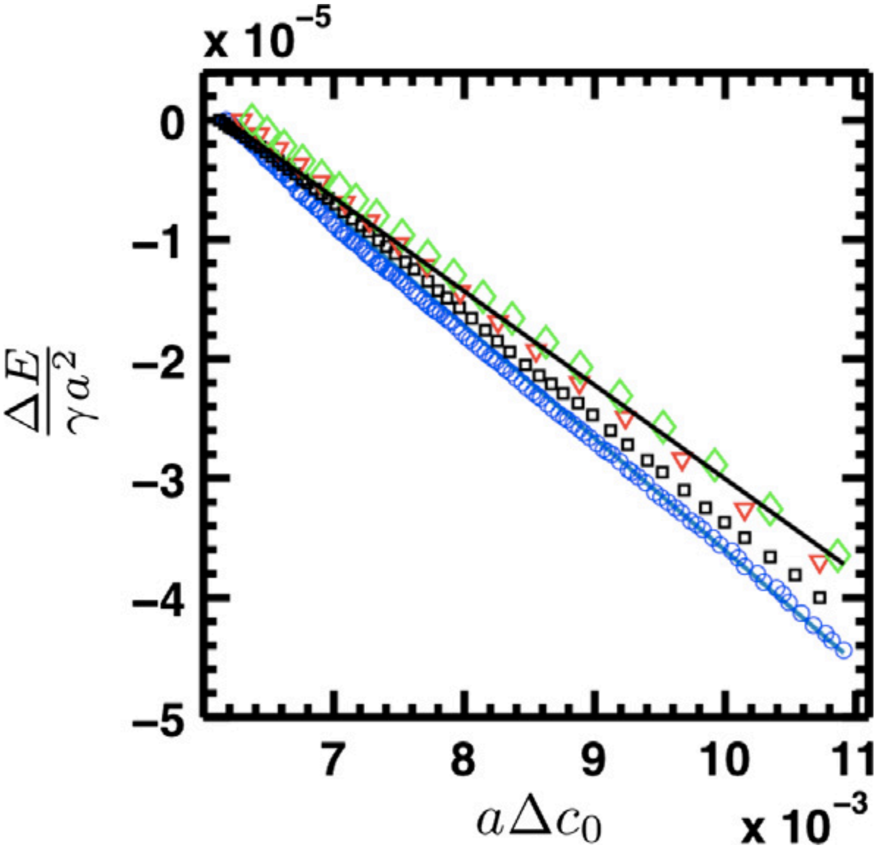

Figure 2.5: Comparison of predicted energy (solid lines) against those extracted from experiment for trajectories in Fig. 2.4(c) for isolated particles (symbols). (The colors correspond to the trajectories in Fig. 2.4(b). The solid black line corresponds to $h_p = 25$ nm, the solid blue line corresponds to $h_p = 30$ nm.

CHAPTER 3 : Curvature capillary attraction: Microspheres at curved interfaces

3.1. Introduction

Capillary interactions are ubiquitous between particles on fluid interfaces. They trap particles at the interface [30] and determine their ensuing organization [20, 39, 64], allowing particles to be widely exploited in technological applications such as stabilization of foams and emulsions [84], and in settings as diverse as the food [101], pharmaceutical [102], mineral recovery [103], and petroleum industries [104]. For microparticles of radius a at planar interfaces of tension γ, gravity is irrelevant, as the Bond number $Bo = \frac{\Delta\rho g a^2}{\gamma} \ll 1$, where g is the gravitational acceleration constant, and $\Delta\rho$ is the density difference between the two fluids on either side of the interface. In this limit, particles with undulated contact lines distort the interface around them, with an associated excess interfacial area. The deformation fields and interfacial area depend on the relative position of the particles, yielding decreasing capillary energy as particles approach [61].

In this research we are interested in the behavior of isolated microparticles trapped on curved interfaces. In experiment, microparticles migrate along curvature gradients to sites of high curvature, as has now been observed for microcylinders [20], microspheres [52], and microdisks [100]. Theoretically, the curvature capillary energy driving this migration is simply the sum of the surface energies and pressure work for particles at the interface. When particles attach to their host interfaces, they change the interface shape owing to the boundary condition at the contact line where the interface meets the particle. There are two limits for this boundary condition. The interface can intersect the particle with an equilibrium contact angle θ_0, determined by the balance of surface energies according to Young's equation [105]. Alternatively, the contact line can be pinned by kinetic trapping at heterogeneities, roughness or other pinning sites on the particle surface [53, 57, 61, 95, 96, 97]. Curvature capillary migration depends on the coupling of the particle-sourced distortion with the host interface shape. For a particle which is much smaller than the capillary length, far from pinning boundaries, and therefore small compared to the prevailing curvature fields, particle-sourced distortions decay over distances comparable to the particle radius. This scenario lends itself to analysis by a singular perturbation method [106, 107]. In a particle-fixed reference frame defined in the plane tangent to the interface, the host interface shape around the particle can be locally decomposed into terms proportional to the host interface mean curvature and deviatoric curvature. By rescaling the governing equations with respect to the particle radius, the shape of the interface around the particle can be found over length scales comparable to this radius. This approach allows clear treatment of limiting boundary conditions on particle sourced distortions and the ranges of validity of local expansions of the host interfaces. It also clarifies the appropriate outer limits on (area or contour) integrals used to evaluate the excess area of the interface created by the particle. Using this method, we have previously solved the curvature capillary energy for disks with pinned contact lines, which applies equally to spheres with pinned contact lines in the limit of weak undulations [100]. We apply the approach to derive the curvature capillary energy for spheres with equilibrium contact angles. While the curvature capillary energies for this scenario have been derived previously and reported to be quadratic in the deviatoric curvature of the interface [52, 92, 93, 94], we find that this term has prefactor zero. We identify the source of the discrepancy between our result and that published previously. We predict that spheres migrate by capillarity on constant mean curvature interfaces only if their contact lines are pinned, and that spheres with equilibrium contact lines would have energies several orders of magnitude weaker than is observed in experiment.

We perform experiments in which we record the trajectories of polystyrene microspheres at hexadecane-water interfaces with well defined curvature fields. We compare the energy dissipated by particle migration to the curvature capillary energy expressions, and find that the spheres migrate in agreement with the expression for pinned contact lines.

This work was performed in collaboration with Dr. Sharifi-Mood. It has been published in Soft Matter as a paper entitled ”Curvature capillary migration of microspheres”, Ref [108]-

Reproduced by permission of The Royal Society of Chemistry. In this work, I designed and performed the experiments, and tracked particle trajectories. My collaborator, Dr. Sharifi-Mood, derived the theory for particle curvature interaction and performed the numerical analysis.

3.2. Theory

Here we give a concise derivation of the capillary energy of a sphere trapped on a curved fluid interface. Without loss of generality, we focus on interfaces with zero mean curvature as the role of finite mean curvature gradient has been addressed in the literature [93, 100]. We first consider the free energy of a system including a free interface with a spherical colloidal particle submerged in subphase fluid 1. In this case, the free energy can be written as,

$$E_1 = \gamma \oiint_{D} (1 + \frac{\nabla h_0 \cdot \nabla h_0}{2}) dA + \gamma_1 A_s, \tag{3.1}$$

where h_0 is the Monge representation of the host interface height prior to particle attachment, D denotes the entire interfacial domain, $dA = dxdy$, γ_1 is the surface energy of the colloid with fluid 1, and $A_s = 4\pi a^2$ accounts for the total area of the colloid. In writing the above expression we have assumed small slopes, i.e. $|\nabla h_0| \ll 1$. Upon attaching to the host interface, the particle creates a disturbance to satisfy its boundary condition on the three phase contact line. The free energy of the system in this case is,

$$E_2 = \gamma_1 A_1 + \gamma_2 A_2 + \gamma \oiint_{D-P} (1 + \frac{\nabla h \cdot \nabla h}{2}) dA, \tag{3.2}$$

where h is the interface height after the particle is adsorbed, $\gamma_1 A_1$ and $\gamma_2 A_2$ are the product of the surface energies and wetted areas for the solid in contact with the upper and lower fluids, respectively, and P denotes the domain under the particle. The capillary energy associated with adsorption of a particle to an interface can be found simply via subtraction of the two energies,

$$\begin{aligned}E = E_2 - E_1 = &\gamma_1 A_1 + \gamma_2 A_2 - \gamma_1 A_s + \\ &\gamma[\oiint\limits_{D-P} (\frac{\nabla\eta \cdot \nabla\eta}{2} + \nabla\eta \cdot \nabla h_0) dA - \oiint\limits_{P} (1 + \frac{\nabla h_0 \cdot \nabla h_0}{2}) dA],\end{aligned} \tag{3.3}$$

where η is the disturbance field defined as $\eta = h - h_0$. In the above expression, the first integral is due to the disturbance created by the particle and the second integral is the area of the hole in the host interface under the particle. We integrate the first integral by parts and then apply the divergence theorem to have,

$$\oiint\limits_{D-P} [\frac{\nabla\eta \cdot \nabla\eta}{2} + \nabla\eta \cdot \nabla h_0] dA = \oint\limits_{\partial(D-P)} [\frac{1}{2}\eta\nabla\eta + \eta\nabla h_0] \cdot \mathbf{m} ds, \tag{3.4}$$

where $\partial(D-P)$ denotes the contours enclosing the domain $D - P$ (See Fig. 3.1). There are two contours enclosing this domain: one, not shown, infinitely far from the particle, with outward pointing vector in the radial direction, and the other enclosing the region P with outward-pointing unit normal vector $\mathbf{m}$. Consequently the curvature capillary energy of the system can be expressed as,

$$\begin{aligned}E = E_2 - E_1 = &\gamma_1 A_1 + \gamma_2 A_2 - \gamma_1 A_s + \\ &\gamma[\oint\limits_{\partial(D-P)} [\frac{1}{2}\eta\nabla\eta + \eta\nabla h_0] \cdot \mathbf{m} ds - \oiint\limits_{P} (1 + \frac{\nabla h_0 \cdot \nabla h_0}{2}) dA].\end{aligned} \tag{3.5}$$

We expand the interface locally around an arbitrary point to obtain a saddle shape,

$$h_0(x, y) = \frac{\Delta c_0}{4}(x^2 - y^2), \tag{3.6}$$

where (x, y) coordinate is tangent to the host interface, oriented along the principle curvatures c_1 and c_2, and Δc_0 is the deviatoric curvature of the host interface defined as,

$$\Delta c_0 = c_1 - c_2, \tag{3.7}$$

where we adopt a convention such that c_1 is always positive. We discuss the range of validity of Eq. 3.6 in terms of an asymptotic treatment in Ref. [108], and in terms of a comparison of host interface shape used in our experiments. To evaluate the integrals in Eq. 3.5, we must define the boundary condition at the three phase contact line, and determine the associated disturbance field η. We discuss two distinct scenarios for this energy (see Fig. 3.2).

3.2.1. Pinned contact line

The curvature capillary energy E, for a particle with nearly circular cross section and a pinned contact line trapped on a host interface with arbitrary mean curvature H_0 and deviatoric curvature Δc_0 was derived previously [100]. The height of the pinned contact line contour can be decomposed into a multipole expansion with quadrupolar mode of amplitude h_p. The associated curvature capillary energy is,

$$E = E_0 - \gamma \pi a^2 (\frac{h_p \Delta c_0}{2} + \frac{3a^2 H_0^2}{4}). \tag{3.8}$$

In this expression, the first term E_0 is independent of the local curvature. The second term predicts that a particle will move to sites of high deviatoric curvature, while the third predicts particle migration along gradients of mean curvature. To understand the relevant importance of these terms, we consider $\frac{a^2 H_0^2}{h_p \Delta c_0} \sim \frac{a}{h_p} \frac{a \Delta p}{\gamma}$ where Δp is the pressure jump across the interface. This ratio suggests that, for sufficiently small pressure jump across the interface, the effect of mean curvature can be neglected. In section 3, we explore this regime in experiment.

3.2.2. Equilibrium wetting

We use a formal matched asymptotic expansion [106, 107] to evaluate the curvature capillary energy in terms of the small parameter $\lambda = r_0 \Delta c_0$, where $r_0 = a\ \sin\theta_0$ is the radius of the hole made a sphere is a planar interface. Here, we give the main features of this derivation in dimensional form, and note the bounds on the solutions and ranges of validity implied by the asymptotics.

For a spherical particle in a curved interface with an equilibrium wetting condition, the fluid interface deforms until it satisfies the equilibrium contact angle at every point on the contact line. The contact line shape is not known *a priori* and must be determined as a part of analysis, as was originally done by Würger [92]. The shape of contact line can be deduced from geometrical relationships (see Fig. 3.3) to be,

$$\cos\theta = \cos\theta_0 + \frac{h(\mathbf{r} \in \rho)}{a}, \tag{3.9}$$

$$\sin\theta = \frac{\rho}{a}, \tag{3.10}$$

where θ is a polar angle which located the contact line in a spherical coordinate system with respect to the particle center, $\cos\theta_0 = \frac{d}{a}$, and $\rho(\phi)$ is the contour of the contact line projected into a plane, which obeys,

$$\rho = a\sqrt{1 - \cos^2\theta}. \tag{3.11}$$

By substituting Eq. 3.9 and 3.10 in this expression and assuming $\frac{h(\mathbf{r}\in\rho)}{a} \sim O(\lambda) \ll 1$, the radial location of contact line projected into the $x - y$ plane is,

$$\rho = r_0 - h(\mathbf{r})\cot\theta_0 - \frac{1}{2}\frac{h^2(\mathbf{r})}{r_0}(\cot^2\theta_0 + 1) + ...|_{\mathbf{r}\in\rho}, \tag{3.12}$$

The corresponding unit vector $\mathbf{m}$ and the arc length element ds up to the first correction in λ are,

$$\mathbf{m} = -[\mathbf{e}_r + \frac{\cot\theta_0}{r_0}\frac{\partial h(\mathbf{r})}{\partial\phi}\mathbf{e}_\phi]\,|_{\mathbf{r}\in\rho}, \tag{3.13}$$

$$ds = r_0[1 - \cot\theta_0\frac{h(\mathbf{r})}{r_0}]d\phi\,|_{\mathbf{r}\in\rho}. \tag{3.14}$$

Young's equation requires,

$$\mathbf{n}_P \cdot \mathbf{n}_I = \cos\theta_0|_{\mathbf{r}\in\rho}, \tag{3.15}$$

where $\mathbf{n}_P$ is the unit normal to the particle and $\mathbf{n}_I$ is the unit normal to the interface evaluated at the contact line. By applying this expression, the boundary condition for the interface shape at the three phase contact line to the leading order is,

$$\frac{h}{r_0} = \frac{\partial h}{\partial r}\,|_{r=r_0}. \tag{3.16}$$

The height of interface satisfies the Young-Laplace equation, which, assuming small slopes, reduces to the Laplacian:

$$\nabla^2 h = 0. \tag{3.17}$$

The boundary condition for the particle-sourced distortion in the far field can be derived using a Van Dyke matching scheme [106, 107] to match the interface shape far from the particle to the host interface shape. The resulting boundary condition far from the particle is,

$$\lim_{r\to\infty} h(r,\phi) = h_0 = \frac{\Delta c_0}{4}\; r^2\cos 2\phi, \tag{3.18}$$

where the limit $r \to \infty$ implies exploring regions around the particle large compared to the particle radius. Using Eq. 3.16 and Eq. 3.18 the leading order interface shape is,

$$h(r,\phi) = \frac{\Delta c_0 \cos 2\phi}{4}(r^2 + \frac{r_0^4}{3r^2}), \tag{3.19}$$

The corresponding disturbance to the interface is,

$$\eta = h - h_0 = \frac{\Delta c_0 \cos 2\phi}{12} \frac{r_0^4}{r^2}. \tag{3.20}$$

Asymptotic analysis for the curved interface around the circular microcylinder show that Eq. 3.18 remains valid everywhere the disturbance (Eq. 3.20) is finite. With this information, we determine the curvature capillary energy Eq. 3.5. In so doing, we can straight-forwardly apply the limits at the contact line and $r \to \infty$, knowing that these functions remain valid within this domain. This is indeed consistent with experiment. We mold the fluid interface by pinning it to a micropost. The interface forms a shape with a well defined curvature field. For micro-particles on interfaces with deviatoric curvatures like those in our experiments $\Delta c_0 \sim 400 - 3000\ m^{-1}$, the distortions will be $\ll 10^{-10} m$ within $5-6$ radii, a, from the the center of particle. Over such ranges, the shape of the fluid interface Eq. 3.18 agrees well with the full function describing the interface shape $h^{\text{micropost}}$; the quadrupolar mode of $h^{\text{micropost}}$ agrees with Eq. 3.18 to better than 2% error. This is the sole mode that can couple to the quadrupolar undulation of the particle. While we perform this matching in detail only for the host interface used in our experiments, the asymptotic analysis can be applied similarly to any fluid interface provided $\frac{a}{R_c} \ll 1$, R_c is the characteristic length of the host interface. The deviatoric curvature part of far field boundary condition is given by Eq. 3.18, with the details for the curvature source (e.g. the micropost in our example) emerging in the expression for Δc_0. In the event that the interface has finite mean curvature, an additional term emerges with the local mean curvature of the interface.

We evaluate

(i) the self-energy of the disturbance created in the host interface, the sum of the following two contour integrals:

$$\oint\limits_{\rho} \frac{\eta}{2}\nabla\eta \cdot \mathbf{m}ds = r_0^4 \int_0^{2\pi} \frac{\Delta c_0^2 \cos^2 2\phi}{144} d\phi = \frac{\pi \Delta c_0^2 r_0^4}{144} \tag{3.21}$$

$$\oint\limits_{r\to\infty} \frac{\eta}{2}\nabla\eta \cdot \mathbf{m}ds = 0 \tag{3.22}$$

This term captures the increase in interfacial area owing to the particle sourced distortion. (ii) the interaction of the disturbance and the host interface, given by the sum of the following two contour integrals:

$$\oint\limits_{\rho} \eta\nabla h_0 \cdot \mathbf{m}ds = -r_0^4 \int_0^{2\pi} \frac{\Delta c_0^2 \cos^2 2\phi}{24} d\phi = -\frac{\pi \Delta c_0^2 r_0^4}{24} \tag{3.23}$$

$$\oint\limits_{r\to\infty} \eta\nabla h_0 \cdot \mathbf{m}ds = r_0^4 \int_0^{2\pi} \frac{\Delta c_0^2 \cos^2 2\phi}{24} d\phi = +\frac{\pi \Delta c_0^2 r_0^4}{24}. \tag{3.24}$$

These terms are equal and opposite, and hence sum to zero. Thus, the net contribution of the particle induced disturbance, the sum of (i) and (ii), is

$$\oint\limits_{\partial(D-P)} [\frac{1}{2}\eta\nabla\eta + \eta\nabla h_0] \cdot \mathbf{m}ds = \frac{\pi \Delta c_0^2 r_0^4}{144}. \tag{3.25}$$

(iii) We calculate the energy decrease owing to the area of the hole under the particle as,

$$-\oiint\limits_{P} (1 + \frac{\nabla h_0 \cdot \nabla h_0}{2}) dS = -\pi r_0^2 - \frac{\pi \Delta c_0^2 r_0^4}{144}. \tag{3.26}$$

The second term in the above expression is equal and opposite to the term in Eq. 3.25. Summing the curvature dependent terms in (i),(ii) and (iii), the energy costs of increased area by the deformation field is shown to be offset by the energy decrease owing to the area eliminated under the particle. This exact canceling of two effects occurs both for the pinned and equilibrium contact lines.

To complete this derivation, the contribution of the (curvature independent) wetting energies can be simplified by noting,

$$\gamma_1 A_1 = \gamma_1 2\pi a^2(1+\cos\theta_0), \tag{3.27}$$

$$\gamma_2 A_2 = \gamma_2 2\pi a^2(1-\cos\theta_0), \tag{3.28}$$

$$\gamma_1 A_s = \gamma_1 4\pi a^2, \tag{3.29}$$

and

$$\cos\theta_0 = \frac{\gamma_2-\gamma_1}{\gamma}, \tag{3.30}$$

summing these contributions, the net curvature capillary energy to order λ^2 is identically zero, i.e.,

$$\frac{E}{\gamma\pi r_0^2} = E_p + O(\lambda^4), \tag{3.31}$$

where the first term in this expression is Pieranski's trapping energy [30] for a sphere obeying an equilibrium contact angle in a planar interface $E_p = -\sin^{-2}\theta_0(1-\cos\theta_0)^2$. The above expression is exact up to the λ^4 term.

Eq. 3.31 shows that there is no quadratic term in Δc_0 for spheres with equilibrium contact lines, and that the curvature capillary energies for these particles are extremely weak. A similar conclusion has been found for perfect disks with circular pinned contact lines [100]. These results differ significantly from prior theory in the literature for this problem. The origin of the discrepancy is an inappropriate treatment of the contour integral given in Eq. 3.24, which was assumed to be zero in prior work.

3.3. Experiments

We study migrations of polystyrene colloidal spheres (Polyscicences, Inc.) with mean diameter of $2a = 10\ \mu m$. Fig. 3.4.(b) illustrates an SEM image of a microsphere revealing qualitatively the surface roughness of the particle. AFM measurement (Bruker Icon) indicates that the root mean squared roughness of the particles is $\sim 15-21\ nm$ (see Fig. 3.4.(c)).

We impose a curvature field to the host interface using a technique reported previously [20] which we recapitulate briefly. A curved oil-water interface is formed around a micropost which is either circular or square in cross section (see the schematic in Fig. 3.4(a)). The interface pins to the edge of the post, and has a height H_m at the post's edge. The post is centered within a confining ring located several capillary lengths away $\frac{r_{ring}}{\sqrt{\frac{\gamma}{\Delta\rho g}}} = 5.5$, where r_{ring} is the radius of the outer ring. By adjusting the volume of water, the slope of the interface at the post's edge is adjusted to be $\psi \sim 15 - 18°$. This system is gently covered in hexadecane in order to prevent evaporation and to protect the interface from stray convection. The interface height in a region sufficiently close to the circular post is well approximated by:

$$h^{\text{micropost}} = H_m - R_m \tan\psi \ln(\frac{L}{R_m}), \tag{3.32}$$

where L is the distance to the center of the post. This interface has zero mean curvature $H_0 = (c_1 + c_2)/2 = 0$, and finite deviatoric curvature $\Delta c_0 = c_1 - c_2$ varying with the radial position. Owing to the finite volume of fluid, there is a weak but negligible pressure drop across the interface.

A dilute suspension of microspheres in hexadecane is prepared. A drop of this suspension is carefully dropped on top of the oil phase. The particles then gently sediment under gravity. Once attached to the interface, they migrate uphill in a deterministic path along deviatoric curvature gradients. We only focus on isolated particles far from neighbors (distances greater than 10-15 radii) and the micropost ($L > R_m + 10a$) to rule out the pair capillary and hydrodynamic interactions [109]. The capillary energy was estimated by evaluating the total dissipation according to the appropriate drag formula (Stokes' law) along particle trajectories.

In Fig. 3.5(a), we illustrate the time stamped images of trajectories for migrating spheres for constant time increment ($\Delta t = 1\ s$). These images reveal that the spheres are propelled faster in the region closer to the post where the magnitude of deviatoric curvature is greater. Note that the size of the spheres are so small that the inertial effects can be neglected ($Re \sim 10^{-3}$) within the entire trajectory. These trajectories are nearly radial, as the corresponding curvature field around the cylindrical post has no dependency on the azimuthal angle ϕ. Fig. 3.5(b) shows the radial distance of the migrating microspheres from the center of the post, L, as a function of time remaining until contact, $t - t_c$, where t_c is the time in which the sphere reached the edge of the post. Qualitatively, these trajectories are similar to those reported previously for microdisks with pinned contact lines migrating in curvature fields. To investigate this quantitatively, we compare energy dissipated along the particle trajectory to theory.

To do so, we note that, in the limit of zero inertia, and neglecting potential energy differences, the curvature capillary energy expended to drive the particles is balanced by viscous dissipation. The total energy dissipated along the trajectories can be extracted from the trajectories according to $\Delta E = \int_{L_0}^{L} F_{drag} dL'$ where L_0 is the reference point and L is an arbitrary point along the trajectory. We used the Stokes' drag formula for a sphere equally immersed in the subphase fluids, $F_{drag} = 6\pi\mu U a$, where μ is the average viscosity of oil and water evaluated at the temperature of the environment. The curvature capillary energy found over the trajectories beginning at $a\Delta c_0 = 6 \times 10^{-3}$ and ending ten particle radii from the micropost was plotted against $a\Delta c_0$ as open symbols in Fig. 3.6; this range of $a\Delta c_0$ was selected because all trajectories captured in experiment spanned this region. The relationship is linear and the total energy difference along a typical trajectory is thousands of times greater than thermal unit energy $k_B T$. The curvature capillary energy is presented normalized by $\gamma\pi a^2 = 8.8 \times 10^8\ k_B T$; the energy for the segment of the particle paths shown in Fig. 3.6 is in the range of $6,000 - 50,000\ k_B T$. This magnitude indicates that the equilibrium wetting boundary condition cannot be responsible for the migration of the spheres in our experiment, as according to Eq. 3.31 for a typical microsphere $a = 5\mu m$ with equilibrium contact angle of $\theta = 90°$, the curvature capillary energy is of magnitude $\Delta E \sim \gamma\pi a^2 \sin^2\theta_0 \lambda^4 \sim 10k_BT$. Moreover the relationship between ΔE and $r_0\Delta c_0$ would be highly nonlinear. Hence, we conclude that the equilibrium contact angle boundary condition does not apply to our microspheres. Rather, the microspheres migrate with pinned contact lines.

We propose that this curvature migration is an assay for nanometric corrugations of the contact line in a trapped state. The magnitude of the quadrupolar mode h_p for the contact line undulations can be inferred from the trajectories in Fig. 3.5. While 7 of 10 of the reported trajectories have h_p similar in scale to the particle roughness (between $20 - 40$ nm), magnitudes for the remaining trajectories were larger, with h_p as high as 130 nm for one trajectory. These results indicate that similar particles have differing pinning states at the interface, with significant consequences for their ensuing dynamics. The role of gravity for particles on curved interfaces has been addressed previously [52, 100]. Because the Bond number is negligible, particle weight plays no role in the deformation of the interface, and the analyses above are valid. For weak enough curvature gradients, however, particles cannot overcome potential energy barriers and thus can attain an equilibrium height.

This form for the curvature capillary energy has been invoked previously to study curvature capillary migration of cylindrical microparticles which followed complex trajectories on interfaces around square microposts with associated complex curvature fields [20]. If the spheres indeed have identical physics, they, too, should migrate along complex contours in such a curvature field. We have studied trajectories of spheres in this setting (see Fig. 3.7(a), in which isolated particles migrate to corners, as does a pair of dimerized particles at the lower right hand corner). To compare particle trajectories to local curvatures, the curvature field around the square micropost was determined using a Galerkin finite element method (Simulation ran by Dr. Sharifi-Mood). Vectors indicating the magnitude and direction of gradients in deviatoric curvature are indicated in Figures 3.7(b) and (c). The spheres migrate from their initial point of attachment along paths defined indeed by these vectors. The ability of the sphere to trace this complex trajectory confirms the underlying physics of microparticles with pinned contact lines is similar regardless of details of the particle shape, and is consistent with the concept that the particle quadrupolar mode couples to the underlying saddle shaped surface.

3.5. Conclusions

We study micropshere migration owing to curvature capillary energy in theory and experiment. We show that for equilibrium contact angles, the curvature capillary energy is very weak, with leading order contributions of fourth order in deviatoric curvature or higher, in contradiction to the accepted form in the literature. This leading order contribution would amount to roughly 10 k_BT in our experiments, several orders of magnitude lower that we measure in experiment. In experiment, microspheres migrate along deterministic trajectories defined by curvature gradients. We find that the corresponding capillary curvature energy propelling the particles ranges from $6,000 - 50,000$ k_BT. We compare these observations to arguments derived previously for particles with pinned contact lines, in which the quadrupolar mode of the particle contact line undulation couples with the curvature field to yield an energy linear in the deviatoric curvature. The data indeed obey this form, allowing the magnitude of the particle induced quadrupole to be inferred. In many cases, it is comparable to particle roughness as determined by AFM. However, significantly larger magnitudes are also found, suggesting that similar particles can have different pinned states at the interface. These results imply that contact line pinning occurs for microparticles at these curved fluid interfaces with dramatic implications in their dynamics at interfaces.

3.6. Summary of capillary attraction

3.6.1. Curvature capillary energy

When a particle with a pinned, undulated contact line attaches to a curved fluid interface, the interface curvature alters the trapping energy. In the limit of small slopes, for particles small compared to the principal radii R_1, R_2, the host interface near the particle center can be expanded in terms of the mean curvature $H_0 = \frac{1}{2}(c_1 + c_2) = \frac{1}{2}(\frac{1}{R_1} + \frac{1}{R_2})$ and the deviatoric curvature $\Delta c_0 = c_1 - c_2 = \frac{1}{R_1} - \frac{1}{R_2}$, where c_1 and c_2 are the principal curvatures evaluated at the particle center of mass. In the absence of the particle, the interface shape is

$$h_0 = \frac{r^2 H_0}{2} + \frac{\Delta c_0}{4} r^2 \cos 2\phi. \tag{3.33}$$

When a particle attaches to the curved interface, the trapping energy is:

$$\Delta E = (\gamma_{SL} - \gamma_{SV})\Delta A_{SL} + \gamma \Delta A_{LV} + \gamma \delta A + \text{ PV work}. \tag{3.34}$$

We consider the right-hand side of this expression term by term. The wetting energies are unchanged from the planar case given the symmetries of the Fourier modes that describe the contact line. The hole made by the particle in the interface and the area in the distortion field both depend on the curvature field, and must be computed. Finally, changes in height owing to the particle require PV work against the pressure jump at the interface. To evaluate these terms, we find the disturbance made to the interface shape by the particle

$\eta = h - h_0$, which requires solution of a simple boundary value problem:

$$\nabla^2 h = 0, \tag{3.35}$$

$$h(r = a) = h_{qp} \cos 2\phi, \tag{3.36}$$

$$h(r \to \infty) = h_0, \tag{3.37}$$

$$\begin{aligned} h &= h_0 + \eta_{qp} + \eta_{in} \\ &= h_0 + h_{qp}\frac{a^2}{r^2}\cos 2\phi - \frac{a^2 \Delta c_0}{4}\frac{a^2}{r^2}\cos 2\phi + \omega_0. \end{aligned} \tag{3.38}$$

The disturbance η has two parts: the particle imposed distortion η_{qp} and the induced disturbance or reflected mode η_{in} (Fig. 1.4). Additionally, the particle shifts vertically to situate itself in the interface with finite mean curvature $\omega_0 = \frac{a^2 H_0}{2}$; this requires PV work:

$$\Delta P \iint\limits_P (h_0 - \frac{H_0 a^2}{2}) r dr d\phi = -\gamma \pi a^2 \frac{H_0^2 a^2}{2}. \tag{3.39}$$

The area of the interface is given by the sum $\Delta A_{LV} + \delta A$. By attaching to the interface, the particle forms a circular hole with area πa^2, with a correction owing to curvature:

$$\Delta A_{LV} = -\iint\limits_P (\frac{\nabla h_0 \cdot \nabla h_0}{2}) r dr d\phi = -\pi a^2 (1 + \frac{a^2 H_0^2}{4} + \frac{a^2 \Delta c_0^2}{16}). \tag{3.40}$$

To evaluate δA, several contributions must be evaluated.

$$\begin{aligned} \delta A = &\iint\limits_I (\frac{\nabla \eta_{in} \cdot \nabla \eta_{in}}{2}) r dr d\phi + \iint\limits_I (\nabla \eta_{in} \cdot \nabla \eta_{qp}) r dr d\phi \\ &+ \iint\limits_I (\frac{\nabla \eta_{qp} \cdot \nabla \eta_{qp}}{2}) r dr d\phi + \iint\limits_I (\nabla \eta \cdot \nabla h_0) r dr d\phi, \end{aligned} \tag{3.41}$$

The first term in this expression is the area from the induced disturbance around the particle. The divergence theorem requires that this term be equal and opposite to the deviatoric curvature correction to ΔA. The second term is the interaction of two disturbance terms:

$$\iint\limits_{I} (\nabla \eta_{qp} \cdot \nabla \eta_{in}) r dr d\phi = -\frac{\pi}{2} \Delta c_0 a^2 h_{qp}. \tag{3.42}$$

The third term is the area from the particle sourced disturbance, evaluated previously, and the final term is identically zero. Gathering terms, the trapping energy on a curved interface is:

$$\Delta E = \Delta E_{planar} - \gamma \pi a^2 (\frac{3a^2 H_0^2}{4} + \frac{h_{qp} \Delta c_0}{2}), \tag{3.43}$$

where ΔE_{planar} is defined in Eq. 1.13. The trapping energy is reduced by interface curvature. In this discussion, we assumed that the particle's quadrupolar mode was aligned with the saddle shape of the interface. If this were not the case, there would be a capillary torque exerted on the particle which would cause the particle to align [91], and the energy expression becomes:

$$\Delta E = \Delta E_{planar} - \gamma \pi a^2 (\frac{3a^2 H_0^2}{4} + \frac{h_{qp} \Delta c_0}{2} \cos 2\alpha), \tag{3.44}$$

where α is the angle between the quadrupolar rise axis on the particle and the first principal axis. Finally, throughout this discussion, we have assumed that $\theta_{tr} = 90^o$. If that were not the case, in all pre-factors, the radius a should be replaced with $a \sin \theta_{tr}$.

This expression has important consequences for particles for varying curvature fields. We have focused on constant mean curvature interfaces, for which we define the curvature capillary energy at a given position of the interface $E_{cc} = \Delta E - \Delta E_{planar}$:

$$E_{cc} = -\gamma \pi a^2 \frac{h_{qp} \Delta c_0}{2} \cos 2\alpha, \tag{3.45}$$

This predicts a local torque enforcing alignment along the principal axes and a force on the particle propelling it toward high curvature regions. This expression is similar to Equation

1.24, in which one particle moves in the curvature field made by its neighbor. In that case, the neighboring particle made a deviatoric curvature field in the interface $\Delta c_0 = 12 h_{qp} \frac{a^2}{r_{12}^4} cos2(\phi + \alpha_1)$.

3.6.2. Planar disks trajectories with corrected drag coefficient

In Chapter 2, we've studied 10 μm disk migration on curved fluid interfaces formed around a circular micropost [100]. In the work by Yao et. al, the capillary energy that drive the small disks to high curvature region predicts a linear dependence on the deviatoric curvature. Here, we re-plotted one trajectory of a small disk migrating from 10 radii away from the micropost to the edge of a 250 μm diameter micropost in Fig. 3.8. The dotted line shows the energy dissipation using a constant drag coefficient; deviates slightly from linearity in high $a\Delta c$ region. Under lower Reynolds number, Stoke's law governs the resistance of a spherical particle moving in a fluid. However, when the particle approaches a boundary, a rigid wall or a free surface, special care needs to be taken to correct Stoke's resistance [109]. In contrast, the solid line shows the energy dissipation incorporating the hydrodynamic effect due to the near field using Brenner's drag coefficient. Indeed, it is linear all the way to the edge of the micropost. Inset shows the trajectory has a $\frac{1}{4}$ powerless in the far field, which indicates the quadrupolar interaction [49, 110]. Since the correction to the drag coefficient is used in every point from the trajectory, the energy dissipated is greater than the curve with constant drag coefficient, which will predict a slightly higher h_{qp} value for the experiments. Here I also plotted the trajectories previously reported in Chapter 2 using the corrected drag coefficient in Figure 3.9. The inferred h_{qp} ranges from $71 - 101$ nm.

3.6.3. Analogies to electrostatics

Capillary interactions are similar to electrostatic interactions [111]. The electrostatic energy U is often likened to the capillary energy. We explore this concept further for a disk that is attached to a curved interface. First we compare a disk with a circular, pinned contact line to a grounded disk in an external field. Then we consider a disk with a quadrupolar undulated contact line to a disk with a quadrupolar edge potential.

The interface height above the plane of the interface h is analogous to the electrostatic potential ψ^{out} external to the particle. The potential at the particle edge corresponds to boundary conditions on h at the contact line. Particles with finite edge potentials, however, have two quantities that are absent in capillarity; these include the electrostatic potential inside the particle ψ^{in} and the charge density at the contact line σ.

We evaluate U for a disk in an external field of form

$$\psi_{ext} = \psi_0 \, \frac{r^2}{a^2} \cos 2\phi. \tag{3.46}$$

A grounded disk in an external field

Consider a grounded disk with radius a in an unbounded domain I in a far field potential ψ_{ext}. The potentials inside ψ^{in} and outside of the disk ψ^{out} are:

$$\psi^{out} = \psi_0(\frac{r^2}{a^2} - \frac{a^2}{r^2}) \cos 2\phi, \tag{3.47}$$

$$\psi^{in} = 0. \tag{3.48}$$

The total electrical energy U is:

$$U = \frac{1}{2} \iint\limits_{I+P} \rho(\mathbf{r})\psi(\mathbf{r}) dA \tag{3.49}$$

where $I + P$ is the entire domain, dA is an area element, and $\rho(\mathbf{r})$ is the charge density in the system. However, the sole charge is σ, the induced charge on the surface of the disk,

$$\sigma = \mathbf{e_r} \cdot (-\epsilon \nabla \psi(\mathbf{r} \geq \mathbf{a}))|_{r=a} = -4\epsilon\psi_0 a^{-1} \cos 2\phi, \tag{3.50}$$

where $\mathbf{e}_r$ is the unit normal pointing away from the disk, and ϵ is the relative permittivity of the disk to that of free space. The expression for U can be recast and evaluated:

$$U = \frac{1}{2}\int_a^\infty \int_0^{2\pi} \sigma\delta(r-a)\psi(\mathbf{r})rd\phi dr = 0, \tag{3.51}$$

where δ is the Dirac delta function. Recalling that, for a grounded disk, $\psi(r = a) = 0$, U is zero. This result agrees with the capillary energy we have derived for circular, pinned contact lines on curved interfaces, for which the capillary energy is zero. In particular, there are no terms in ψ_0^2, or analogously $(a^2\Delta c_0)^2$ whose contributions have been the subject of discussion [100, 108, 112].

A disk with an edge potential

Consider a dielectric disk of radius a with edge potential $\psi(r = a) = q\cos 2\phi$ in an unbounded domain with far field potential ψ_{ext}. Here, ψ^{in} is finite, as the disk polarizes owing to the edge potential. This finite potential has no analogy in the capillary problem; this will propagate throughout the calculation of U. For simplicity, we consider a disk and external domain of the same relative permittivity. The electric potentials inside and outside the disk are subject to the boundary conditions:

$$\psi^{in}\big|_{r=a} = \psi^{out}\big|_{r=a}, \tag{3.52}$$

$$\mathbf{e}_r \cdot (\nabla\psi^{in} - \nabla\psi^{out})\big|_{r=a} = \frac{\sigma}{\epsilon}. \tag{3.53}$$

with solutions:

$$\psi^{in} = q\frac{r^2}{a^2}\cos 2\phi, \tag{3.54}$$

$$\psi^{out} = q\frac{a^2}{r^2}\cos 2\phi + \psi_0(\frac{r^2}{a^2} - \frac{a^2}{r^2})\cos 2\phi. \tag{3.55}$$

Notice that ψ^{out} has the same form as h for a particle with a pinned, quadrupolar contact line on a curved interface. The corresponding egde charge density is:

$$\sigma = 4\epsilon \frac{(q - \psi_0)}{a} \cos 2\phi. \tag{3.56}$$

Since this is the sole charge in this system, U is:

$$\begin{aligned} U &= \frac{1}{2} \int_0^\infty \int_0^{2\pi} \sigma \delta(r - a) \psi(\mathbf{r}) r d\phi dr \\ &= -2\pi\epsilon\psi_0 q + \pi\epsilon q^2 + \pi\epsilon q^2. \end{aligned} \tag{3.57}$$

We break this expression into three terms; the first two are analogous to the net capillary energy for a particle on a curved interface; these include the curvature capillary energy E_{cc} in Equation (3.45) and the self energy owing to the particle distortion in Equation (1.13). The third term, of the same form as the self energy, is not present in the capillary energy. To understand the origin of this term, we use Gauss's law to recast U:

$$U = -\frac{\epsilon}{2} \oint\limits_{\partial(I+P)} (\psi \nabla \psi) \cdot \mathbf{n} \, dl + \frac{\epsilon}{2} \iint\limits_{I+P} (\nabla \psi)^2 dA, \tag{3.58}$$

where the second integral can be decomposed into the domains inside and outside of the disk:

$$\iint\limits_{I+P} (\nabla \psi)^2 dA = \iint\limits_{P} (\nabla \psi^{in})^2 dA + \iint\limits_{I} (\nabla \psi^{out})^2 dA, \tag{3.59}$$

The contribution to U integrated over P is:

$$\frac{\epsilon}{2} \iint\limits_{P} (\nabla \psi^{in})^2 dA = \epsilon\pi \int_0^a \frac{4q^2}{a^4} r^3 dr = \epsilon\pi q^2, \tag{3.60}$$

This is the energy required to polarize the disk. This has no analogy in the capillary problem. The process of charging the particle, which generates the potential inside of the particle, differs from the process of undulating the contact line, which relies on wetting energies or pinning sites. When this term is disregarded, the analogy between electrostatics and capillarity holds.

3.6.4. Key findings on curved interfaces

Spherical particles on curved interfaces have been analyzed in several limits. Particles with contact angle of 90° on bounded cylindrically-shaped interfaces are predicted to induce quadrupolar distortions that drive assembly [50]. Particles with contact lines at equilibrium on unbounded interfaces are predicted either to interact with capillary energies that are quadratic in the deviatoric curvature [92] or to fail to interact [108], depending on the treatment of the far field boundary in evaluating the interfacial area. Since contact line pinning is ubiquitous, this case is difficult to interrogate in experiment. Finally, particles with pinned contact lines on unbounded interfaces have been addressed. This case, which is identical to the case of a disk on the interface except for the constant wetting energy terms, is discussed in section 3.6.1.

Structures that clearly reveal quadrupolar symmetries were observed on interfaces with complex curvatures. The interfaces were formed by placing droplets of oil on surfaces with patterned hydrophobic surfaces; the resulting interfaces had constant mean curvature but spatially varying deviatoric curvatures [86]. Charged spherical microparticles on these interfaces form a square lattice characteristic of capillary quadrupolar interactions balanced by electrostatic repulsion. The square lattice is strained, consistent with the particle quadrupolar distortion aligning along the spatially varying principle axes. At particle densities greater than 0.33, hexagonal lattices begin to appear, characteristic of colloidal crystals at interfaces absent strong quadrupolar modes.

Spherical particles also respond dynamically to curved interfaces. Silica colloids at air-water interfaces displayed different behaviors depending on particle wetting [52]. For contact angles up to 5°, particles settle to the minimum interface height, consistent with weak capillary interaction. For contact angle of $\sim 30^\circ$, particles migrate along the principal axis to equilibrium sites.

We have studied the dynamics of microparticles on curved oil-water interfaces for several particle shapes including disks [100], spheres [108] and cylinders [20]. These experiments are performed on interface shapes molded around a micropost. A vertical cylindrical micropost hundreds of microns in diameter is fabricated from epoxy resin on a silicon substrate. The post is surrounded by a low ring, located several capillary lengths away. This space is filled with water so that the contact line pinned at the edge of the micropost. The maximum slope of the interface occurs at the micropost given by the angle $\psi \sim 15^\circ$ with the horizontal. A layer of hexadecane is gently placed over this water layer to prevent evaporation, dampen stray convection, and to allow particles to be introduced to the interface via sedimentation through the oil. This apparatus is placed under an optical microscope and imaged from above; particle trajectories are recorded and analyzed. Near the post, in the region of interest, the interface height decays logarithmically with distance L from the center of the micropost. In this region, the mean curvature is negligible and the deviatoric curvature Δc_0 is known, $\sim -L^{-2}$. Particles attach to the interface and migrate along the curvature gradient to sites of high deviatoric curvature, in agreement with the predictions in Equation 3.45. Results are summarized in Figure 3.10, including time-stamped images of typical trajectories (left-most column), the energy dissipated along a particle path (center column) and observed power laws implied by the equality of viscous drag and the curvature capillary force (right-most column). The energy dissipated versus deviatoric curvature is linear in Δc_0 with coefficient of linear regression $R^2 = 0.999$ or better. As the cylindrical microparticle migrates, it aligns its quadrupolar rise axis with the rise axis toward the micropost, in agreement with the capillary torque implied by Equation 3.45. Recent work reveals analogies between capillary migration on curved fluid interfaces and Janus bead migration on tense lipid bilayer vesicles. The tense vesicle shape obeys the Young-Laplace equation. The particle migrates along curvature gradients on GUVs stretched to impose curvature fields, with energy dissipated linearly in the deviatoric curvature [21]. For all of these studies, the interface slope is small and the particle is much smaller than the micropost. In recent work, we have challenged these assumptions. That discussion is described in Chapter 4.

3.6.5. Summary

The discussion of lattice formation by repulsive particles on interfaces with weakly varying deviatoric curvatures is one interesting limit for structure formation on curved interfaces. Particles formed a square lattice, and neither assembled nor migrated. Structure formation on interfaces with strong curvature gradients is another interesting limit. For example, consider cylindrical particles on an interface pinned to a square micropost (see Fig. 3.10b). Curvature gradients near the corners are very steep; particles migrate along curvature gradient lines to form trapped structures influenced by the curvature gradients, and particle pair interactions, and potentially by multibody effects and local non-linearities. Between these limits, tunable structures informed by curvature gradients may be formed. This is a focus of ongoing work.

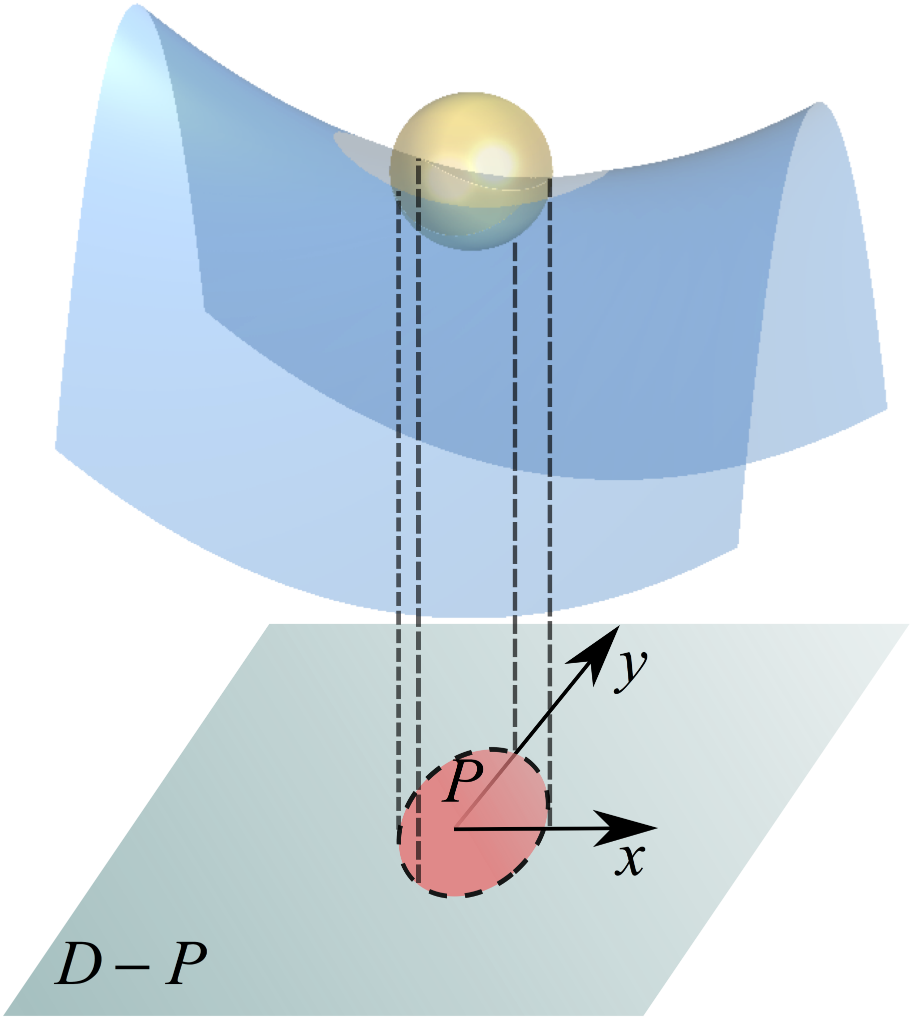

Figure 3.1: Schematic representation of a sphere trapped at a curved interface and its mapping to the tangent plane.

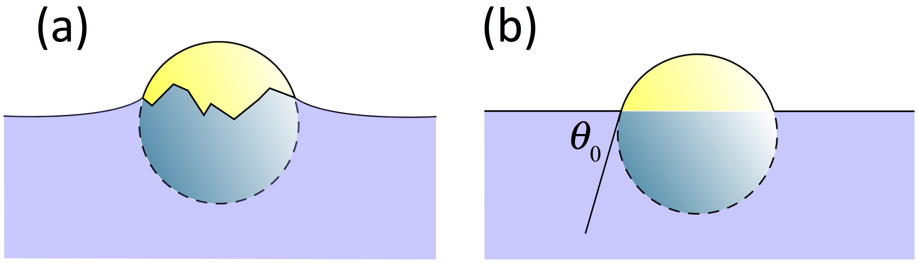

Figure 3.2: Schematic representation of a sphere trapped at an interface with (a) a pinned undulated contact line and (b) an equilibrium wetting boundary condition with a contact angel θ_0.

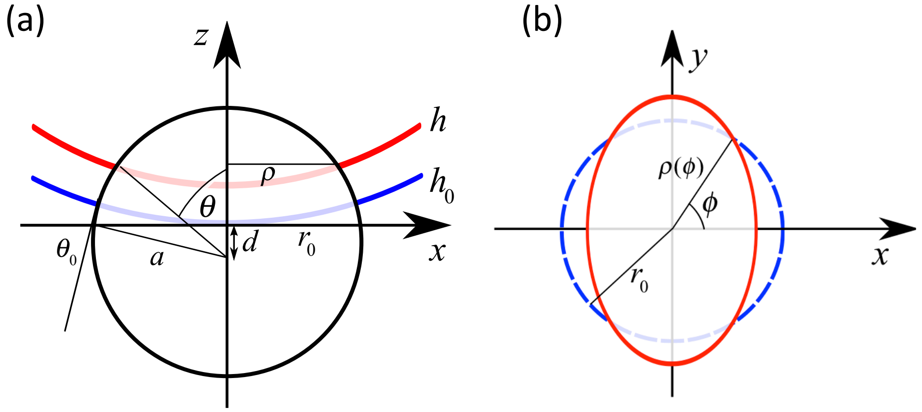

Figure 3.3: (a) Schematic view of a sphere of radius a at a liquid interface in $x-z$ plane, where θ_0 and r_0 are the contact angle and the radius of the contact line for a flat interface. h_0 describes a curved interface without a particle, $h = h_0 + \eta$ accounts for the height of interface in presence of the particle. θ is the polar angle of the deformed contact line, and ρ is its radial position. (b) Schematic view of the contact lines in $x-y$ plane in flat (in blue) and curved interfaces (in red).

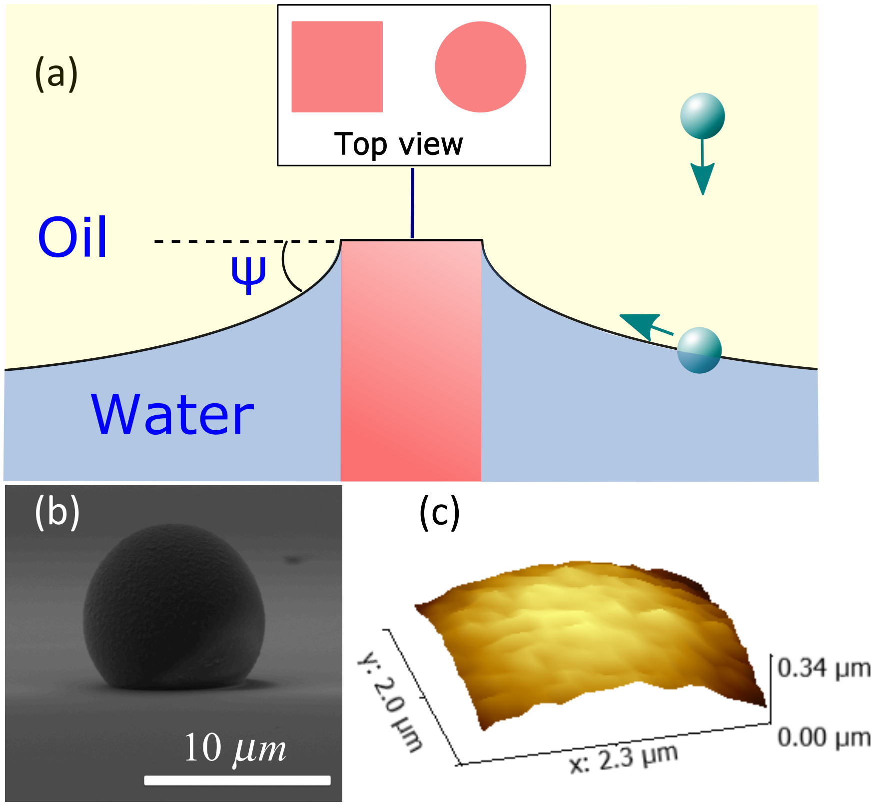

Figure 3.4: (a) Schematic view of curvature field around the micropost. (b) SEM image of a microsphere and PDMS negative of the air-water interface showing particle roughness and (C) AFM reveals nanoscopic roughness of the sphere surfaces with RMS values ranging of $15 - 21$ nm.

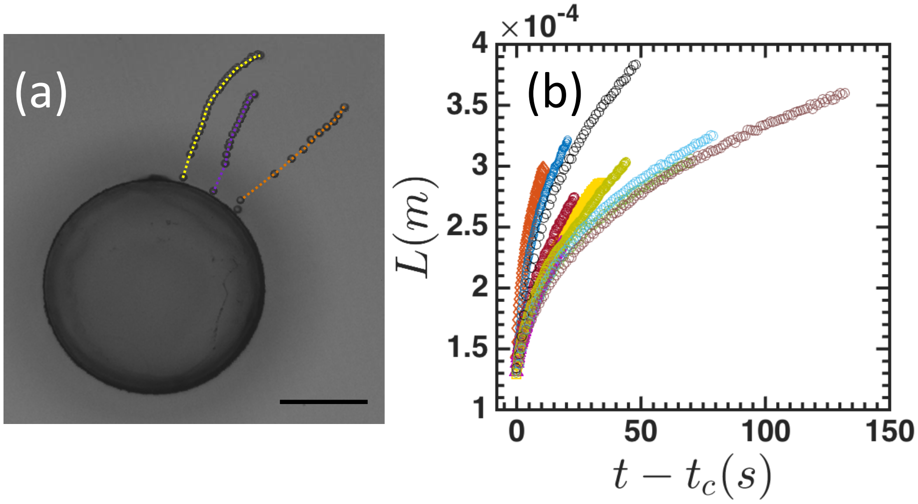

Figure 3.5: (a) Time stamped image of microspheres trajectory (scale bar = 100 μm). (b) Trajectories for spheres migrating on the interface. Colors for trajectories in (b) correspond to trajectories of similar colors in (a).

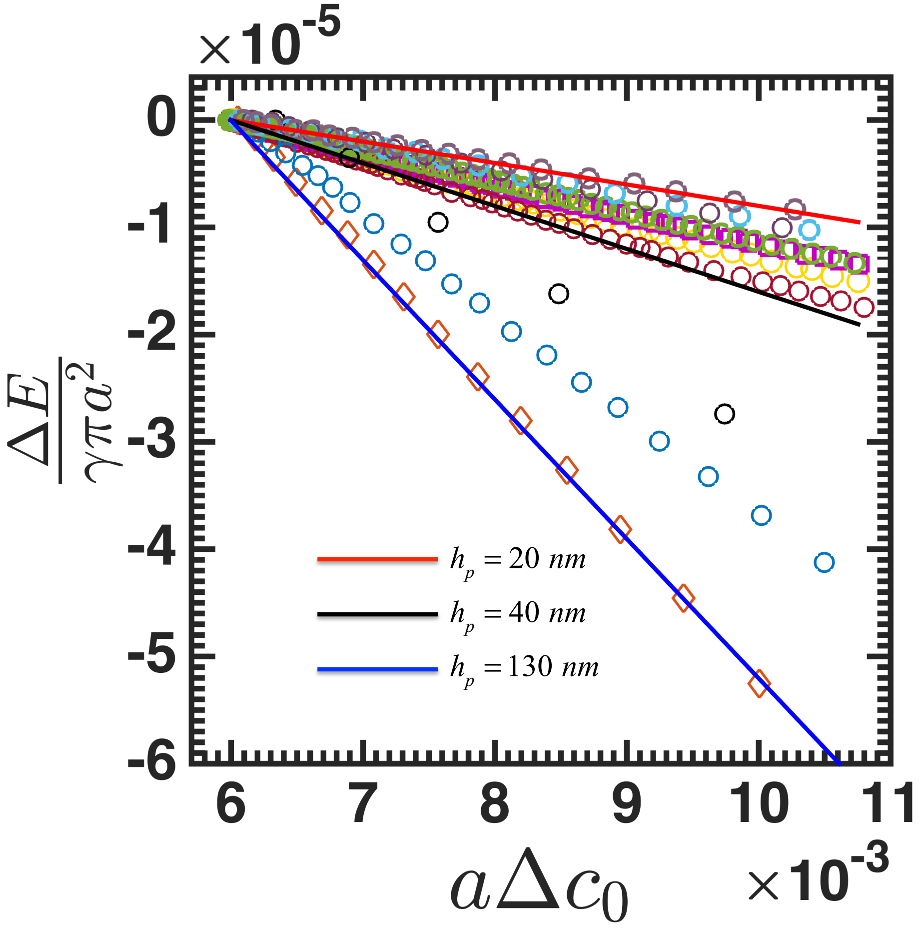

Figure 3.6: Comparison of predicted curvature capillary energy for particles with pinned contact lines (Eq. 3.8) (solid lines) against those extracted from experiment for trajectories in Fig. 3.5(b) for isolated particles (symbols). The colors correspond to the trajectories in Fig. 3.5(b). The linear fit is excellent for all trajectories, with coefficient of linear regression $R^2 = 0.999$ for the worst case.

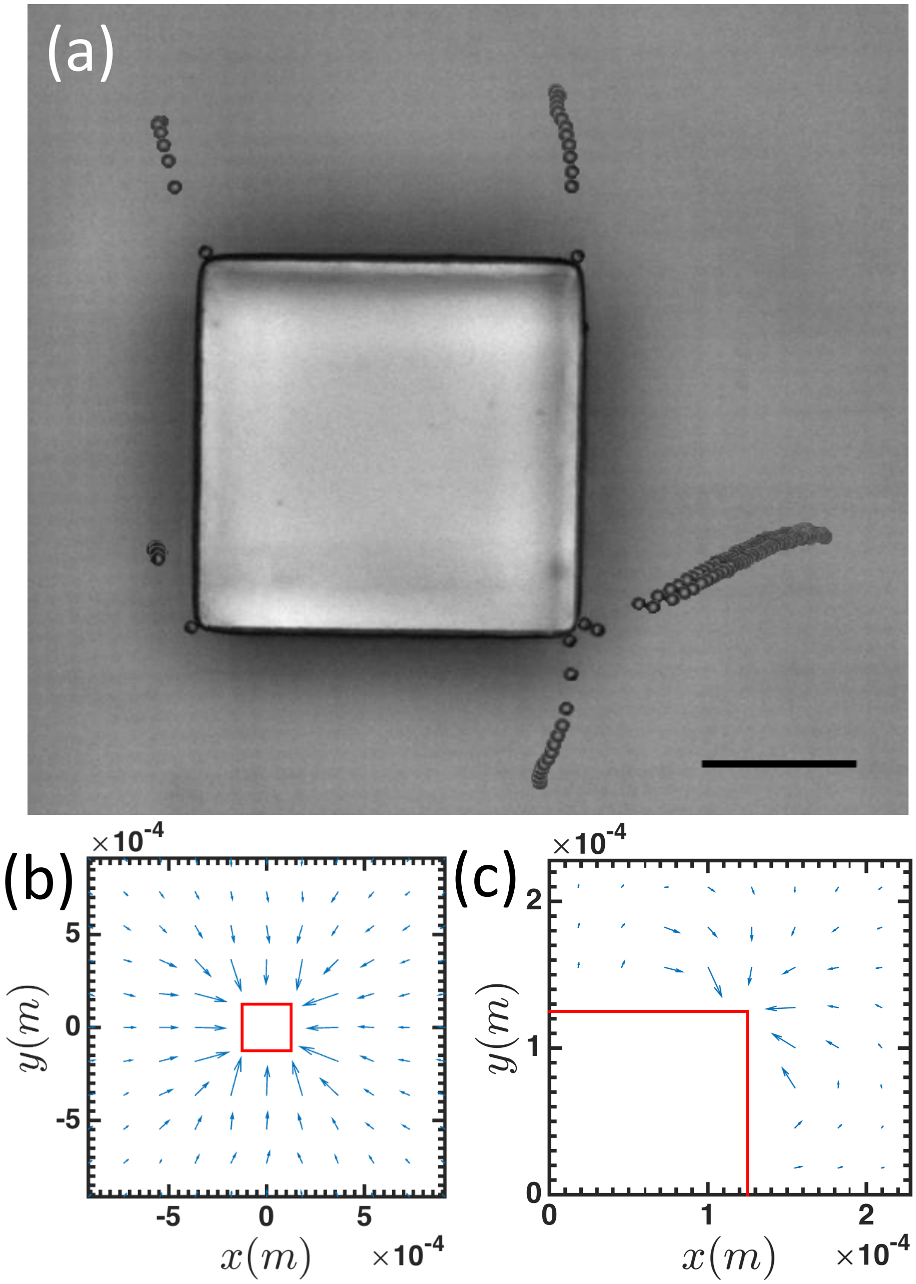

Figure 3.7: (a) Time-stamped trajectories of microspheres around a square post illustrating that the microspheres follow complex trajectories as defined by the deviatoric curvature field (the scale bar is $100\mu m$). Numerically evaluated curvature gradient around (b) a square post and (c) a corner of the square post. The arrows scaled with the magnitude of deviatoric curvature gradient.

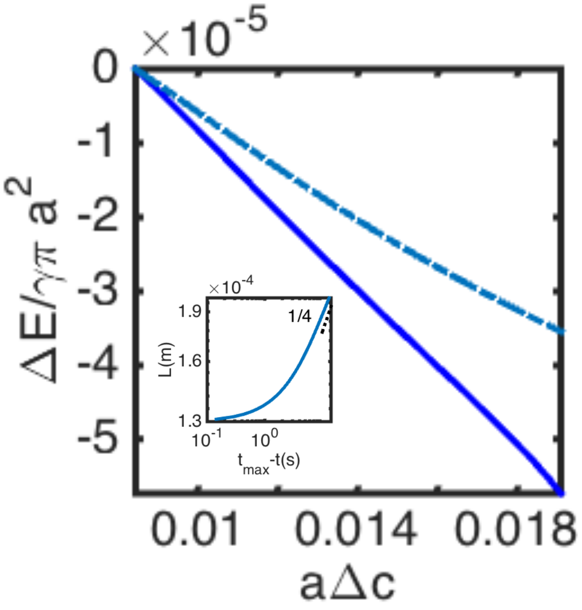

Figure 3.8: Energy dissipated of a microdisk ($2a$= $10\mu m$) on a curved interface (R_m = $125\mu m$) from 10 radii away to the contact of the micropost using Brenner's drag coefficient [109]. Dotted blue curve shows the energy dissipation using a constant drag coefficient, $C_D = 1$. Solid blue curve shows the energy dissipation using Brenner's drag coefficient [109]. Inset: plot presents the separation distance versus the contact time and the dotted line shows a slope of $\frac{1}{4}$.

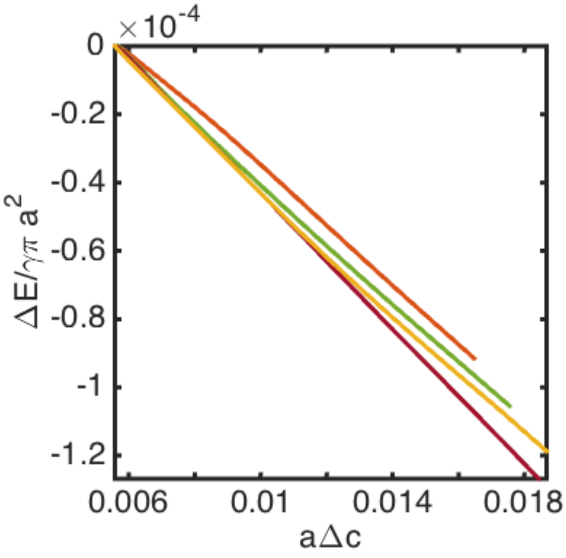

Figure 3.9: Energy dissipated of microdisks (a= $5\mu m$) on a curved interface ($R_m = 125\mu m$) for the full trajectory (25 radii away) to the contact of the micropost using Brenner's drag coefficient [109]

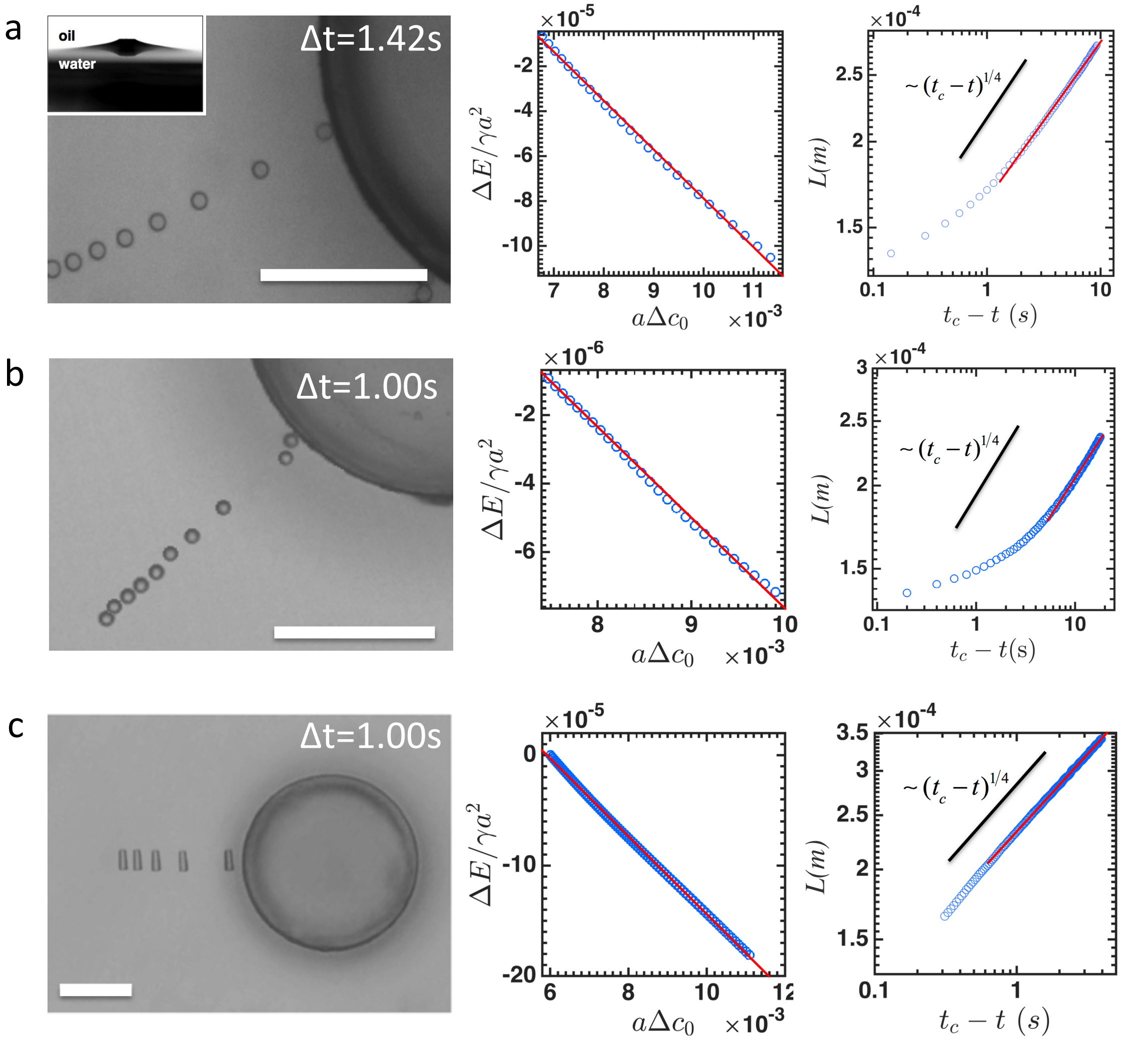

Figure 3.10: Curvature capillary migration of disk (a), sphere (b) and cylinder (c). Left-most column shows the time-stamped image of trajectories of microparticles migrating toward a circular micropost. Center column shows curvature capillary energy for particles are linear in deviatoric curvature. Right-most column plots power law dependence of center-to-center separation distance (L) versus contact time. (a) Inset: side view of the curved interface. Scale bars are 100 μm. (a) Reprinted from Reference [100], copyright (2015), with permission from Elsevier. (b) Adapted from [108] with permission from The Royal Society of Chemistry. (c) Reprinted with permission from [20], copyright (2011), National Academy of Sciences.

CHAPTER 4 : Curvature capillary repulsion: Large disks at curved interfaces

4.1. Introduction

Directed assembly of colloids is an exciting field in materials science to form structures with new symmetries and responses. We have been studying how interface curvature can be used in new ways to guide structure formation. On a fluid interface, the area of the deformation field around adsorbed microparticles depends on interface curvature; particles move to minimize the excess area of the distortions that they make in the interface. For particles that are sufficiently small, this area decreases as particles move along principle axes to sites of high deviatoric curvature. We have studied this migration for microparticles on a curved host interface with zero mean curvature created by pinning an oil-water interface around a micropost. Here, on a similar interface, we demonstrate capillary curvature repulsion, that is, we identify conditions in which microparticles migrate away from high curvature sites. Using theory and experiment, we discuss the origin of these interactions and their relationship to the particle's undulated contact line. We discuss the implications of this new type of interaction in various contexts from materials science to microrobotics.

In this chapter, I report work that will be published with co-authors Giulia Bigazzi, Dr. Lu Yao and Dr. Nima Sharifi-Mood. These results were obtained in collaboration. In particular, in this study, I performed the experiments and lead the analysis.

4.2. Background

Fluid interfaces are excellent sites to organize microscale particles with potential to form new functional structures. Microparticles are firmly attached to fluid interfaces by significant trapping energies associated with the elimination of a small patch of interface by the particle adsorption. On planar interfaces, crystalline packing of microparticles can be achieved, e.g., by exploiting electrostatic repulsion and weak confinement in a gravitational well [30]. More complex arrangements can be achieved by a number of routes. For example, if complex fluids like nematic liquid crystals are used as subphases, repulsion between the colloids owing to their topological defects can also form crystalline packings [113], and elastic energies in the nematic subphase can guide complex open structures to form [24]. Particle shape can also dictate the symmetries of structures at fluid interfaces; the capillary energy, given by the product of surface tension and area, near a particle depends on features like particle aspect ratio and the presence of sharp edges. Thus, capillary interactions depend on particle shape and orientation, so particles assemble in preferred configurations, e.g., uncharged ellipsoids in side-to-side configurations [68, 72] and cylindrical microparticles in end-to-end configurations [91, 64, 65]. In this communication, we discuss recent studies of capillary assembly at curved fluid interfaces, introduce the new concept of curvature capillary repulsion, and conclude with a broader vision of how these interactions and analogous interactions in other soft matter hosts can be exploited in a number of contexts.

On a curved fluid interface, the excess area around a colloid depends on the underlying interface shape. As a result, curvature can act as an "external field" to dictate particle behavior. In prior work, we have reported capillary curvature attraction in the limit of small particle radius to interface radius of curvature [20, 100, 108, 114]. Here we report more complex behavior that emerges when this limit is relaxed. To situate this result, we first briefly recapitulate the main concepts that explain curvature capillary attraction. We then motivate our discussion of curvature capillary repulsion.

The phenomenon of capillary curvature attraction is now well established, having been reported for microcylinders [20], microdisks [100], and microspheres [108]. These studies were performed for particles on a host interface created by pinning a water interface around a micropost of height H_m, radius R_m, with interface slope at the micropost of $-\tan\Psi$, where Ψ is roughly 15°. A layer of hexadecane is gently placed above this water layer to minimize fluxes from evaporation. A schematic of this arrangement is shown in Fig. 4.1a. Particles are introduced to this oil super-phase sediment under gravity and attach to the interface, avoiding the use of spreading solvent. The interface slope is small, and all experiments are performed at distances from the center of the micropost L small compared to the capillary length. Similar migrations are observed for cylinders, spheres and disks [114]. A typical trajectory for a disk migrating on the curved fluid interface is shown in Fig. 4.1c. The particle attaches to the interface at some distance from the micropost. It then migrates along paths radial to the micropost until contact. For this situation, the interface shape is governed by the Laplace equation. The host interface shape $h(L)$ in the absence of the particle is simply

$$h(L) = H_m - R_m \tan\Psi \ln(\frac{L}{R_m}) \tag{4.1}$$

The interface shape has zero mean curvature, and proves a versatile platform for investigation of curvature capillary effects. This expression can be expanded in a polar coordinate system (r, ϕ) defined in the plane tangent to the interface in powers of $\lambda = \frac{a}{L_0}$, where a is the particle radius and L_0 is the distance from the post center where a particle adsorbs. To leading order, the local host interface height above this reference plane has the form:

$$h^0(r, \phi) = \frac{\Delta c(L_0)}{4} r^2 \cos 2\phi \tag{4.2}$$

This is a saddle surface, characterized by the deviatoric curvature $\Delta c = \frac{1}{R_1} - \frac{1}{R_2}$, where R_1 and R_2 are the principal radii of curvature at L_0. When colloidal particles attach to the interface, they make distortions in the interface. Colloidal particles typically have pinned contact lines [53, 115, 57]; these contours can be described in terms of an expansion in Fourier modes. Each mode excites an interfacial distortion given by the corresponding mode in a multipole expansion. For particles with negligible body forces and body torques, the leading order Fourier mode has quadrupolar symmetries [61, 114], so the contact line, to leading order is described:

$$h^{particle}(r = a, \phi) = h_2 \cos 2(\phi + \alpha_2) \tag{4.3}$$

where h_2 is the magnitude of the quadrupolar mode, and the phase angle α_2 is zero when the quadrupolar rise axis aligns with rise axis of the saddle surface. The interfacial distortion associated with this contour couples with the interface curvature in a manner akin to a charged multipole in an external electric field. For a small particle [100, 114], the capillary energy for a microparticle on such a curved interface differs from the case of a planar interface:

$$E(L_0) = E_{planar} - \gamma\pi a^2 \frac{h_2 \Delta c(L_0)}{2} \cos 2\alpha_2 \tag{4.4}$$

This expression predicts a torque and a force; it indicates that particles decrease their capillary energy by rotating the particle to align its quadrupolar rise along the rise axis of the host interface ($\alpha_2 = 0$), as has been observed for cylindrical microparticles [63, 20], and by migrating to sites of high curvature.

This predicted linear dependence of the capillary energy on the deviatoric curvature at the particle center of mass can be compared to experiment like that presented in Fig. 4.1 c-d. The Reynolds number Re= $\frac{av\rho}{\mu} \sim 10^{-5}$ for a typical trajectory, where a is the characteristic length of the particle, v is the particle velocity, ρ is the fluid density, and μ is the fluid viscosity. Thus, the particles migrate in creeping flow, and the energy dissipated along a trajectory can be extracted by integrating along a particle path.

$$\begin{aligned} \Delta E \quad &= \gamma\pi a^2 \frac{h_2}{2}(\Delta c(L_{0,f}) - \Delta c(L_{0,i})) \\ &= 6\pi\mu a \int_{s_i}^{s_f} C_D v ds \end{aligned} \tag{4.5}$$

We have performed this integration two ways. We have truncated the particle trajectory ~ 10 particle radii from the post to avoid hydrodynamic interactions with the wall, adopting Lamb's drag coefficient on a disk [98]. We have also integrated over the energy dissipated over the entire trajectory, adopting drag coefficients for disks near bounding surfaces in Fig. 4.1c (details in Appendix A) [116]. These graphs confirm the predicted linear dependence of the migration energy on the local deviatoric curvature, and allow the magnitude of $h_2 \sim 71 - 101$ nm to be inferred. From (4.4), the capillary force can be found:

$$F_{cap} = \gamma \pi a^2 \frac{h_2}{2} \frac{d\Delta c}{dL_0} \delta_L \tag{4.6}$$

A balance of this force and viscous drag predicts a power law dependence in L_0 vs. $(t_f - t)$, for particles far enough from the post to neglect hydrodynamic interactions, where t_f is the time that the particle ceases its migration. This power law is apparent in the data (Fig. 4.1d). Note that the trajectories are non-Brownian; typical energy dissipated along a trajectory is of order $10^5 k_B T$. Typical capillary forces magnitudes are $\sim$ 10pN for a disk of radius 10 μm for the range of h_2 inferred. The gravitational force on the particle can also be estimated [42, 117]. The particle migrates to minimize its potential energy, constrained to move along the interface:

$$E_g = \left[(\rho_p - \rho_1)\Phi_1 + (\rho_p - \rho_2)(1 - \Phi_1) \right] V_p g h \tag{4.7}$$

where ρ_p is the particle density, ρ_i is the density of water (i=1) and oil (i=2), and Φ_1 is the volume fraction of the particle immersed in the aqueous phase, and V_p is the volume of the particle. The corresponding force owing to gravity is:

$$F_g = -[(\rho_P - \rho_1)\Phi_1 + (\rho_P - \rho_2)(1 - \Phi_1)] V_P g \frac{\delta h}{\delta z} \tag{4.8}$$

The ratio of the gravitational force to the capillary force is between 10^{-5} to 10^{-4}. The negligible contributions by gravity is also reflected in the small value for the Bond number, a dimensionless number defines the contribution of gravitational forces to surface tension forces, $Bo = \frac{\Delta \rho g L^2}{\gamma} = 1.3 \times 10^{-6}$.

What if we consider larger particles or smaller posts? What new phenomena emerge? Such a trajectory is shown in Fig. 4.1e for a disk 125 μm in diameter on an interface similar to that in Fig. 4.1c. This larger particle moves along a roughly radial path *away* from the post. Here, we delve into the origin of this apparent curvature repulsion, and find a rich variety of behaviors.

4.3. Theory

We have considered several potential sources of this repulsion. Gravitational forces on interfacially-trapped particles remain small, even for these larger particles. Interactions with the micropost can also be considered. Equation (4.4) was derived using the method of reflections [77, 99], in which the micropost determines the host interface shape near the particle, and the disturbance made by the particle is determined assuming a pinned contact line. The curvature-dependent part of the energy associated with this disturbance is reported in (4.4). A similar calculation can be done to understand interactions of the particle-sourced disturbance with the micropost. However, the energy associated with these interactions is negligible, with largest contribution being two orders of magnitude smaller than the leading order term (see Appendix A). Finally, we consider the role of higher order Fourier modes in the particle's distorted contact line, which can couple with higher order modes in the local description of the host interface. Theory presented below shows that the importance of these modes increase with λ; we present a simple theory based on these interfacial details, and compare it favorably to the experiments.

Here, we derive a more general expression for a particle interacting with the host interface shape. The entire host interface profile is described by (4.1). When a microdisk attaches to this interface at some distance L_0 from the center of the post, the disturbance created by the particle decays monotonically over distances comparable to the particle radius a. To understand the energy associated with this deformation, we first find an expression for the local shape of the host interface at L_0. In the limit of $\lambda = \frac{a}{L_0} < 1$ we expand (4.1) in a power series in a local coordinate x, y, z with origin at L_0 (Fig. 4.1b), where the height is defined as the distance above the plane tangent to the interface. We perform a coordinate transformation, using the following relationship between the two coordinates,

$$L^2 = X^2 + Y^2 \tag{4.9}$$

$$X = L_0 + x \tag{4.10}$$

$$Y = y \tag{4.11}$$

$$Z = Z_0 \tag{4.12}$$

where X, Y, Z are the coordinate centered at the bottom center of the micropost, Z_0 is the interface height at the particle center of mass, and h^0 is the height of the interface above Z_0. Expanding the natural log term in (4.1), and scaling heights with a, the dimensionless interface profile is

$$\begin{aligned} \widetilde{h}^0 = \quad & \tfrac{1}{2}\tfrac{\lambda R_m \tan\psi}{L_0}(\widetilde{x^2} - \widetilde{y^2}) - \tfrac{\lambda^2 R_m \tan\psi}{L_0}(\tfrac{\widetilde{x^3}}{3} - \widetilde{x}\widetilde{y^2}) \\ & + \tfrac{1}{4}\tfrac{\lambda^3 R_m \tan\psi}{L_0}(\widetilde{y^4} + \widetilde{x^4} - 6\widetilde{x^2}\widetilde{y^2}) + ... \end{aligned} \tag{4.13}$$

where $\widetilde{h}^0 = \frac{h}{a}$, $\widetilde{x} = \frac{x}{a}$, $\widetilde{y} = \frac{y}{a}$. Equation (4.13) can be recast in a polar coordinate $\widetilde{x} = \widetilde{r}\cos\phi$, $\widetilde{y} = \widetilde{r}\sin\phi$:

$$\widetilde{h}^0 = \frac{1}{2}\frac{\lambda R_m \tan\psi}{L_0}\widetilde{r}^2\cos 2\phi - \frac{1}{3}\frac{\lambda^2 R_m \tan\psi}{L_0}\widetilde{r}^3\cos 3\phi + \frac{1}{4}\frac{\lambda^3 R_m \tan\psi}{L_0}\widetilde{r}^4\cos 4\phi + ... \tag{4.14}$$

Noting that $\Delta c = \frac{2R_m tan\psi}{{L_0}^2}$ the local description of the host interface shape becomes,

$$h^0 = \frac{1}{4}\Delta c r^2 \cos 2\phi - \frac{1}{6}\frac{\Delta c}{L_0} r^3 \cos 3\phi + \frac{1}{8}\frac{\Delta c}{{L_0}^2} r^4 \cos 4\phi + ... \tag{4.15}$$

A circular disk on the fluid interface disturbs the interface height owing to its pinned contact line; the particle-sourced disturbance owing to the pinned, undulated contact line can be expressed in terms of a multipole expansion:

$$h^{particle} = h_2\frac{a^2}{r^2}\cos 2(\phi + \alpha_2) + h_3\frac{a^3}{r^3}\cos 3(\phi + \alpha_3) + h_4\frac{a^4}{r^4}\cos 4(\phi + \alpha_4) + ... \tag{4.16}$$

where the subscripts 2, 3, and 4 indicate mode of deformation, e.g., the quadrupolar, hexapolar, and octopolar modes of deformation and α_n is the phase angle for mode n. To find the interface shape for the particle attached to the interface, we note that the solution takes the form of a multipole expansion, and apply the pinning boundary condition,

$$h(r=a,\phi) = h^{particle}(r=a,\phi) \tag{4.17}$$

and require that, far from the particle, the interface recovers the host interface shape,

$$\lim_{r\to\infty} h(r,\phi) = h^0 \tag{4.18}$$

The full expression of the resulting interface profile near the particle is

$$\begin{aligned} h = \quad & h^0 + h^{particle} - \frac{1}{4}\frac{\Delta c a^2}{r^2}a^2\cos 2(\phi+\alpha_2) + \frac{1}{6}\frac{\Delta c}{L_0}\frac{a^3}{r^3}a^3\cos 3(\phi+\alpha_3) \\ & -\frac{1}{8}\frac{\Delta c}{{L_0}^2}\frac{a^4}{r^4}a^4\cos 4(\phi+\alpha_4) + ... \end{aligned} \tag{4.19}$$

The capillary energy associated with the particle on this interface is the product of the constant interfacial tension and the change in surface area owing to particle attachment. The details of this calculation are reported in our prior work on the quadrupolar disturbance, so details are not given here. The capillary energy around the particle is:

$$\Delta E = \gamma\pi a^2\frac{\Delta c}{2}\left\{-h_2\cos 2\alpha_2 + \lambda h_3\cos 3\alpha_3 - \lambda^2 h_4\cos 4\alpha_4 + ...\right\} + \text{self terms} \tag{4.20}$$

where the self terms indicate interactions quadratic in the magnitude of each mode that would occur for particles on a planar interfaces, which are independent of interface shape.

4.4. Experimental

We perform two series of experiments. We study disks of diameter 25 μm and 150 μm and vary the micropost diameter while fixing its height and the slope of the interface at the micropost's edge. For each experiment, we compute the Bond number Bo; for these systems Bo ranges from 1 $\times 10^{-5}$ to 6 $\times 10^{-5}$.

4.4.1. Particle fabrication

Epoxy resin particles are fabricated using standard lithographic techniques. A negative tone photoresist, SU-8 (MicroChem Corp.), is spin-coated onto a chrome-sputtered silicon wafer. After soft baking at 95°C, the photoresist is exposed to UV light on a tabletop mask aligner (OAI Model 100) through a mask with an array of circular holes. The photoresist is cross-linked on a hot plate at 95°C. The sample is then developed in SU-8 developer solution to dissolve the unexposed region, leaving solid circular disks on the wafer. The disks are released from wafer by sonicating in chrome etchant. Subsequently, particles are cleaned, washed with water and isopropanol, and stored in hexadecane for further uses. The disk particles aspect ratio is 0.2, thickness to diameter.

4.4.2. Molding the Interface

We fabricate the vessel used to mold the fluid interface using lithographic techniques given in detail in a previous publication [20]. In short, three layers of lithography are built on a silicon wafer: a wetting layer of an array of microcylinders of height 5 μm, a bounding ring of radius 1.27 cm and height 25 μm, and a micropost of height 250 μm. The micropost height H_m in all the experiment is 200 μm. Microposts of varying radii are fabricated, including 47 μm, 57 μm, 125 μm, 250 μm, and 600 μm.

4.4.3. Experimental Protocol

We add water to the vessel to pin at the top edge of the micropost and at the edge of the bounding ring. The interface slope is determined by the volume of water; the volume is sufficiently large and the ring is sufficiently far from the micropost that the mean curvature of the interface is negligible. In these experiments, the pinning angle, ψ, is kept between $15^\circ \leq \psi \leq 20^\circ$. This is the maximum slope of the interface. We then carefully place a layer of hexadecane onto the water subphase to form a curved oil-water interface. We introduce particles to the interface by gently adding drops of microparticles dispersed in hexadecane to the superphase where they slowly sediment and attach to the interface. We study trajectories after this attachment event. The vessel is placed under an upright microscope (Zeiss M1m) in a reflective mode. Particle trajectories are recorded using a high resolution camera at rate of 0.141 or 0.200 ms per frame.

4.5. Results and Discussions

We study microparticle migration on well-defined curved oil-water interfaces formed by pinning water around a micropost. We define $\lambda^* = \frac{a}{R_m}$; this parameter is the upper bound to λ around any post. Typical trajectories for disks of 25 μm in diameter on the curved interface molded by a 57 μm micropost are reported in Fig. 4.2, for which λ^*=0.44. Three particles approach the micropost with distinct behaviors. The first disk migrated towards the micropost and stopped at center-to-center distance $L_0(t_f)$=50.1 μm from the post (Fig. 4.2a). The second disk migrated at a much slower rate to the micropost and stopped at $L_0(t_f)$=128.0 μm (Fig. 4.2b). The third disk migrated along curvature gradients all the way to the edge of the micropost (Fig. 4.2c). Interestingly, upon the attachment of the third disk (green cross mark), the nearby disk (red triangle) was repelled at distances of a few particle radii by the incoming particle. It moved away from the incoming particle by orbiting around the post, i.e. keeping a fixed distance from the post.

There is evidence of competing modes when the trajectories are inspected for power law dependencies. Trajectories in Fig. 4.2 are shown in a log-log as insets. In these insets, the abscissa is $t_f - t$, and vertical axis is $L_0/(R_m + a)$, a normalized center-to-center distance which is unity for particles attached to posts. Far from the post, all three disks obey a power law of $\frac{1}{4}$, indicating a dominant quadrupolar mode. The trajectories deviate strongly from this power law for $L_0/(R_m + a) \sim 3$, or $L_0 < 120$ μm and $\lambda > 0.1$, consistent with contributions from other modes. These deviations differ from each other; two of the trajectories steepen, while the other plateaus at distances too far from contact to attribute to hydrodynamic interactions.

Experiments with larger disks (2a=150 μm) also reveal interesting behaviors. Images of the disks on planar interfaces are shown in Fig. 4.3a and b. The disks are quite rough, with strong distortion apparent near their edges in the interferogram; the interface shape around the disk is randomly puckered near the particle's edge and weakly quadrupolar in the far field; an additional interferogram with random puckering near the disk and only higher order modes evident $\sim$ 2.3 radii from the disk in shown in Appendix A. We also show two example trajectories in Appendix A of such disks. A disk on an interface around a 600 μm post ($\lambda^* = 0.25$) exhibits curvature attraction until contact, where on an interface around a 250 μm diameter micropost ($\lambda^* = 0.6$), such a disk moved radially towards the post and stopped at some equilibrium location $L_0(t_f)$=314.7 μm, similar to the results above with the smaller disks. However, when such disks are placed on an interface around a micropost with diameter of 125 μm (λ^* =1.2), the disks are strongly repelled from the high curvature zones, migrating away from the micropost (Fig. 4.3a) at rapid rates that diminish with distance from the post.

The energy dissipated along these repulsive trajectories is shown versus L_0 in Fig. 4.3c; these data, graphed against deviatoric curvature, suggest a linear relationship only far from the post (Appendix A); an inspection of L_0 versus t suggests that these particles act as repulsive quadrupoles in the far field, i.e. that the particles have quadrupolar modes that are misaligned, and hence repelled from the high curvature regions, with $\alpha_2 = \pi/2$. The arrows in these figures indicate that the direction of migration is away from the post.

We have conducted similar experiments with 25 μm disks around microposts of various diameters where λ^* is 0.20, 0.44 and 0.53. We summarize our experimental findings for all of the disks in a histogram in Fig. 4.4 and categorized these behaviors as attraction, equilibria or repulsion as a function of λ^*. The histogram shows systematic changes with λ^*. For $\lambda^* < 0.075$ all particles experience capillary curvature attraction and move without interruption along radial paths to the micropost. For moderate λ^*, particles are either attracted all the way to the micropost or find equilibrium locations at distances of several particle radii from the micropost. For larger $\lambda^* > 0.5$, particles either find equilibrium locations or are repelled from high curvature regions. Finally, for the largest value of λ^* explored, all particles were repelled from the high curvature zones.

We interpret these results within the context of (4.20). The contact line on each disk is determined by randomly distributed rough sites that pin the contact line. Thus, the amplitude of each mode can vary strongly from particle to particle in the same batch. Equation (4.20) indicates that each mode has a preferred orientation to minimize the energy on the interface. For example, for contact lines described by a quadrupolar mode, the energy is minimized when the quadrupolar rise axis aligns with the rise axis of the interface; this has indeed been reported for small cylindrical particles on curved fluid interfaces that excite strong quadrupolar distortions [20]. For contact lines described solely by hexapolar modes or octopolar modes, particles would orient as shown in Fig. 4.5. Particles experience a capillary torque to enforce this alignment; if all α_n could align so that their curvature capillary energy were negative, the particles would migrate toward the post to minimize the capillary energy. This migration would occur at different rates owing to the different amplitudes of the modes h_i and their differing dependencies on L_0. Such trajectories would give the steepest reduction in curvature capillary energy.

However, random pinning implies not only random amplitudes, but also random phase angles of the various modes, so modes cannot co-align. Furthermore, when several modes are present, different modes dominate in different zones of the interface. Far from the micropost, the quadrupolar mode dominates the particle's rotational alignment and migration. As the particle migrates toward the post, λ increases, and higher order modes grow in importance. There are two scenarios in zones where these higher order modes compete. The particle may rotate, adjusting its angle in local equilibrium as it approaches the post. Or, there may be significant energy barriers to rotation owing to the rugged contact line, so particles cannot find an angle that allows particles to migrate toward the post. This latter case is particularly interesting, as it suggest that rough particles on curved interfaces may not rotate freely, but may have pinned orientations. For such pinned angles, the signs on the competing modes will likely differ. Orientations can occur where attractive and repulsive terms can balance, defining states of mechanical equilibrium. However, as λ approaches unity, all terms become important. For particles with trapped "bad" alignments with contributions from many modes, energy can decrease only by moving *away* from the post, i.e. they will be repelled from high curvature sites.

We have observed a complex trajectory that further supports this interpretation. A 25 μm disk attached to an interface around a micropost of diameter 47 μm ($\lambda^* = 0.53$). The particle was initially repelled from the high curvature region, and migrated away from the post (Fig. 4.6). However, at L_0= 309.5 μm ($\lambda = 0.039$) the particle suddenly rotated roughly 86°, and subsequently moved towards the post, obeying a 1/4 power law over the attractive segment of its motion. The disk then increased its speed as it neared the post, but stopped abruptly several particle radii from the post. This evidence suggests that the initial repulsion can be attributed to the trapped poorly aligned quadrupole. The rotation occurred at λ where the higher order modes were negligible; the rotation angle of 86° rotated the misaligned quadrupole into favorable alignment for curvature attraction. Finally, the power law in the subsequent attraction revealed the attractive quadrupolar curvature interaction (Fig. 4.6b).

We can indeed construct simple deformation fields and energy landscapes that capture the main features of these experiments assuming a particle with two pinned modes, a hexapole and quadrupole, with the rise axis of quadrupole aligned with that of the hexapole. If the particle attaches far from the post, the hexapolar mode can be neglected. The particle will rotate, aligning the quadrupolar rise axis with the rise axis of the interface and move to sites of high curvature. As the particle approaches the post, the mis-aligned hexapole introduces an increasingly strong repulsive force. If rotation is impeded, the disk will find an equilibrium location which stops particle migration. If instead, the disk adsorbs to the interface near the micropost, both modes contribute and there will be a strong rotational barrier. Particles with misaligned modes can reduce their energy by moving away from the post (See Appendix A). We are exploring these scenarios using particle engineered to present such distortions in ongoing work.

4.6. Conclusions

We have been developing the relationships between capillary energy landscapes around isolated particles and interface shape to develop new ways to direct particle migration and assembly. Contact line pinning plays an important role in determining such interactions; undulated three-phase contact lines create quadrupolar distortions to leading order. These distortions couple with the deviatoric curvature field of curved fluid interfaces. The resulting curvature capillary energy drives small particles to sites of strong deviatoric curvature. In other studies, we have explored this phenomenon for a variety of microparticle systems, and have extended these arguments to understand microparticle migration on tense lipid bilayer vesicles, on which particles trace Brownian trajectories guided by curvature gradients owing to the weak tension in these systems [21]. Thus, the concepts we develop here can be adapted to apply to different physical systems.

Here, we report that higher order modes in the interface shape and the particle sourced distortion provide greater complexity, with particles finding equilibrium locations far from the sites of highest curvature, or being repelled from high curvature locations. We have demonstrated these concepts using particles with random roughness to pin the contact lines. Pinned contact lines also occur on relatively smooth but chemically heterogeneous particles. Since such particles are ubiquitous, these phenomena are also likely of broad importance.

4.7. Outlook

Interface curvature has already been used to guide structure formation. For example, Ershov *et al.* has exploited the coupling of the particle's quadrupolar distortion with the principal axes of curvature to form colloidal crystalline domains with quadrupolar symmetry from colloidal spheres [86]. Cavallaro *et al.* has exploited this coupling and capillary curvature attraction to build complex structures around a square micropost [20]. The building of such structures is a focus of ongoing work in our research group. Particles with differing shapes give important degrees of freedom; cylindrical particles show competition between pair quadrupolar interactions and curvature interactions in their assembly [70].

Curvature repulsion, discussed here, opens exciting new possibilities. To explore these phenomena, we have expanded the host interface locally to higher order modes in a multipole expansion. The particular expansion that we find is valid for our particular interface shape. However, such expansions can always be performed for interfaces with small slopes. Thus, this work suggests that interface shapes can be molded and tailored to emphasize particular modes in particular spatial regions. These interactions also have rich coupling with particle shape. For example, consider a high aspect ratio microcylinder on a curved interface formed around a very small micropost in Fig. 4.7. For reference, prior studies with small cylindrical microparticles around large posts report particles aligned with their major axes along principal axes. Here, the long microcylinder migrates radially along curvature gradients with its major axis pointed toward the micropost, and stops at an equilibrium location far from the post with an orientation that positions its sharp edge toward the post, indicating the importance of details in the interface shape around the particle. This, too, is a focus of ongoing work.

This research opens interesting new directions. In materials science, we might design curvature capillary energy wells to mold objects based on their symmetries far from the curvature source, thereby preventing trapped states that can occur for objects in contact with the posts. In microrobotics, curvature attraction and curvature repulsion could provide new means of propelling microrobots along interfaces [118]. It would be interesting to investigate limiting length scales; can we mold structure formation at the submicron scale? Finally, we close by noting that this study falls within a rich and interesting class of problems in which a colloid is placed in soft matter, distorts the soft matter host, and creates an energy landscape around it. By molding the host-in this communication, the fluid interface, rich phenomena emerge. We and others have explored related phenomena for colloids and macromolecules confined in other hosts including colloids in nematic liquid crystals, colloids adhered to lipid bilayer vesicles, and proteins on curved lipid bilayers [21, 23, 119, 120, 121, 122]

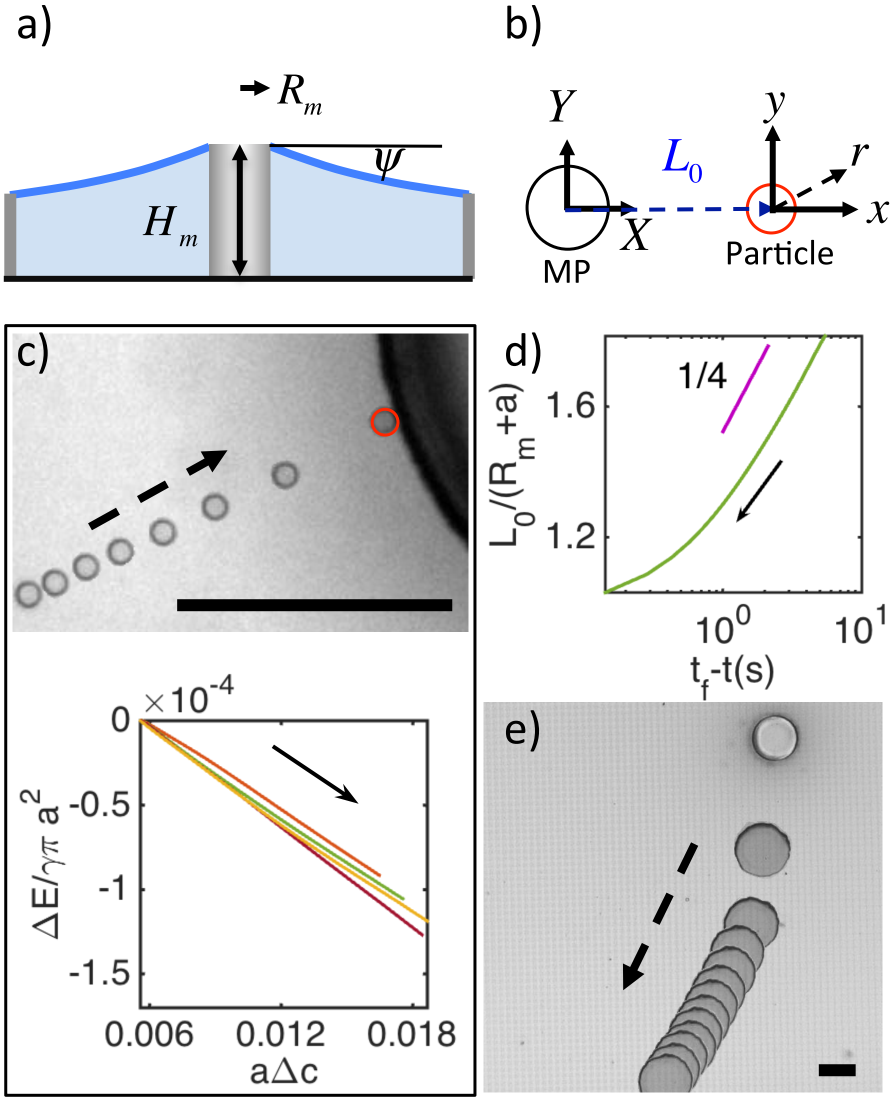

Figure 4.1: Curvature attraction and curvature repulsion. Arrows indicate direction of migration. (a) Schematic of the interface shape formed by pinning fluid interface to the edge of a micropost and an outer ring. (b) Coordinates at center of micropost and at the particle located a distance L_0 from the post center. (c) (Top) A microdisk ($2a$=10 μm) migrates to the edge of a micropost (250 μm diameter). (Bottom) The energy dissipated as such particles migrate to the high curvature regions is linear in deviatoric curvature. (d) The power law dependence confirms the dominance of the quadrupolar mode. (e) A disk ($2a$=150 μm) migrates away from the micropost (125 μm diameter).

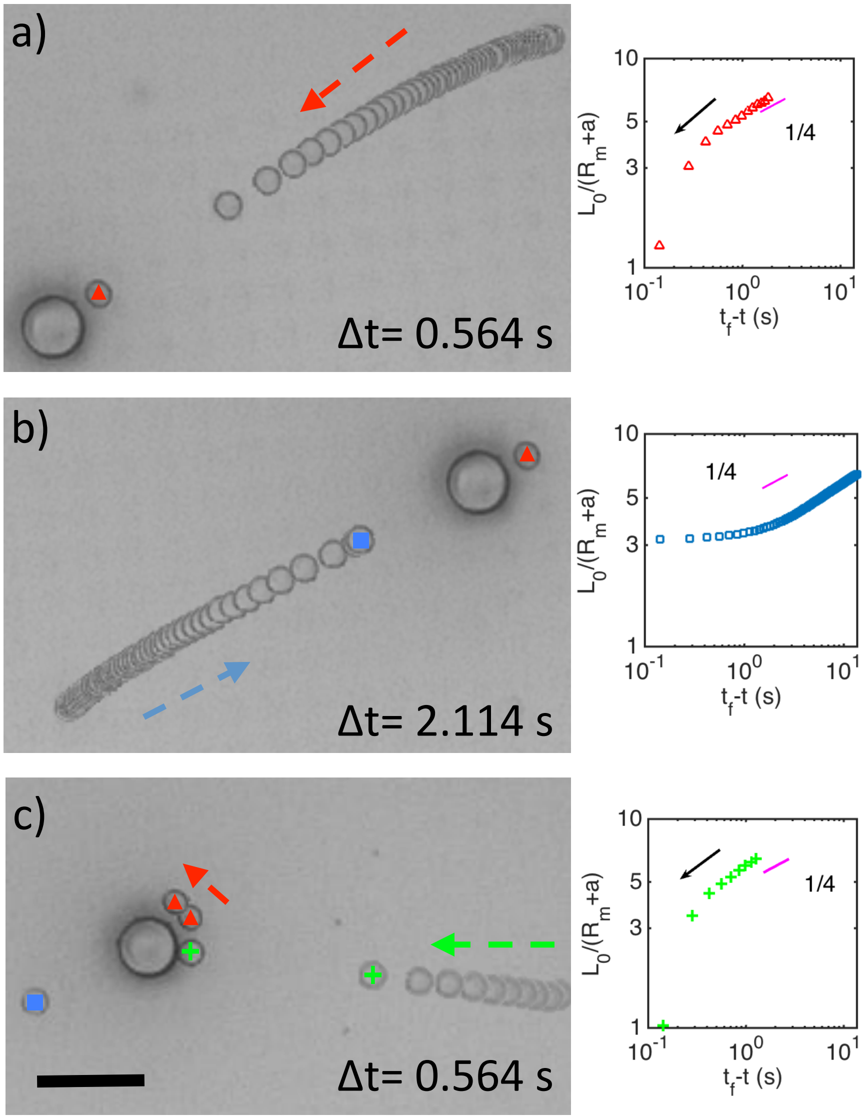

Figure 4.2: Bocce Ball: Trajectories of microdisks ($2a$=25 μm) around a circular micropost. Left panel: Time stamped image of microdisks trajectory on a curved oil-water interface where the micropost is 57 μm in diameter. Right panel: log-log graph of $L_0/(R_m + a)$ vs $t_f - t$ for each trajectory. (a) A microdisk (red triangle) migrates along curvature gradients toward the micropost and stops before contacting the post (at 50.9 μm center-to-center distance). (b) A microdisk (blue square) migrate towards the micropost and stops at 128.0 μm, several particle radii from the post. (c) A microdisk (green cross) migrates towards the edge of the micropost. This incoming disk interacts strongly with the first disk, causing it to move at a constant distance from the post to a new location, as such, its final position is shifted slightly. Scale bar is 100 μm.

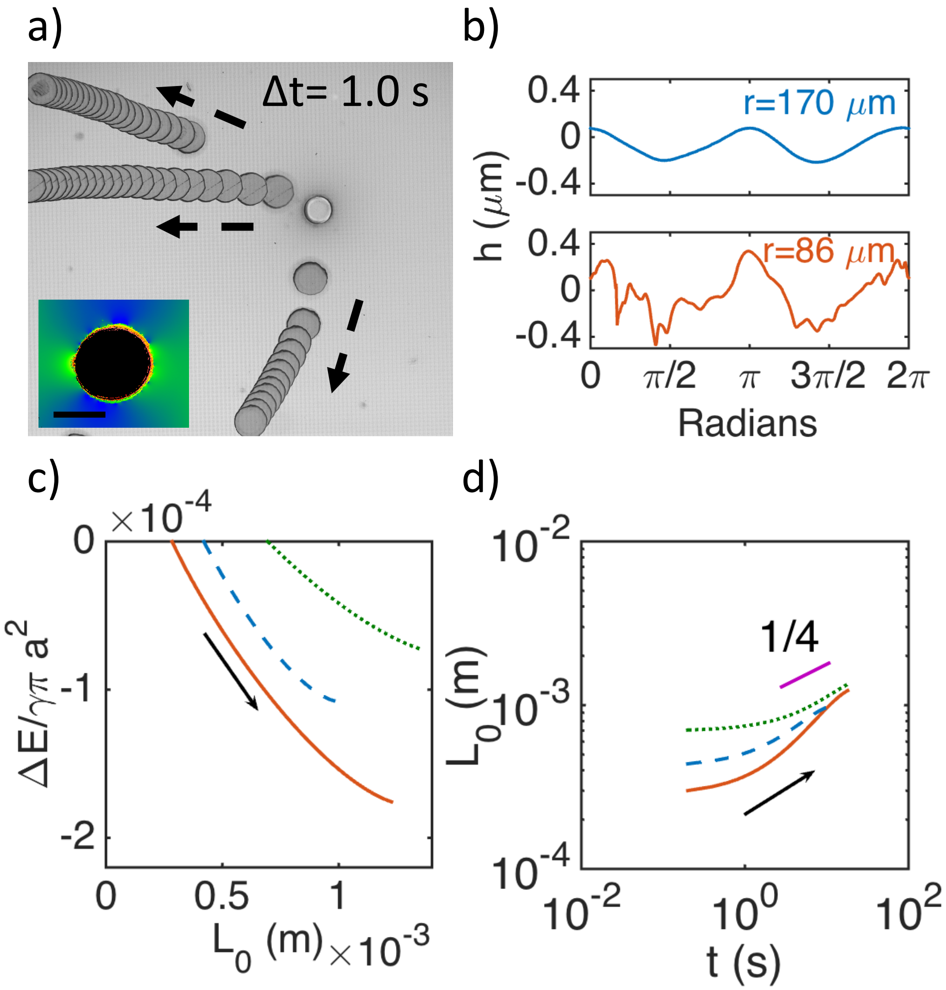

Figure 4.3: Curvature repulsion of microdisks ($2a$=150 μm) around circular microposts. Time stamped image of microdisks trajectories on curved oil-water interfaces. (a) Three microdisks are repelled by the curved oil-water interface and migrate radially outwards from the 125 μm diameter micropost. Inset: interferogram showing quadrupolar distortion far from the particle and puckered interface near the particle. Scale bar is 100 μm. (b) Top: quadrupolar undulation of interface height along a circle of radius 170 μm from particle center. Bottom: rugged interface height along a circle of radius 86 μm from particle center. (c) Energy dissipated along a trajectory. (d) L_0 vs. t: evidence of repulsive quadrupole in the far field.

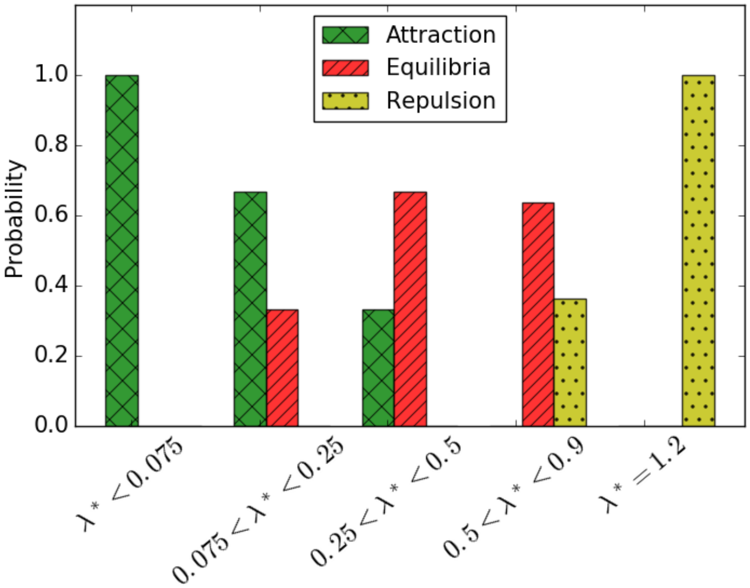

Figure 4.4: Transition from curvature attraction to repulsion with λ^*. A histogram summarizing all of the particle trajectories as a function of λ^*, the ratio of particle radius to micropost radius. Green (attraction to the post), red (equilibrium away from the post), and yellow (repulsion from the post throughout the field of view). The length of the bars indicate the probabilities of the observed particles trajectories within the λ^* range.

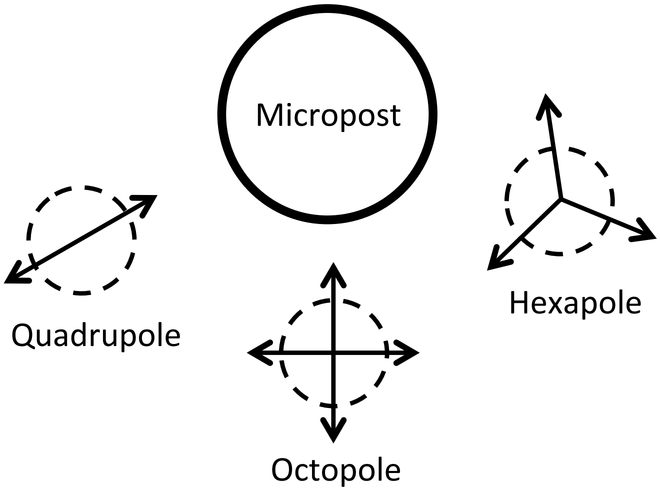

Figure 4.5: Preferred orientation of quadrupole, hexapole and octopole deformation around a micropost. Headed arrows indicate the axes of capillary rises on the particle. Quadrupole and octopus prefer their rise axes pointed toward the micropost, while hexapole prefers to point the valley between the two rise axes toward the micropost.

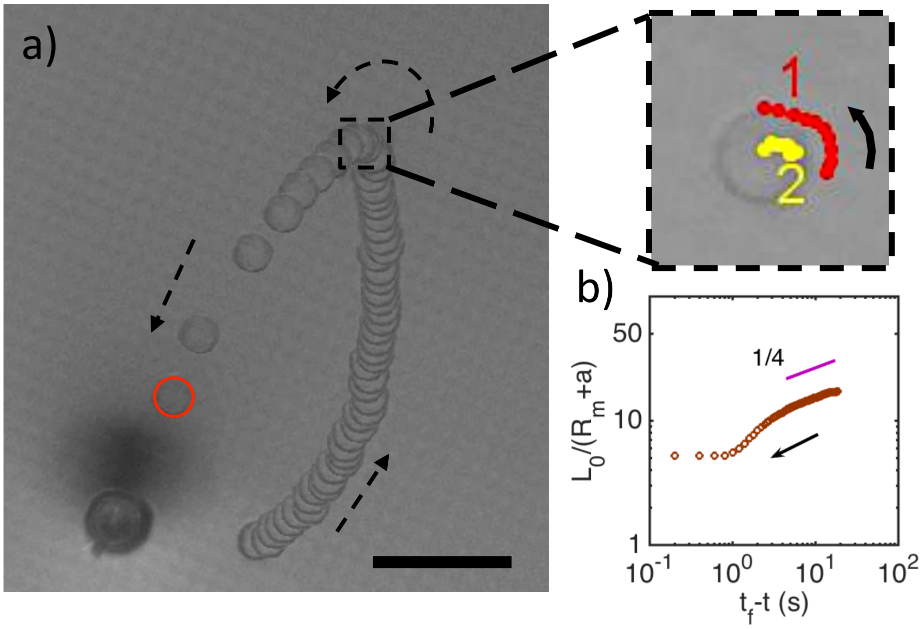

Figure 4.6: Repulsion followed by rotation and attraction. (a) Time stamped image (Δt=2 s) of a microdisk ($2a$=25 μm) on a curved interface created by a 47 μm micropost. The microdisk is initially repelled by the curvature and migrates away from the micropost. The particle then rotates roughly 86°. Thereafter, it is attracted towards the micropost. Red circle indicates the final location of the disk. Inset: Particle rotation as marked by red dots (1) the mark on the particle, and yellow dots (2) indicate the center of the disk. (b) $L_0/(R_m + a)$ vs $t_f - t$ for the latter part of trajectory, as disk approached the post.

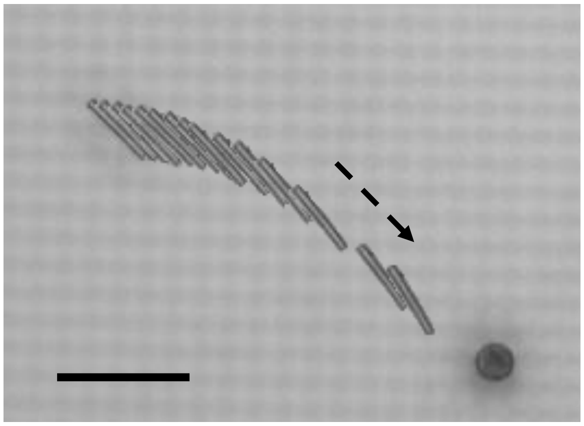

Figure 4.7: Particle shape: A long microcylinder finds an equilibrium location with complex orientation. Time stamped image ($\Delta t = 1.0s$) of a microcylinder migration on a curved oil-water interface formed around a 28 μm micropost. Scale bar is 100 μm.

CHAPTER 5 : Pair interactions on curved interfaces

5.1. Introduction

In this chapter, we explore particle interactions on a curved fluid interface with zero mean curvature. On planar interfaces, particles interact with deformation fields from their neighbors to assemble. On curved interfaces, curvature capillary interactions can either attract or repel particles from high curvature regions. Here, I derive an expression for the energy of interaction for a pair of particles on curved fluid interfaces.

In our experiments using spheres on curved fluid interfaces, we have observed microspheres on curved fluid interfaces assemble into chains, zig-zag, and L-shaped assemblies. These observations inspired me to study physics behind the experimental observations. Assuming the two microparticles attach to an interface with zero mean curvature, analytical solution is derived for the pair interaction. The final form of the interaction energy will be useful in understanding how particles assemble on curved interface, and in the development of strategies to design structures guided by the curvature field.

This work was performed in collaboration with Dr. Sharifi-Mood and Alismari Read. I derived the analytical solution for the pair interaction, and later compared it to my collaborator's derivation in bipolar coordinate.

5.2. Theory

5.2.1. Interface profile around particle A

Suppose two microspheres, A and B, are trapped on a curved fluid interface, and the contact line is pinned at the surface of each particle. The particles are separated by some distance r_{AB}. Each particle deforms the curved interface around them with a quadrupolar distortion, h_{p_A} and h_{p_B}. Letting the coordinate to be centered at particle A, the interface shape around particle A can be summed as the contribution from (i) the quadrupolar distortion owing to

A's undulated contact line h_A, (ii) the parent interface h_0, (iii) the induced term from the parent interface $h_{ind(0)}$, (iv) the local distortion near A from the neighboring particle B, $h_{B\,at\,A}$, and (v) the induced term due to particle B, $h_{ind\,(B\,at\,A)}$,

$$h = h_0 + h_{B\,at\,A} + h_A + h_{ind(0)} + h_{ind\,(B\,at\,A)}. \tag{5.1}$$

Each term can be written explicitly as

$$h_0 = \frac{\Delta c_0^A {r_A}^2}{4} \cos(2(\phi_A - \beta_A)) \tag{5.2}$$

$$h_{B\,at\,A} = \frac{3h_{p_B} a^2 r_A^2}{{r_{AB}}^4} \cos(2(\phi_A + \alpha_B)) \tag{5.3}$$

$$h_A = \frac{h_{p_A} a^2}{{r_A}^2} \cos(2(\phi_A - \alpha_A)) \tag{5.4}$$

$$h_{ind(0)} = -\frac{\Delta c_0^A}{4} \frac{a^4}{{r_A}^2} \cos(2(\phi_A - \beta_A)) \tag{5.5}$$

$$h_{ind\,(B\,at\,A)} = -\frac{3h_{p_B} a^4}{{r_{AB}}^4} \frac{a^2}{r_A^2} \cos(2(\phi_A + \alpha_B)) \tag{5.6}$$

where r_i is the radial distance from the center of particle i, α_i is the phase angle of particle i with respect to the center-to-center axis of the neighboring particle, β_i is the phase angle of particle i with respect to the host curvature field, and Δc_0^i is the deviatoric curvature at i. The subscript i takes A or B for particle A and B respectively (Fig. 5.1).

The full expression of the height profile around particle A is

$$\begin{aligned} h =& \frac{\Delta c_0^A {r_A}^2}{4} \cos(2(\phi_A - \beta_A)) + \frac{3h_{p_B} a^2 r_A^2}{{r_{AB}}^4} \cos(2(\phi_A + \alpha_B)) + \frac{h_{p_A} a^2}{{r_A}^2} \cos(2(\phi_A - \alpha_A)) \\ & - \frac{\Delta c_0^A}{4} \frac{a^4}{{r_A}^2} \cos(2(\phi_A - \beta_A)) - \frac{3h_{p_B} a^4}{{r_{AB}}^4} \frac{a^2}{r_A^2} \cos(2(\phi_A + \alpha_B)) \end{aligned} \tag{5.7}$$

Define variables A, B, C, D, and E:

$$A = \frac{\Delta c_0^A}{4} \tag{5.8a}$$

$$B = \frac{3h_{p_B} a^2}{{r_{AB}}^4} \tag{5.8b}$$

$$C = h_{p_A} a^2 \tag{5.8c}$$

$$D = \frac{\Delta c_0^A a^4}{4} \tag{5.8d}$$

$$E = \frac{3h_{p_B} a^6}{{r_{AB}}^4} \tag{5.8e}$$

First derivative with respect to r_A

$$\frac{\partial h_0}{\partial r} = 2Ar_A \cos(2(\phi_A - \beta_A)) \tag{5.9}$$

$$\frac{\partial h_{B\,at\,A}}{\partial r_A} = 2Br_A \cos(2(\phi_A + \alpha_B)) \tag{5.10}$$

$$\frac{\partial h_A}{\partial r_A} = -\frac{2C}{r_A^3} \cos(2(\phi_A - \alpha_A)) \tag{5.11}$$

$$\frac{\partial h_{ind(0)}}{\partial r_A} = \frac{2D}{r_A^3} \cos(2(\phi_A - \beta_A)) \tag{5.12}$$

$$\frac{\partial h_{ind(B\,at\,A)}}{\partial r_A} = \frac{2E}{r_A^3} \cos(2(\phi_A + \alpha_B)) \tag{5.13}$$

The interface profile around particle A can be written as a summation of host fields with disturbance. Host fields, h_{host} in this context are the inherent curvature field and the distortion field from the neighboring particle, h_0 and $h_{B\,at\,A}$, respectively. The disturbance on the interface contains three parts: the particle imposed distortion, the induced disturbance due to the deviatoric curvature of the host interface, and the induced disturbance that fights the distortion due to the neighboring particle B. Therefore, we can re-write h as,

$$h = h_{host} + \eta \tag{5.14}$$

where

$$\begin{aligned} h_{host} &= h_0 + h_{B\,at\,A} \\ &= \frac{\Delta c_0^A {r_A}^2}{4}\cos(2(\phi_A - \beta_A)) + \frac{3h_{p_B} a^2 r_A^2}{{r_{AB}}^4}\cos(2(\phi_A - \alpha_B)) \\ &= A r_A^2 \cos(2(\phi_A - \beta_A)) + B r_A^2 \cos(2(\phi_A - \alpha_B)) \end{aligned} \tag{5.15}$$

$$\begin{aligned} \eta &= h_A + h_{ind(0)} + h_{ind\,(B\,at\,A)} \\ &= \frac{h_{p_A} a^2}{{r_A}^2}\cos(2(\phi_A - \alpha_A)) - \frac{\Delta c_0^A}{4}\frac{a^4}{{r_A}^2}\cos(2(\phi_A - \beta_A)) - \frac{3h_{p_B} a^4}{{r_{AB}}^4}\frac{a^2}{r_A^2}\cos(2(\phi_A + \alpha_B)) \\ &= \frac{C}{r_A^2}\cos(2(\phi_A - \alpha_A)) - \frac{D}{r_A^2}\cos(2(\phi_A - \beta_A)) - \frac{E}{r_A^2}\cos(2(\phi_A + \alpha_B)) \end{aligned} \tag{5.16}$$

5.2.2. Finding interaction energy

To find pair interaction energy we first have to calculate the excess surface area. In Monge representation, the area integral is:

$$A = \int \sqrt{1 + \nabla h \cdot \nabla h} dS \tag{5.17}$$

where dS is the area of the interface. Assuming small slopes, $\nabla h << 1$, the integrand can be approximated by Taylor series,

$$\sqrt{1 + \nabla h \cdot \nabla h} = 1 + \frac{\nabla h \cdot \nabla h}{2}. \tag{5.18}$$

Now, we can find the interaction energy between the two particles with a center-to-center separation r_{AB}. For simplicity, we ignore the contribution from the mean curvature, so the energy prior to particle attachment is

$$E_1 = \gamma \oiint_D 1 + \frac{\nabla h_{host} \cdot \nabla h_{host}}{2} dA \tag{5.19}$$

where γ is the interfacial tension, h_0 is the height of the host interface, and D denotes the entire interfacial domain. When the particle attaches to the interface, the free energy becomes

$$E_2 = \gamma_1 A_1 + \gamma_2 A_2 + \gamma \oiint\limits_{D-P} 1 + \frac{\nabla h \cdot \nabla h}{2} dA \tag{5.20}$$

where h is the height of interface after the particle is adsorbed, $\gamma_1 A_1$ and $\gamma_2 A_2$ are the surface energies for the particle wetted with the upper and lower fluids, respectively, and $D - P$ is the domain of the interface outside of the particle. Therefore, the energy is

$$E_2 - E_1 = \gamma_1 A_1 + \gamma_2 A_2 + \gamma \oiint\limits_{D-P} 1 + \frac{\nabla h \cdot \nabla h}{2} dA - \gamma \oiint\limits_{D} 1 + \frac{\nabla h_{host} \cdot \nabla h_{host}}{2} dA \tag{5.21}$$

Substituting Equation 5.15, 5.16, into Equation 5.20,

$$\begin{aligned} E_2 &= \gamma_1 A_1 + \gamma_2 A_2 + \gamma \oiint\limits_{D-P} 1 + \frac{\nabla(h_0 + h_{B\,at\,A} + \eta) \cdot \nabla(h_0 + h_{B\,at\,A} + \eta)}{2} dA \\ &= \gamma_1 A_1 + \gamma_2 A_2 + \gamma \oiint\limits_{D-P} \left\{ 1 + \frac{\nabla h_0 \cdot \nabla h_0}{2} + \frac{\nabla h_{B\,at\,A} \cdot \nabla h_{B\,at\,A}}{2} + \frac{\nabla \eta \cdot \nabla \eta}{2} \right. \\ &\quad \left. + \nabla h_0 \cdot \nabla h_{B\,at\,A} + \nabla h_0 \cdot \nabla \eta + \nabla h_{B\,at\,A} \cdot \nabla \eta \right\} dA \end{aligned} \tag{5.22}$$

So, Equation 5.21 becomes,

$$\begin{aligned} E_2 - E_1 &= \gamma_1 A_1 + \gamma_2 A_2 + \gamma \oiint\limits_{D-P} \left\{ 1 + \frac{\nabla h_0 \cdot \nabla h_0}{2} + \frac{\nabla h_{B\,at\,A} \cdot \nabla h_{B\,at\,A}}{2} + \frac{\nabla \eta \cdot \nabla \eta}{2} \right. \\ &\quad \left. + \nabla h_0 \cdot \nabla h_{B\,at\,A} + \nabla h_0 \cdot \nabla \eta + \nabla h_{B\,at\,A} \cdot \nabla \eta \right\} dA - \gamma \oiint\limits_{D} 1 + \frac{\nabla h_{host} \cdot \nabla h_{host}}{2} dA \\ &= \gamma_1 A_1 + \gamma_2 A_2 + \gamma \oiint\limits_{D-P} \left\{ \frac{\nabla \eta \cdot \nabla \eta}{2} + \nabla h_0 \cdot \nabla \eta + \nabla h_{B\,at\,A} \cdot \nabla \eta \right\} dA \\ &\quad - \gamma \oiint\limits_{P} 1 + \frac{\nabla h_{host} \cdot \nabla h_{host}}{2} dA \end{aligned} \tag{5.23}$$

The first integral is the energy owing to the disturbance, and the second integral is the area of the hole in the interface created by the particle adsorption. Let's first consider the first integrand. Gradient operator of the disturbance can then be written as the sum of the gradients,

$$\frac{\nabla\eta\cdot\nabla\eta}{2}=\frac{1}{2}\nabla(h_A+h_{ind(0)}+h_{ind\,(B\,at\,A)})\cdot\nabla(h_A+h_{ind(0)}+h_{ind\,(B\,at\,A)})$$

$$\begin{aligned}&=\frac{\nabla h_A\cdot\nabla h_A}{2}+\frac{\nabla h_{ind(0)}\cdot\nabla h_{ind(0)}}{2}+\frac{\nabla h_{ind(B\,at\,A)}\cdot\nabla h_{ind(B\,at\,A)}}{2}\\&\quad+\nabla h_A\cdot\nabla h_{ind(0)}+\nabla h_A\cdot h_{ind(B\,at\,A)}+\nabla h_{ind(0)}\cdot h_{ind(B\,at\,A)}\end{aligned}\tag{5.24}$$

To solve the integral in the above equation, we utilize the Green's theorem. The integrand can then be written as

$$\nabla h_A\cdot\nabla h_A=\nabla\cdot(h_A\nabla h_A)-(h_A\nabla^2h_A)\tag{5.25}$$

where the second term is zero since $\nabla^2 h_A$=0. Therefore, the area integral is

$$\frac{1}{2}\oiint_{D-P}\nabla h_A\cdot\nabla h_A dA=\frac{1}{2}\oiint_{D-P}\nabla\cdot(h_A\nabla h_A)dA\tag{5.26}$$

By applying Green's theorem as contour integral,

$$\begin{aligned}\frac{1}{2}\oiint_{D-P}\nabla\cdot(h_A\nabla h_A)dA&=\frac{1}{2}\oint_{I}(h_A\nabla h_A)\cdot\mathbf{m}ds\\&=\lim_{r^*\to\infty}\frac{1}{2}\oint_{r_A=r^*}e_r\cdot(h_A\nabla h_A)\,r_Ad\phi-\frac{1}{2}\oint_{r_A=a}e_r\cdot(h_A\nabla h_A)\,r_Ad\phi\\&=\frac{1}{2}\int_{\phi=0}^{2\pi}h_A\left(\frac{\partial h_A}{\partial r}\right)r_Ad\phi\Bigg|_{r_A=\infty}-\frac{1}{2}\int_{\phi=0}^{2\pi}h_A\left(\frac{\partial h_A}{\partial r}\right)r_Ad\phi\Bigg|_{r_A=a}\end{aligned}\tag{5.27}$$

Useful integrals for integrating cos functions from 0 to 2π:

$$\int_{0}^{2\pi} \cos^2(2(x-a))dx = \pi \tag{5.28}$$

$$\int_{0}^{2\pi} \cos(2(x-a))\cos(2(x-b))dx = \pi\cos(2(a-b)) \tag{5.29}$$

The individual terms are calculated as follows,

$$\begin{aligned}\frac{1}{2}\int_{\phi=0}^{2\pi} h_A\left(\frac{\partial h_A}{\partial r}\right)r_A d\phi\Bigg|_{r_A=\infty} &= \frac{1}{2}\int_{\phi=0}^{2\pi} \frac{C}{r_A^2}\cos(2(\phi_A-\alpha_A))\left(-\frac{2C}{r_A^3}\cos(2(\phi_A-\alpha_A))\right)r_A d\phi \\ &= \pi\frac{C^2}{r_A^4} = \pi\frac{(h_{p_A}a^2)^2}{r_A^4}\Bigg|_{r_A=\infty} = 0\end{aligned} \tag{5.30}$$

$$-\frac{1}{2}\int_{\phi=0}^{2\pi} h_A\left(\frac{\partial h_A}{\partial r}\right)r_A d\phi\Bigg|_{r_A=a} = \pi\frac{(h_{p_A}a^2)^2}{r_A^4}\Bigg|_{r_A=a} = -\pi\frac{(h_{p_A}a^2)^2}{a^4} \tag{5.31}$$

Subtracting two terms gives,

$$\gamma\oiint_{D-P}\frac{\nabla h_A\cdot\nabla h_A}{2}dA = \gamma\pi {h_{P_A}}^2 \tag{5.32}$$

Applying the same method, we solve the rest of the terms in $\nabla\eta \cdot \nabla\eta$,

$$\gamma \oiint\limits_{D-P} \frac{\nabla h_{ind(0)} \cdot \nabla h_{ind(0)}}{2} dA = -\gamma \frac{D^2}{r_A^4}\pi \bigg|_a^\infty = \gamma \frac{\Delta c_0^2 a^4}{16}\pi \tag{5.33}$$

$$\gamma \oiint\limits_{D-P} \frac{\nabla h_{ind(B\,at\,A)} \cdot \nabla h_{ind(B\,at\,A)}}{2} dA = -\gamma \frac{E^2}{r_A^4}\pi \bigg|_a^\infty = \gamma \frac{9 {h_{p_B}}^2 a^8}{{r_{AB}}^8}\pi \tag{5.34}$$

$$\gamma \oiint\limits_{D-P} \nabla h_A \cdot \nabla h_{ind(0)} dA = \frac{2CD}{r_A^4}\cos(2(\beta_A - \alpha_A))\bigg|_a^\infty = -\gamma \frac{h_{p_A} a^2 \Delta c_0^A}{2}\pi \cos(2(\beta_A - \alpha_A)) \tag{5.35}$$

$$\begin{aligned}\gamma \oiint\limits_{D-P} \nabla h_A \cdot \nabla h_{ind(B\,at\,A)} dA &= \gamma\ \frac{2CE}{{r_A}^4}\cos(2(\alpha_A + \alpha_B))\bigg|_a^\infty \\ &= -\gamma \frac{6 h_{p_A} h_{p_B} a^4}{r_{AB}^4}\pi \cos(2(\alpha_A + \alpha_B))\end{aligned} \tag{5.36}$$

$$\begin{aligned}\gamma \oiint\limits_{D-P} \nabla h_{ind(0)} \cdot \nabla h_{ind(B\,at\,A)} dA &= \gamma\ \frac{2DE}{{r_A}^4}\pi \cos(2(\beta_A + \alpha_B))\bigg|_a^\infty \\ &= \gamma \frac{3 h_{p_B} a^6 \Delta c_0^A}{2 r_{AB}^4}\pi \cos(2(\beta_A + \alpha_B))\end{aligned} \tag{5.37}$$

The remaining terms in the first integral are

$$\gamma \oiint\limits_{D-P} \nabla h_0 \cdot \nabla\eta dA = 0 \tag{5.38}$$

$$\gamma \oiint\limits_{D-P} \nabla h_{B\,at\,A} \cdot \nabla\eta dA = 0 \tag{5.39}$$

The second integral is

$$-\gamma \oiint\limits_P 1 + \frac{\nabla h_{host} \cdot \nabla h_{host}}{2} dA = -\, \gamma \pi a^2 - \gamma \oiint\limits_P \frac{\nabla h_0 \cdot \nabla h_0}{2} + \frac{\nabla h_{B\,at\,A} \cdot \nabla h_{B\,at\,A}}{2} + \nabla h_0 \cdot \nabla h_{B\,at\,A}\ dA \tag{5.40}$$

Individual integrals are calculated as

$$-\gamma \oiint\limits_P \frac{\nabla h_0 \cdot \nabla h_0}{2}\ dA = \gamma\ A^2 {r_A}^2\big|_0^a = -\gamma \frac{\Delta {c_0^A}^2 a^4}{16}\pi \tag{5.41}$$

$$-\gamma \oiint\limits_P \frac{\nabla h_{B\,at\,A} \cdot \nabla h_{B\,at\,A}}{2}\ dA = -\gamma\ B^2 {r_A}^4 \pi\big|_0^a = -\gamma \frac{9 h_{p_B}^2 a^8}{{r_{AB}}^8}\pi \tag{5.42}$$

$$\begin{aligned} -\gamma \oiint\limits_P \nabla h_0 \cdot \nabla h_{B\,at\,A}\ dA &= -\gamma\ 2AB{r_A}^2 \pi \cos(2(\beta_A + \alpha_B))\big|_0^a \\ &= -\gamma \frac{3 h_{p_B} a^6 \Delta c_0^A}{2 r_{AB}^4}\pi \cos(2(\beta_A + \alpha_B)) \end{aligned} \tag{5.43}$$

The interaction energy, Equation 5.21, of particle A with respect to the deformation made by neighboring particle B is

$$\begin{aligned} E_2 - E_1 = \gamma_1 A_1 + \gamma_2 A_2 + \gamma \pi {h_{P_A}}^2 + \gamma \frac{\Delta c_0^2 a^4}{16}\pi + \gamma \frac{9 {h_{p_B}}^2 a^8}{{r_{AB}}^8}\pi - \gamma \frac{h_{p_A} a^2 \Delta c_0^A}{2}\pi \cos(2(\beta_A - \alpha_A)) \\ - \gamma \frac{6 h_{p_A} h_{p_B} a^4}{r_{AB}^4}\pi \cos(2(\alpha_A + \alpha_B)) + \gamma \frac{3 h_{p_B} a^6 \Delta c_0^A}{2 r_{AB}^4}\pi \cos(2(\beta_A + \alpha_B)) \\ - \gamma \pi a^2 - \gamma \frac{\Delta {c_0^A}^2 a^4}{16}\pi - \gamma \frac{9 h_{p_B}^2 a^8}{{r_{AB}}^8}\pi - \gamma \frac{3 h_{p_B} a^6 \Delta c_0^A}{2 r_{AB}^4}\pi \cos(2(\beta_A + \alpha_B)) \end{aligned}$$

$$\begin{aligned} E_2 - E_1 = \gamma_1 A_1 + \gamma_2 A_2 + \gamma\pi {h_{P_A}}^2 - \gamma\pi a^2 - \gamma\frac{h_{p_A} a^2 \Delta c_0^A}{2}\pi\cos(2(\beta_A - \alpha_A)) \\ - \gamma\frac{6 h_{p_A} h_{p_B} a^4}{r_{AB}^4}\pi\cos(2(\alpha_A + \alpha_B)) \end{aligned} \tag{5.44}$$

Similar expressions were discussed in the previous chapters for particles with pinned contact lines. The first four terms in the above equation are independent of the curvature and the location of the particles. We then define

$$E_0^A = \gamma_1 A_1 + \gamma_2 A_2 + \gamma\pi {h_{P_A}}^2 - \gamma\pi a^2 \tag{5.45}$$

Therefore,

$$\begin{aligned} E &= E_2 - E_1 \\ &= E_0^A - \gamma\frac{h_{p_A} a^2 \Delta c_0^A}{2}\pi\cos(2(\beta_A - \alpha_A)) - \gamma\frac{6 h_{p_A} h_{p_B} a^4}{r_{AB}^4}\pi\cos(2(\alpha_A + \alpha_B)) \end{aligned} \tag{5.46}$$

To capture the pair interaction, we repeat the same calculation for particle B in the curvature field of particle A. Adding that result to the above expression, the final form of the interaction energy is

$$\begin{aligned} E_{pair} = & E_0^A + E_0^B - \gamma\frac{h_{p_A} a^2 \Delta c_0^A}{2}\pi\cos(2(\beta_A - \alpha_A)) - \gamma\frac{12 h_{p_A} h_{p_B} a^4}{r_{AB}^4}\pi\cos(2(\alpha_A + \alpha_B)) \\ & - \gamma\frac{h_{p_B} a^2 \Delta c_0^B}{2}\pi\cos(2(\beta_B - \alpha_B)) \end{aligned} \tag{5.47}$$

The final form of the interaction energy of a pair of particles A and B has contribution from the individual particle curvature interaction, as well as pair interaction from the two particles.

5.3. Conclusion

In this chapter I have derived the interaction energy of a pair of microparticles on curved fluid interfaces for zero mean curvature interfaces like those we study in our experiments. This final form of energy has two contributions that depend on particle-particle separation distance, and also the local curvature. This competition between the two contributions will determine the particle alignment on the interface. When the pair interaction is stronger than curvature interaction, particles will align with each other in a mirror symmetric orientation. On the other hand, when the curvature interaction is stronger, particles will align their quadrupolar axes along the principal axes, with the quadrupolar rise axis aligned with the rise of the interface. With this result, we could predict particle behavior on the curved interface and use curvature/pair interactions to dictate the assembly on fluid interfaces.

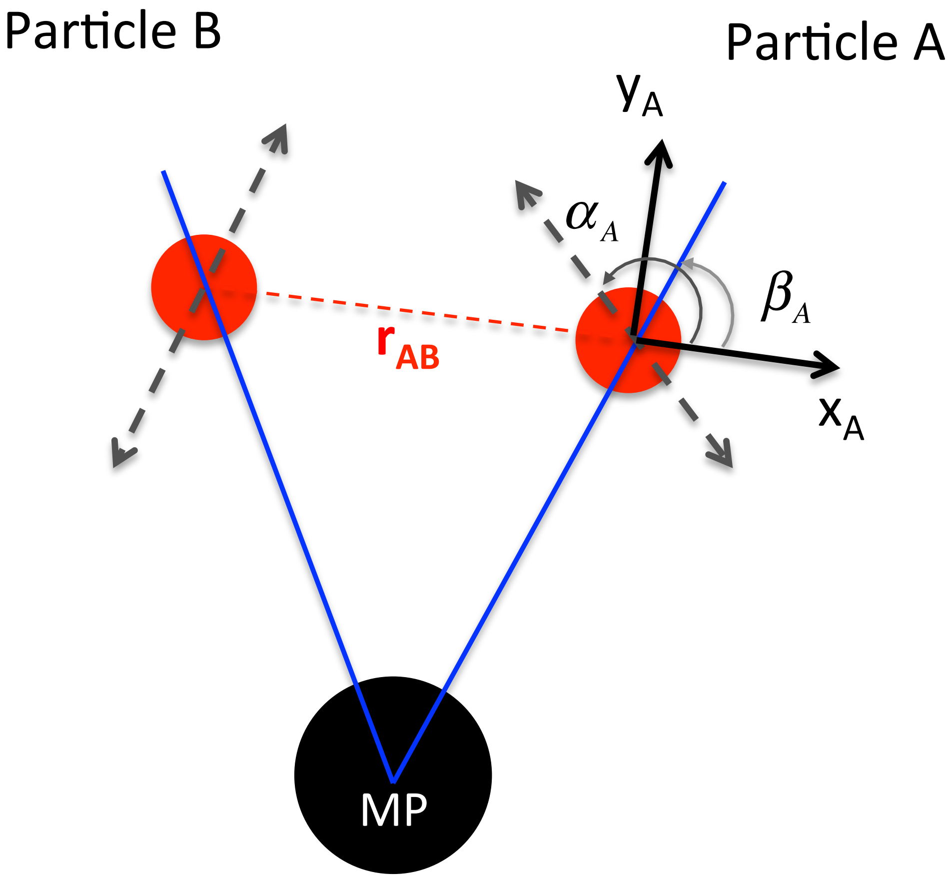

Figure 5.1: Schematic of two particles, A and B, around a micropost. The dark circle represents micropost. Two particles are separated by distance r_{AB}. α_A and α_B denote the phase angle of capillary rise axes for the two particles. β_A and β_B denote the phase angle of the interface rise axes for the two particles.

CHAPTER 6 : Cylindrical particles at nematic films

6.1. Introduction

Colloidal assembly is widely exploited in bottom-up schemes to create organized, micro- and macroscopic structures from nano- and microscale building blocks; particles assembly is guided, e.g., by interparticle potentials and entropic effects, often augmented by external applied fields [1, 123]. Rather than using the usual applied electromagnetic fields, recent research explores interactions that emerge when particles are placed in soft material, for example, elastic interactions that occur when particles are immersed in liquid crystals (LCs) [124, 125, 126].

In this chapter, we study the behavior of cyBlancLCRlindrical particles on thin air-nematic interface, both planar and curved. Cylindrical particles have aspect ratio of 2.5 and are fabricated using standard lithographic technique. Particle behavior on the thin film depends both on the forces from the interface and as well as the bulk. The interplay of capillarity and elasticity determines their interaction and alignment on the planar and the curved interfaces. We report regions of dominance for the curved interfaces.

This work was performed in collaboration with Dr. Gharbi and Victor L. Ngo, an undergraduate researcher who worked in our lab. I designed and performed the experiments, worked on the derivation of capillary and elastic torques, and involved in all the discussions. This study was published in the Proceedings of the National Academy of Sciences of the United States of America.

6.2. Liquid Crystals

Liquid crystal (LC) is a state of matter between liquids and crystals. Molecules in crystals are ordered whereas molecules in liquids they are not. For liquid crystals, they have molecules of a liquid but still maintain some degree of orientational or positional order, and have properties associated with both liquids and crystals. Liquid crystals are made up of anisotropic molecules, including disc-like and rod-like molecules. Such anisotropy gives rise to many unique properties of LC, such as elastic constant, viscosity coefficients, birefringence, dielectric, and diamagnetic anisotropies. One well known example is the liquid crystal display (LCDs) which was developed in 1970s. The discoveries of electro-optical effects in LC revolutionized the display industry in making light weight and flat screens with high quality images.

There are two types of liquid crystals: thermotropic and lyotropic liquid crystals. Thermotropic liquid crystals form liquid crystalline phases under certain temperature ranges. In this case, phase transitions occur as the surrounding temperature is varied. On the other hand, lyotropic liquid crystals form liquid crystals phases only if it is dissolved in water or other solvents. Phases of liquid crystals depend strongly on the concentration of the substances or compounds. Examples of lyotropic liquid crystals include soaps and phospholipids which have a polar head group attached to a long hydrocarbon tail group. LC molecules dissolved in a polar solvent may form micelles and vesicles, or bilayer structure resembling the biological membranes. Hereafter, we will only focus on the thermotropic liquid crystals.

The simplest liquid crystalline phase is the nematic phase. The name *nematic* comes from the Greek word for thread. In the nematic state, the rod-like LC molecules align in a preferred orientational direction, denoted by the director field **n**; deviations from this alignment cost elastic energy owing to the bend, twist and splay of the molecules [127]. There is growing interest in using LCs as media to template the assembly of particles by using director configurations and hence elastic energy fields. Particles placed in oriented LCs perturb the director field, eliciting a change in elastic energy that moves them to preferred locations or causes them to interact. Most studies so far focus on spherical colloidal assembly in the bulk LCs [120, 122, 128, 129]. Spherical colloids form either dipolar or quadrupolar defect structures in nematic films, depending on the anchoring conditions at the particle surface [122], as well as the nature of their confinement [128]. In the far field, particles interact as elastic multipoles; in the near field, the details of the director field rearrangement near the particles cement the assemblies [120]. More recently, the role of complex particle shape has been explored, with sharp edges and corners playing important roles in creating large distortions and defects in the LC director field [130, 131, 121, 132, 133, 134, 135, 136]. In particular, moderate aspect ratio cylinders with homeotropic anchoring and associated dipolar defects in uniform nematic films chain and orient with the director field [130, 135].

6.2.1. Capillarity and Elasticity

Even for spherical colloids, the air/nematic interface is a rich environment, for example, microspheres with homeotropic anchoring, or perpendicular alignment of LC molecules to particle surface, self-organize into 2D crystalline lattices on hybrid nematic films[137]. By confining nematic LC films in cells with antagonistic anchoring conditions, defects can be forced into the nematic bulk with well-defined geometries and locations [24]. The resulting elastic energy fields propagate far from the defects and guide particle assembly on interfaces as distant as 50 microns from the defect itself [24, 138]. So far, only spherical particle interactions have been reported at nematic interfaces; for such particles, capillary interactions caused by particle-sourced distortions of the interface are typically weak [138]. Anisotropic particles, however, create large deformations in the interface, with large associated capillary interactions.

Capillary interactions at planar isotropic fluid interfaces arise between particles with non-spherical shapes, or, in principle, spherical particles with pinning sites or chemical patchiness. The undulated contact line where liquid, vapor and particle meet distorts the interface around the particles. To minimize the area of the interface, particles orient and assemble [39, 139] to equilibrium distances influenced by near field capillary attraction or repulsion [76]. At curved isotropic fluid interfaces, the particle-induced deformations interact with the interface curvature [20, 52, 63, 100, 108]. In particular, cylindrical particles on planar interfaces attract in mirror symmetric orientations and assemble to form rigid, linear chains [63, 64]. On curved interfaces, they orient along principal axes of the interface and migrate to sites of high curvature [20].

6.3. Motivation

While directed assembly of colloids to form organized structures is often guided by external applied fields [140, 141, 142], recent advances instead rely on interactions that emerge when particles are placed in a soft material. Two important examples are elastic interactions between particles in liquid crystals (LCs) [24, 124, 125, 126, 137, 138], and capillary interactions between particles at fluid interfaces [39, 61, 64, 76]. Well defined director fields with associated elastic energy landscapes can be imposed by confining nematic LCs between surfaces that favor given molecular orientations. When particles are introduced, they elicit an elastic response that moves them to preferred locations or drives them to interact with each other [120, 122, 128, 129]. Capillary interactions occur between particles trapped at fluid interfaces; the particles distort the interface and assemble to minimize the interfacial area [39, 139]. Interface curvature fields can steer particles along well-defined paths and orient them via curvature capillary energies. Since both fluid interfaces and LC director fields are readily reconfigured, a deeper understanding of these mechanisms paves the way for responsive or reconfigurable materials. Can capillarity and elasticity together direct interactions between colloids on free surfaces of nematic films? To our knowledge, thus far, only spherical colloids have been studied at nematic interfaces; for such particles, capillary interactions are typically weak [138]. Anisotropic particles, however, create larger interface deformations with associated significant capillary interactions, as has been established in studies on isotropic fluids with planar [63, 64] and curved interfaces [20].

An *a priori* comparison of capillarity to elastic interactions suggests that capillarity would dominate, and elasticity would not play an important role. For example, a particle of radius $R \sim 10^{-5} m$ on a nematic LC of average elastic constant $K \sim 10^{-11} N$ with surface tension $\gamma \sim 10^{-2} N m^{-1}$ has an elasto-capillary number $\frac{\gamma R}{K} \sim 10^3 - 10^4$, indicating that capillary effects are far larger than those of elastic origin. However, a more careful scrutiny of the magnitude of these interactions on, for example, cylindrical microparticles indicates otherwise. When immersed in an oriented hybrid nematic film, cylindrical microparticles of length L and radius R chain by elastic dipolar interactions and orient along the director field, with elastic energies and torques $\sim KL$ [130, 135]. On fluid interfaces, such microparticles distort fluid interfaces with characteristic deformation magnitudes $H_p << R$ and associated capillary energy $\sim \gamma {H_p}^2$. For this situation, the ratio of capillary to elastic energies is far smaller, indicating that there may be a more interesting interplay of these effects. We probe this interplay in a study of cylindrical microparticles with homeotropic anchoring at free surfaces of an aligned hybrid nematic film, a system in which elastic effects and capillary effects can play complementary or competing roles.

6.4. Materials and Methods

6.4.1. Lithographic cylindrical colloid fabrication and surface treatment

A microcylinder array is fabricated from negative tone epoxy photoresist SU-8 (Microchem Corp.) using standard photolithographic procedures. In short, the negative tone epoxy photoresist SU-8 is spin-coated onto a plasma-cleaned silicon wafer. After soft baking the wafer, the photoresist is exposed to UV light (365nm) on a tabletop mask aligner (OAI Model 100) through a photomask (Microtronics Inc., Fine Line Imaging). Subsequently, the wafer is heated to crosslink the UV-exposed regions, and immersed in SU-8 developer to dissolve the undeveloped epoxy. The resulting microcylinders in these arrays have nominal radii R=5 μm, and length L=25 μm. To impose anchoring conditions, the microcylinder arrays are sputtered with a 30 nm film of chromium. After releasing the microcylinders from the wafer by scraping the wafer with a razor blade, the particles are sputtered a second time to ensure that all sides of the particles are covered with chromium. To induce strong homeotropic anchoring, cylindrical particles are treated with a 3% weight solution of N,N-dimethyl-N-octadecyl-3-aminopropyltrimethoxysilyl chloride (DMOAP, Sigma-Aldrich) in a mixture of 90% weight of ethanol, and 10% weight of water solution, for one hour at 80°C. Particles are subsequently cleaned by repeated cycles of rinsing, centrifugation, and decanting in water. Microcylinders are then dried in the oven overnight to evaporate solvent.

6.4.2. Substrate preparation: Planar interface

Planar anchoring of nematic LC on the glass substrate is achieved by treating glass microscope slides with a solution of 1% weight polyvinyl alcohol (PVA) dissolved in a mixture of ethanol and water (10:90 wt/wt). The substrates are first spin-coated with the PVA solution at 2000 rpm for 20 seconds, and heated in the oven at 110°C for one hour. The PVA treated glass substrates are then rubbed in one direction with a velvet cloth to ensure unidirectional planar alignment. A nematic film is formed by spin-coating a small droplet of 4-cyano-4-pentylbiphenyl (5CB) on the glass substrate. The thickness of the film is controlled by the spin-coating speed.

6.4.3. Substrate preparation: Curved interface

The curved interface is molded simply by placing an SU-8 microdisk of height approximately 50μm and diameter 350μm on the glass substrate which is already covered with a nematic film. The nematic film pins at the top edge of the microdisk creating a monopole deformation of the interface. The angle of the curved interface at the edge of the microdisk is between 10-15°.

6.4.4. Particle dispersion and Microscopy

The particles are placed on nematic films prepared over either planar substrates to form a planar air/nematic interface or around microdisks to create well defined curvature fields. The anchoring of the nematic film is hybrid: planar at the glass substrate and perpendicular in contact with air.

The microparticles are placed on air/nematic interfaces by aerosolizing them and allowing them to sediment through air and attach to the interface. Once attached, the particles are no longer affected by gravity, as is reflected in the small value of the Bond number, the ratio between gravitational forces and interfacial tension Bo=$\Delta\rho g {L_c}^2/\gamma \sim 10^{-6}$, where $\Delta\rho$ is the density difference between particle and liquid crystals ($\rho_{SU-8} = 1200 kg/m^3$ and $\rho_{5CB} =$

$1008 kg/m^3$), g is the gravitational acceleration constant, L_c is the particle characteristic length ($L_c = 12.5 \times 10^{-6}$m), and γ is the interfacial tension between two liquids ($\gamma_{5CB-air} = 3.8 \times 10^{-2} N/m$) [143]. Cylinders of aspect ratio 2.5 typically assume a side-on configuration with the particle long axis in the plane of the interface [63, 144].

Particle behavior is observed using bright field (BF) and polarized optical microscopy (POM) in transmission mode under an upright optical microscope (Zeiss AxioImager M1m, Carl Zeiss, Oberkochen, Germany). Images and videos are taken with a high-resolution camera (Zeiss AxioCam HRc). Particle orientation and trajectory are analyzed using ImageJ.

6.5. Results and Discussion

In our experiments, we study microcylinders deposited on the free surface of a hybrid aligned nematic film. The film has oriented planar anchoring on the substrate and homeotropic anchoring at the free surface. The significant bending of the director across the film thickness provides an elastic environment that can couple to distortions or defects in the director field created by the particles. Microcylinders with homeotropic anchoring are introduced onto this surface by creating an aerosol, and subsequently allowing them to sediment through air and attach to the interface (Fig.6.1a).

Once attached, the microcylinders align along the easy axis of the nematic film, corresponding to the direction of the oriented planar anchoring on the substrate. This orientation occurs robustly for films of $h \approx 25 \mu m$. This elastic alignment is enforced by a torque that rotates nanowires [133] or bullet like particles [131] immersed within uniform LC, and can be attributed to the coupling of the topological defect created by the microcylinder and the prevailing director field. The microrods create a point defect at one of their flat ends (see Fig.6.1b and c) which is similar to the hyperbolic hedgehog observed around homeotropic beads trapped at air/nematic [137] or water/nematic interfaces [145, 146]. As expected, the elastic defect and the associated alignment disappear when the nematic is heated to the isotropic phase (see Fig.6.1d and e). For larger film thicknesses (above $h \approx 50\mu m$), the elastic coupling vanishes and cylinders become randomly oriented.

In addition to elastic deformations, the cylinders deform the fluid interface. Interferometric images (Fig.6.2a) reveal the quadrupolar symmetries of this distortion, with rise at the planar ends of the cylinder and weak downward deflections along the sides, qualitatively similar to the behavior at the air/water interface [91]. This distortion has a polar quadrupolar mode that determines the long range interactions of the particles [61]. The magnitude of the polar quadrupolar deformation at the air/nematic interface of an isolated cylinder measured 3 radii from the particle center is $H_p = 174nm \pm 30nm$, independent of the liquid crystal film thickness (Fig.6.2b).

These particles could, in principle, interact either via capillarity, elastic interactions, or both. To discern the prevailing energies, trajectories of interacting particles were captured using video microscopy. Typically, both elasticity and inertia are negligible, as reflected by values of the Ericksen number $Er = \eta\nu L_c/K \approx 10^{-2}$ and the Reynolds number, $Re = \rho_{5CB}\nu L_c/\eta \approx 10^{-7}$, respectively. In these expressions, $\eta = 14.21mPa \cdot s$ is the viscosity of 5CB, ν is the bulk fluid velocity, L_c is the characteristic length of the particle, *i.e* the cylinder length, ρ_{5CB}=1.008g/ml is the density of 5CB, and $K \sim 10^{-11}N$ is the average Frank elastic constant. Thus, particle migrations are balanced by viscous dissipation, which can be treated in the context of a Newtonian viscous fluid. To understand the drag on the particle, we record the Brownian trajectories of an isolated particle on the film at a rate of 70ms per frame for approximately 12 minutes. The microcylinders are affected both by the anisotropic alignment of the director and the particle shape. The instantaneous velocity of the particle between each video frame, is determined in directions both parallel and perpendicular with the director field. From these data, the diffusion coefficient along the easy axis and that perpendicular to it are determined to be $6.26 \times 10^{-3}\mu m^2/s$ and $1.39 \times 10^{-3}\mu m^2/s$, respectively. For the purpose of estimating potentials, an average of two diffusion coefficients was used in the Stokes-Einstein equation to find the Stokes drag coefficient.

On an isotropic fluid interface, cylindrical particles assemble in mirror symmetry to form an end-to-end chain by capillarity [63]. The existence of an easy axis in this system alters these trajectories. There are two scenarios observed for this assembly depending upon the orientation of the vector defining the center to center distance between the particles **r**. Either **r** is parallel to the easy axis or it is not. When **r** is parallel to the easy axis, the microcylinders remain aligned along this axis as they approach in an end-end configuration (see Fig.3). The interaction potential has elastic and capillary contributions

$$U_{total} = U_{elastic} + U_{capillary} \tag{6.1}$$

$$U_{total} = -K(LR)^2 r^{-3} - 12\pi\gamma {H_p}^2 \cos(2\varphi_A + 2\varphi_B){L_c}^4 r^{-4} \tag{6.2}$$

In this expression, the first term is an attractive elastic dipole-dipole interaction between the cylinders assuming a small angle difference between the major axis of the two particles [131]. In this expression $L = 25 \times 10^{-6} m$ is the length of the microcylinder, $R = 5 \times 10^{-6} m$ is its radius, and r is the particle center to center separation distance. The elastic potential at $r = 110 \mu m$ is about $2.8 \times 10^1 k_B T$. The second term is the capillary contribution, with pair potential between polar capillary quadrupoles [61]. In this expression, H_p is the magnitude of the quadrupolar distortion due to a cylinder, and φ_A and φ_B are the orientation of the quadrupolar rise axis of particle A and B, respectively. The capillary contribution to the interaction at $r = 110 \mu m$ is of $1.8 \times 10^3 k_B T$, two orders of magnitude greater than the elastic potentials. Thus, assembly is indeed dominated by capillarity while the alignment is enforced by elasticity. The particle trajectory versus time obeys the expected 1/6 power-law dependence for interacting polar quadrupoles in the interface in the far field (see Fig.6.3). This power law results from a balance of the prevailing interaction force with viscous dissipation [63, 68], i.e. $F_{drag} = F_{capillary}$, where $F_{drag} = C_D L_c \eta \frac{dr}{dt}$ and $F_{capillary} = 48\pi\gamma {H_p}^2 \cos(2\varphi_A + 2\varphi_B){L_c}^4 r^{-5}$. In this expression, C_D is the diffusion coefficient. This balance allows us to identify the pre-factor to the power law:

$$\left(\frac{48\pi\gamma {H_p}^2 \cos(2\varphi_A + 2\varphi_B){L_c}^3}{C_D \eta}\right)^{1/6} t^{1/6} = r \tag{6.3}$$

When $\mathbf{r}$ is not parallel to the easy axis, both capillary and elastic effects are evident in the particle dynamics. Microcylinders first assemble into an end-to-end structure at an angle with respect the director field via capillarity (Fig.6.4a) with orientations that deviates from mirror symmetry. Thereafter, an elastic torque rotates the assembled chain to re-align it along the easy axis (Fig.6.4a and b). Similarly, chains of particles can form by successive capillary interactions and rotations. Fig.6.4c shows elastic rotation on the film interface of chain lengths 3, 4, 5, and 7 particles. This elastic torque can be approximated as $T_{elast} = -KL_c\theta$ for small angle θ between the chains long axis and the easy axis. The elastic torque is balanced by the viscous drag on the particle,

$$T_{elast} = -KL_c(\theta - \theta_f) = \sigma\eta\frac{\partial\theta}{\partial t} \tag{6.4}$$

where σ is the rotational drag coefficient of the chain [147]. Upon integration, the particle positions may be characterized as a function of time and chain length:

$$\theta(t) = C_o e^{-\frac{KL_c}{\sigma\eta}t} \tag{6.5}$$

where C_o is a constant that can be computed from the cylinder's initial and final orientation. In Fig.6.4b, $\theta(t)$ is reported, where the abscissa indicates time since the chain formation, as indicated that the experimental results are in a good fit with theory for chain comprising four particles. In a hybrid nematic film, the elastic energy is inversely related to the film thickness [148],

$$F_{FO} = \frac{1}{2} K \frac{(\bar{\theta}_o - \bar{\theta}_h)^2}{h} \tag{6.6}$$

where $\bar{\theta}_o$ is the angle of the liquid crystal molecule on the substrate, $\bar{\theta}_h$ is the angle of the liquid crystal molecule at the air/nematic interface, and h is the thickness of the nematic film. Hence as film thickness increases, the alignment and torque weaken significantly. As we observed in experiment, these effects are completely absent for films thicker than $50\mu m$.

6.5.1. Elasto-capillary interactions on curved interface

Microcylinders on interfaces with finite deviatoric curvatures align along principle axes and migrate to sites of high curvature owing to capillarity [20]. Here we study the interplay of this capillary alignment and the elasticity enforced alignment along the easy axis.

The curved nematic film covers a region roughly 2 cm in diameter, centered around the SU-8 microdisk of height $50\mu m$ and diameter $350\mu m$, respectively. Microcylinders are aerosolized and dispersed onto the surface molded around the microdisk (See schematic in Fig.6.5a). The interface shape $h(r_m)$ is axially symmetric that the interface height profile, obtained by interferometry, in four directions from the center of the microdisk collapse into one curve in Fig.6.5a. From the data, the interface slopes and curvatures can be determined directly.

This interface shape has zero mean curvature $H_0 = \frac{1}{2}(c_1 + c_2)$ and finite deviatoric curvature is given by :

$$\Delta c = c_1 - c_2 = \frac{1}{R_1} - \frac{1}{R_2} \tag{6.7}$$

where R_1 and R_2 are the radii of curvature along the two principal axes, and $c_1 = \frac{1}{R_1}$ and $c_2 = \frac{1}{R_2}$ are local principal curvatures, defined so that $c_1 \geq c_2$. For our interface shape, given that mean curvature is zero, $c_1 = -c_2$ From the expression for the interface height, the deviatoric curvature can be found:

$$\Delta c = \frac{d^2h}{dr_m^2} - \frac{1}{r_m}\frac{dh}{dr_m} = 2\frac{d^2h}{dr_m^2} \tag{6.8}$$

Note that at the contact line where LC, air and microdisk meet, the height of the nematic is still within the range where cylindrical particles can sense the easy axis on planar films. Therefore, we select this height regime to ascertain whether curvature-alignment or nematic-alignment will dominate. We report particle behaviors for distances from the microdisk center r_m up to $1500\mu m$ microns, for which the height varies from $25\mu m$ to $50\mu m$. Microcylinders attach to the interface, and rotate to align their major axis along the radial direction (see Fig.6.5b); in this configuration, the rise axis of the particle-sourced quadrupole aligns along the rise of the monopole. For all microparticles observed within roughly $1200\mu m$ from the center of the post, radial alignment is observed. Once attached, microparticles migrate along a radial trajectory towards the post, along the curvature gradient. In this region, particle alignment is dominated by capillarity.

For particles located between 1200 to $1300\mu m$ from the center of the microdisk, particles transition from a curvature capillary alignment to elastic field dominated behavior (as shown in Fig.6.5b, the yellow arc depicts a segment of a circle drawn with a radius of $1300\mu m$). Particles in this region transition from radial alignment to alignment along the easy axis. In one observation, a weak flow field moved particles from the elastic-dominated to curvature-capillary-dominated regions. Microcylinders convected toward the microdisk slowly rotate from alignment along the easy axis to radial alignment.

The identification of the location where elastic alignment and capillary alignment compete allows us to estimate the torque from both viewpoints. The capillary torque for particles rotating from alignment along one principle axis to the other is given simply by $T_{cap} = 2\pi\gamma {L_c}^2 H_p \Delta c$ [91]. Evaluating this torque at $r_m = 1300\mu m$, $T_{cap} = 3.2 \times 10^4 k_B T$. At the same location, the elastic torque T_{elast} on a film of thickness $h \approx 25\mu m$ (the height at this distance from the post) can be estimated using equation (6.4) to be $4.8 \times 10^4 k_B T$, comparable to the capillary torque. Closer to the microdisk, elastic torques decrease while capillary torques increase, explaining the observed crossover behavior.

6.6. Conclusions

In conclusion, cylindrical particles at free surfaces of hybrid nematic films display a rich interplay of capillary and elastic interactions. The particles orient along the director easy axis on nematic films that are sufficiently thin. Pairs of particles form chains by capillarity, which rotate to align along the easy axis by an elastic torque. We characterize this elastic torque for chains of varying length. On curved fluid interfaces, curvature capillary orientation and migration compete with the elastic field for curvatures which are sufficiently steep. Transition regions where curvature is weak enough for elastic-enforced alignment to be restored are identified. By developing this understanding, we establish new assembly tools with important degrees of freedom to assemble and orient responsive materials.

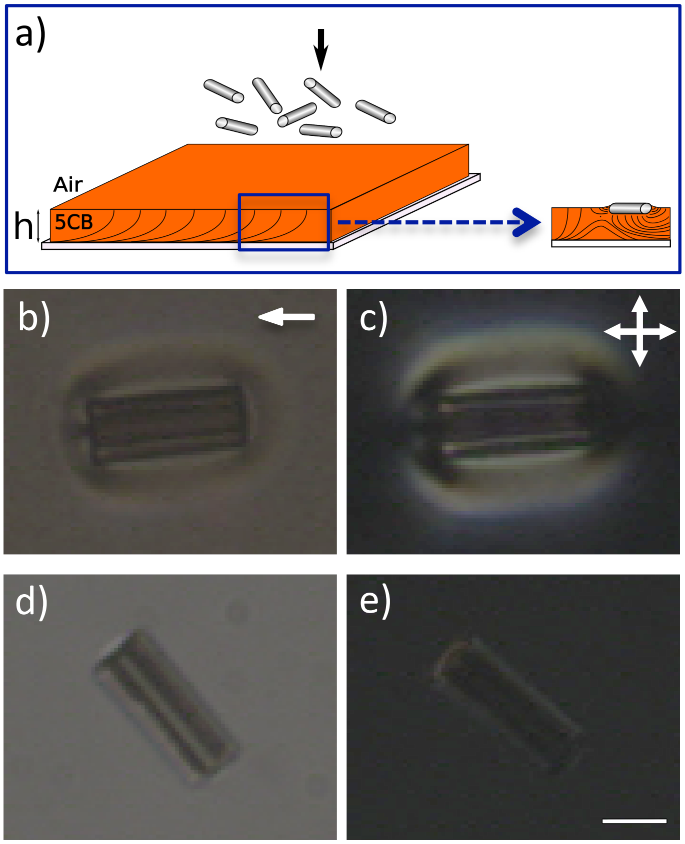

Figure 6.1: Schematic of microcylinders on hybrid thin nematic film. (a). Optical images of a microcylinder with homeotropic anchoring on a thin uniform nematic film ($h \approx 25\mu m$) of 5CB in the nematic phase: (b) in bright field and (c) under cross polarizers, and in the isotropic phase: (d) in bright field and (e) under cross polarizers. In the nematic phase, a point defect is observed on one flat end of the cylinder that disappears when heated to the isotropic phase. White arrow indicates the directions of liquid crystal alignment. Scale bar is $10\mu m$.

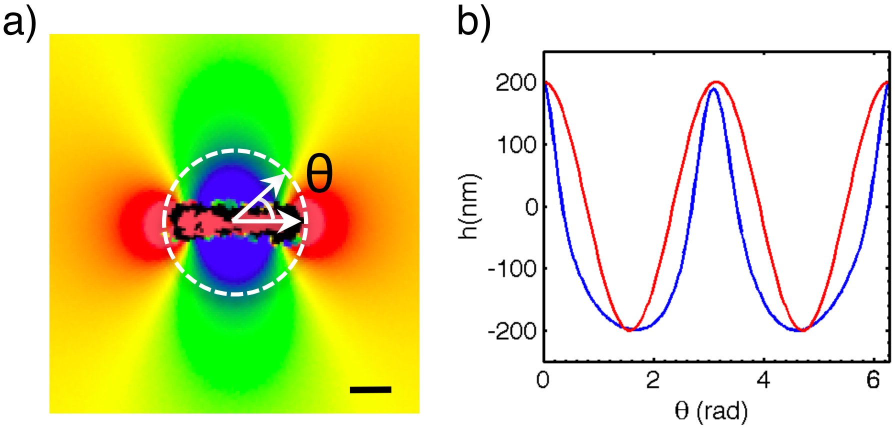

Figure 6.2: Interfacial deformation of microcylinders. (a) Interferogram of a cylinder at an air/nematic interface. (b) The interface distortion (blue curve) has polar quadrupolar mode (red curve) of amplitude $174 \pm 30nm$ measured 3 radii from the particle center. Scale bar is $10\mu m$.

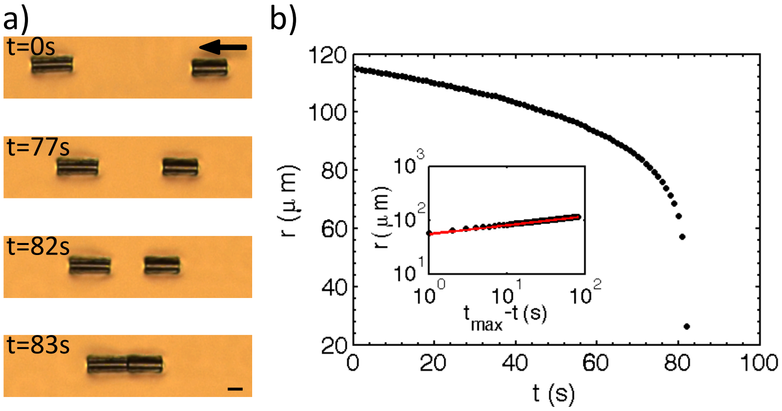

Figure 6.3: Cylinders assemble into end-to-end chain on a hybrid nematic film. (a) Time-lapsed image of cylinder assembly. (b) Particle center to center separation distance, r, as a function of time, t, extracted from particle tracking. Inset: $\log r$ vs $\log(t_{max} - t)$ shows a power law of $t^{1/6}$ power. Arrow indicates the directions of liquid crystal alignment. Scale bar is $10\mu m$.

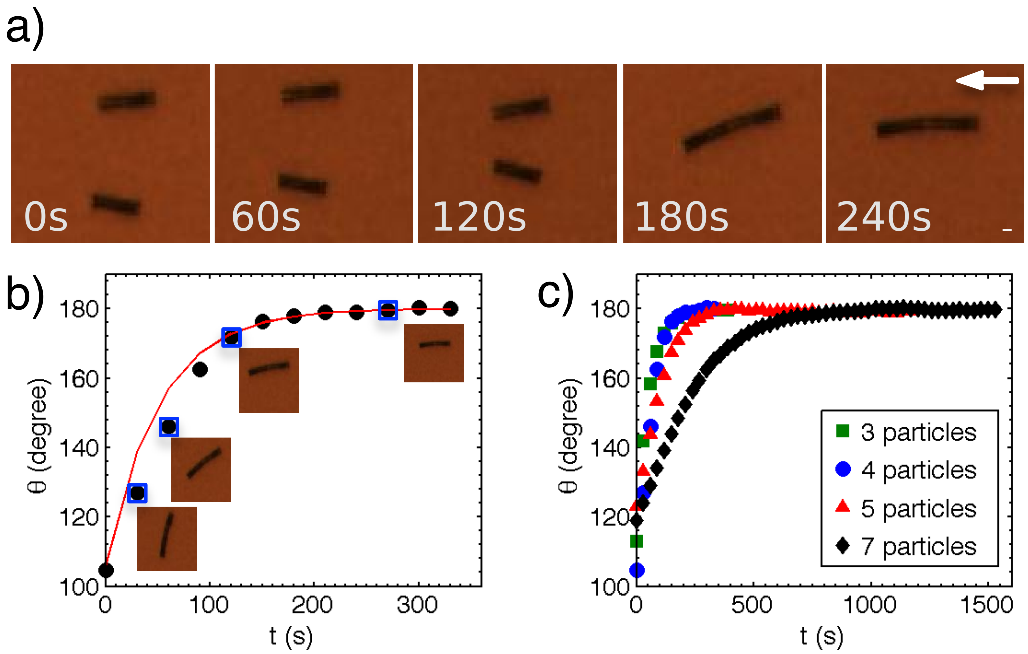

Figure 6.4: Upon forming a rigid chain, the aggregate rotates such that the chain axis aligns parallel to the director field (a). Elastic rotation rate of a chain comprising four particles (b). Rotations observed on the interface for chains of $75\mu m$, $100\mu m$, $125\mu m$, and $175\mu m$ in lengths (c). Arrow indicates the directions of liquid crystal alignment. Scale bar is $10\mu m$.

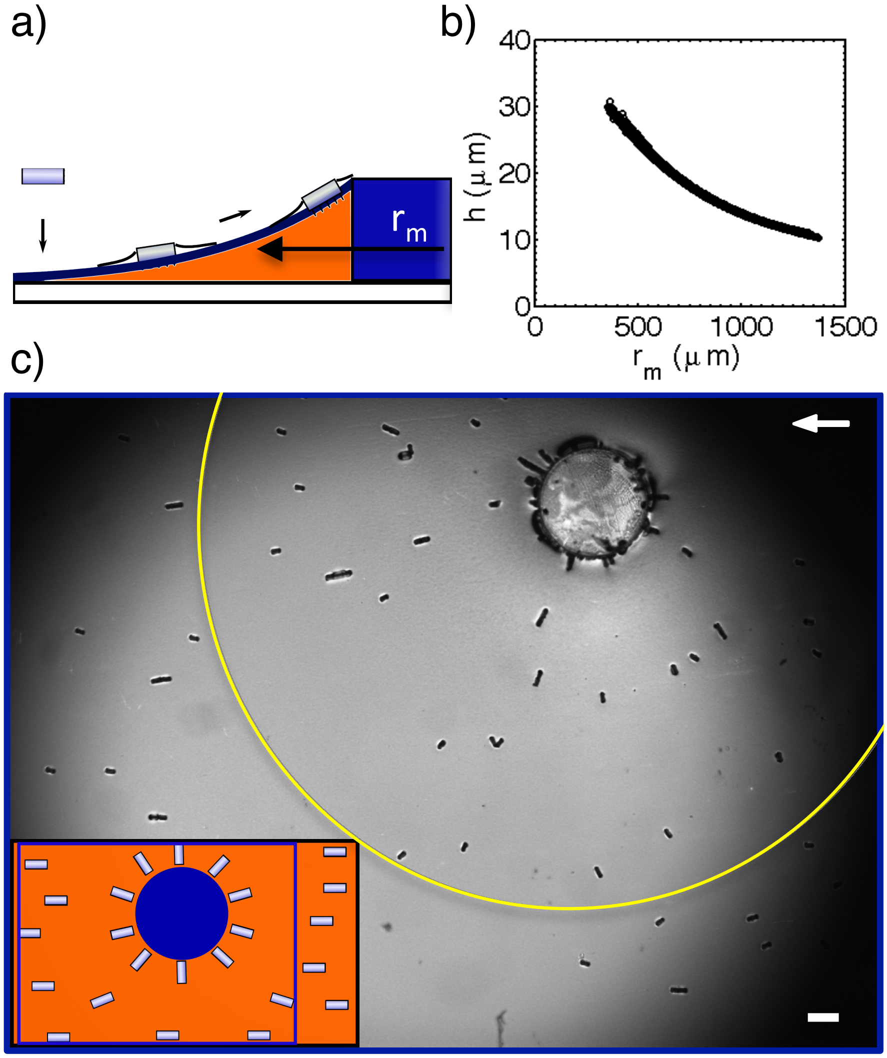

Figure 6.5: Microcylinders on a curved interface. (a) Schematic of the side view of the interface (r_m indicates the radial distance from the center of the microdisk). Inset: Interface height profile obtained by interferometry shown as black circles. (b) Top view optical image of the curved interface. After dispersing particles at the curved interface, particles within the yellow circle located at $r_m = 1300\mu m$, align radially towards the microdisk. Particles outside of this curve,align with the director field. Microdisk diameter is $350\mu m$, height $50\mu m$. Scale bar is $100\mu m$. Inset: Schematic of alignment of microcylinders.

APPENDIX A

A.1. Reflected mode

A.1.1. Problem statement

We have based our previous analysis for particles around microposts with pinned contact lines on the interaction of the particle-imposed quadrupole $h_A = h_{qp}\frac{a^2}{{r_A}^2}\cos 2(\varphi_A - \alpha_A)$ and the reflection from the particle of the local curvature field from the post: $\eta_A = -\frac{\Delta c_0}{4}\frac{a^4}{{r_A}^2}\cos 2(\varphi_A)$, which yields the curvature capillary energy:

$$E = E_{planar} - \gamma\pi\frac{h_{qp}a^2\Delta c_0}{2}\cos 2(\alpha_A), \tag{A.1}$$

where angle α_A defining the orientation of the quadrupolar rise axis of A is defined counter-clockwise from the x_A axis. For the case of a singular perturbation in powers of $\frac{a}{L}$, in which the particle-sourced distortion decays before reaching the micropost, this is the solution. If, however, the particle-sourced distortion is not negligible at the micropost, and micropost has a pinned contact line, there is a reflected mode owing to the particle-sourced distortion h_A from the post. Here we evaluate that contribution.

A.1.2. Taylor Series of disturbance from particle A at the post

Noting $x_A = x_M + L$ and $y_A = y_M$, we find h_A near the micropost.

$$h_A(x_M,y_M) = h_{qp}\frac{a^2}{(x_M+L)^2 + {y_M}^2}\cos 2\left(\tan^{-1}\frac{y_M}{x_M+L} - \alpha_A\right) \tag{A.2}$$

To expand this in a Taylor series near 0_M, which is the center of the micropost:

$$\begin{aligned} h_A(x_M,y_M) \approx{} & h_A(x_M=0,y_M=0) + \nabla h_A(x_M=0,y_M=0)\cdot\mathbf{x}_M \\ & + \frac{\mathbf{x}_M\cdot\nabla\nabla h_A(x_M=0,y_M=0)\cdot\mathbf{x}_M}{2} \end{aligned} \tag{A.3}$$

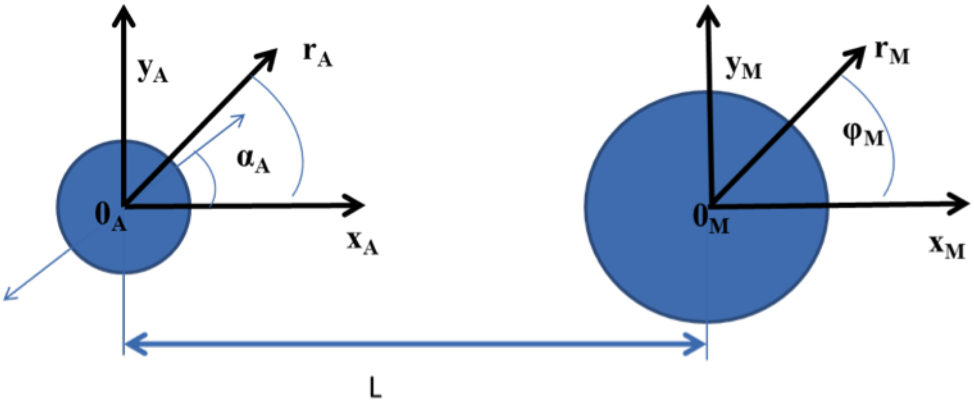

Figure A.1: Schematic of particle A and micropost M. A is a quadrupolar surface deflection of magnitude h_{qp} and radius a separated from the micropost by the distance L. Arrows indicate orientation of quadrupolar rise axes. The angle α_A defining the orientation of the quadrupolar rise axis of A is defined counterclockwise from the x_A axis.

We first evaluate:

$$h_A(x_M = 0, y_M = 0) = h_{qp}\frac{a^2}{L^2}\cos(2\alpha_A) \tag{A.4}$$

Define two variables ζ and Υ:

$$\zeta = (x_M + L)^2 + {y_M}^2 \tag{A.5}$$

$$\Upsilon = \tan^{-1}\frac{y_M}{x_M + L} \tag{A.6}$$

from which one can show:

$$\frac{\partial\zeta}{\partial x_M} = 2(x_M + L) \tag{A.7}$$

$$\frac{\partial\zeta}{\partial y_M} = 2y_M \tag{A.8}$$

$$\frac{\partial\Upsilon}{\partial x_M} = \frac{(x_M + L)^2}{(x_M + L)^2 + {y_M}^2}\frac{-y_M}{(x_M + L)^2} = \frac{-y_M}{\zeta} \tag{A.9}$$

$$\frac{\partial\Upsilon}{\partial y_M} = \frac{(x_M + L)^2}{(x_M + L)^2 + {y_M}^2}\frac{1}{(x_M + L)} = \frac{(x_M + L)}{\zeta} \tag{A.10}$$

Recast h_A in terms of ζ and Υ,

$$h_A(x_M,y_M) = h_{qp}a^2\zeta^{-1}\cos 2\left(\Upsilon - \alpha_A\right) \tag{A.11}$$

Compute the partial derivatives of h_A, and evaluate at $x_M = 0, y_M = 0$,

$$\frac{\partial h_A}{\partial x_M} = -2h_{qp}a^2\zeta^{-2}(x_M + L)\cos 2\left(\Upsilon - \alpha_A\right) + 2h_{qp}a^2\zeta^{-2}\sin 2\left(\Upsilon - \alpha_A\right)(y_M) \tag{A.12}$$

$$\left.\frac{\partial h_A}{\partial x_M}\right|_{0_M} = -2h_{qp}a^2L^{-3}\cos 2\alpha_A \tag{A.13}$$

$$\frac{\partial h_A}{\partial y_M} = -2h_{qp}a^2\zeta^{-2}(y_M)\cos 2\left(\Upsilon - \alpha_A\right) - 2h_{qp}a^2\zeta^{-2}\sin 2\left(\Upsilon - \alpha_A\right)(x_M + L) \tag{A.14}$$

$$\left.\frac{\partial h_A}{\partial y_M}\right|_{0_M} = 2h_{qp}a^2L^{-3}\sin 2\alpha_A \tag{A.15}$$

Using the derivatives from above, we find ∇h_A,

$$\begin{aligned}\nabla h_A = &- 2h_{qp}a^2\zeta^{-2}\cos 2\left(\Upsilon - \alpha_A\right)\left((x_M + L)\delta_{x_M} + y_M\delta_{y_M}\right)\\ &+ 2h_{qp}a^2\zeta^{-2}\sin 2\left(\Upsilon - \alpha_A\right)\left(y_M\delta_{x_M} - (x_M + L)\delta_{y_M}\right)\end{aligned} \tag{A.16}$$

Evaluating ∇h_A at the center of the micropost, $x_M = 0, y_M = 0$

$$\left.\nabla h_A\right|_{0_M} = -2h_{qp}a^2L^{-4}\left[L\cos 2\alpha_A\delta_{x_M} - L\sin 2\alpha_A\delta_{y_M}\right] \tag{A.17}$$

Noting that $\delta_{x_M} = r_M\cos\varphi_M$ and $\delta_{y_M} = r_M\sin\varphi_M$,

$$\begin{aligned}\left.\nabla h_A\right|_{0_M}\cdot\mathbf{r}_M &= -2h_{qp}a^2L^{-3}\left[\cos 2\alpha_A r_M\cos\varphi_M - \sin 2\alpha_A r_M\sin\varphi_M\right]\\ &= -2h_{qp}a^2R_ML^{-3}\left[\frac{r_M}{R_M}\cos 2\alpha_A\cos\varphi_M - \frac{r_M}{R_M}\sin 2\alpha_A\sin\varphi_M\right]\\ &= -2h_{qp}a^2R_ML^{-3}\frac{r_M}{R_M}\left[\cos 2\alpha_A\cos\varphi_M - \sin 2\alpha_A\sin\varphi_M\right]\\ &= -2h_{qp}a^2R_ML^{-3}\frac{r_M}{R_M}\cos(2\alpha_A + \varphi_M)\end{aligned} \tag{A.18}$$

Let $r_M = R_M$, where R_M is the radius of the micropost,

$$\left(\nabla h_A\big|_{0_M} \cdot \mathbf{r}_M\right)\Big|_{r_M=R_M} = -2h_{qp}a^2R_ML^{-3}\cos(2\alpha_A + \varphi_M) \tag{A.19}$$

Now, compute the second derivatives of h_A,

$$\begin{aligned}\frac{\partial}{\partial x_M}\frac{\partial h_A}{\partial x_M} &= 8h_{qp}a^2\zeta^{-3}(x_M + L)^2\cos 2\left(\Upsilon - \alpha_A\right)\\ &\quad - 2h_{qp}a^2\zeta^{-2}\cos 2\left(\Upsilon - \alpha_A\right)\\ &\quad - 4h_{qp}a^2\zeta^{-3}y_M(x_M + L)\sin 2\left(\Upsilon - \alpha_A\right)\\ &\quad - 8h_{qp}a^2\zeta^{-3}y_M(x_M + L)\sin 2\left(\Upsilon - \alpha_A\right)\\ &\quad - 4h_{qp}a^2\zeta^{-3}{y_M}^2\cos 2\left(\Upsilon - \alpha_A\right)\end{aligned} \tag{A.20}$$

$$\begin{aligned}\frac{\partial}{\partial y_M}\frac{\partial h_A}{\partial y_M} &= 8h_{qp}a^2\zeta^{-3}{y_M}^2\cos 2\left(\Upsilon - \alpha_A\right)\\ &\quad - 2h_{qp}a^2\zeta^{-2}\cos 2\left(\Upsilon - \alpha_A\right)\\ &\quad + 4h_{qp}a^2\zeta^{-3}y_M(x_M + L)\sin 2\left(\Upsilon - \alpha_A\right)\\ &\quad + 8h_{qp}a^2\zeta^{-3}y_M(x_M + L)\sin 2\left(\Upsilon - \alpha_A\right)\\ &\quad - 4h_{qp}a^2\zeta^{-3}(x_M + L)^2\cos 2\left(\Upsilon - \alpha_A\right)\end{aligned} \tag{A.21}$$

Upon evaluation at $x_M = 0, y_M = 0$ this reduces to:

$$\begin{aligned}\frac{\partial}{\partial x_M}\frac{\partial h_A}{\partial x_M}\bigg|_{0_M} &= 8h_{qp}a^2L^{-6}(L)^2\cos 2\alpha_A - 2h_{qp}a^2L^{-4}\cos 2\alpha_A\\ &= 6h_{qp}a^2L^{-4}\cos 2\alpha_A\end{aligned} \tag{A.22}$$

$$\begin{aligned}\frac{\partial}{\partial y_M}\frac{\partial h_A}{\partial y_M}\bigg|_{0_M} &= -4h_{qp}a^2L^{-6}(L)^2\cos 2\alpha_A - 2h_{qp}a^2L^{-4}\cos 2\alpha_A\\ &= -6h_{qp}a^2L^{-4}\cos 2\alpha_A\end{aligned} \tag{A.23}$$

The mixed second partial derivative is

$$\begin{aligned}
\frac{\partial}{\partial x_M}\frac{\partial h_A}{\partial y_M} &= 8h_{qp}a^2\zeta^{-3}y_M(x_M+L)\cos 2\left(\Upsilon-\alpha_A\right) \\
&+ 4h_{qp}a^2\zeta^{-3}{y_M}^2\sin 2\left(\Upsilon-\alpha_A\right) \\
&+ 8h_{qp}a^2\zeta^{-3}(x_M+L)^2\sin 2\left(\Upsilon-\alpha_A\right) \\
&+ 4h_{qp}a^2\zeta^{-3}y_M(x_M+L)\cos 2\left(\Upsilon-\alpha_A\right) \\
&- 2h_{qp}a^2\zeta^{-2}\sin 2\left(\Upsilon-\alpha_A\right)
\end{aligned} \tag{A.24}$$

Evaluate the second partial derivative at $x_M = 0, y_M = 0$,

$$\begin{aligned}
\left.\frac{\partial}{\partial x_M}\frac{\partial h_A}{\partial y_M}\right|_{0_M} &= -8h_{qp}a^2L^{-6}(L)^2\sin 2\alpha_A + 2h_{qp}a^2L^{-4}\sin 2\alpha_A \\
&= -6h_{qp}a^2L^{-4}\sin 2\alpha_A
\end{aligned} \tag{A.25}$$

Evaluating $\mathbf{r}\cdot\nabla\nabla h_A|_{0M}\cdot\mathbf{r}$,

$$\begin{aligned}
\mathbf{r}\cdot\nabla\nabla h_A|_{0M}\cdot\mathbf{r} &= {r_M}^2\cos^2\varphi_M h_{A,xx} + {r_M}^2\sin^2\varphi_M h_{A,yy} + 2r_M\cos\varphi_M\sin\varphi_M h_{A,xy} \\
&= {r_M}^2\cos^2\varphi_M(6h_{qp}a^2L^{-4}\cos 2\alpha_A) + {r_M}^2\sin^2\varphi_M(-6h_{qp}a^2L^{-4}\cos 2\alpha_A) \\
&\quad + 2{r_M}^2\cos\varphi_M\sin\varphi_M(-6h_{qp}a^2L^{-4}\sin 2\alpha_A) \\
&= -6h_{qp}a^2L^{-4}{r_M}^2\left\{\cos 2\alpha_A(-\cos 2\varphi_M) + \sin 2\varphi_M\sin 2\alpha_A\right\} \\
&= 6h_{qp}a^2L^{-4}{r_M}^2\left\{\cos 2\alpha_A(\cos 2\varphi_M) - \sin 2\varphi_M\sin 2\alpha_A\right\} \\
&= 6h_{qp}a^2L^{-4}{r_M}^2\cos 2\left(\alpha_A+\varphi_M\right)
\end{aligned} \tag{A.26}$$

The resulting Taylor series expansion is:

$$\begin{aligned}
h_A(x_M, y_M) \approx h_{qp}\frac{a^2}{L^2}\cos 2\alpha_A &- 2h_{qp}\frac{a^2R_M}{L^3}\frac{r_M}{R_M}\cos(\varphi_M+2\alpha_A) \\
&+ 6h_{qp}\frac{a^2{R_M}^2}{L^4}\frac{{r_M}^2}{{R_M}^2}\cos 2(\varphi_M+\alpha_A)
\end{aligned} \tag{A.27}$$

Evaluating this distortion at the edge of the micropost $r_M = R_M$, we find:

$$h_A(x_M = R_M \cos\varphi_M, y_M = R_M \sin\varphi_M) \approx h_{qp}\frac{a^2}{L^2}\cos 2\alpha_A - 2h_{qp}\frac{a^2 R_M}{L^3}\cos(\varphi_M + 2\alpha_A) + 6h_{qp}\frac{a^2 {R_M}^2}{L^4}\cos 2(\varphi_M + \alpha_A) + H.O.T. \tag{A.28}$$

i.e., at the edge of the micropost, the particle changes the height, the slope and the curvature.

A.1.3. Reflected modes from the post

In order for the contact line at the micropost to remain fixed, some adjustment must be made in the interface shape to undo the disturbance made by A. All of these terms excite decaying induced terms near the post.

$$\begin{aligned} h_{\text{induced at M}} =& - h_{qp}\frac{a^2}{L^2}\cos 2\alpha_A(1 - \ln\frac{r_M}{R_M}) \text{ an induced monopole at micropost} \\ &+ 2h_{qp}\frac{a^2 R_M}{L^3}\frac{R_M}{r_M}\cos(\varphi_M + 2\alpha_A) \text{ an induced dipole at micropost} \\ &+ 6h_{qp}\frac{a^2 {R_M}^2}{L^4}\frac{{R_M}^2}{{r_M}^2}\cos 2(\varphi_M + \alpha_A) \text{ an induced quadrupole at micropost} \\ &+ H.O.T. \end{aligned} \tag{A.29}$$

Consequences near the micropost

These can interact with the micropost-sourced monopole, dipolar and quadrupolar terms. Each mode reflected from the post must be expanded around the particle.

Monopole

The monopole reflected from the micropost changes the curvature near the particle. To evaluate the curvature near A we evaluate:

$$h_{\text{Monopole induced at M}} = -h_{qp}\frac{a^2}{L^2}\cos 2\alpha_A(1 - \ln\frac{r_M}{R_M}) \tag{A.30}$$

Note that ${r_M}^2 = (x_A - L)^2 + {y_A}^2$, evaluate the expression at $r_A = 0$,

$$h_{\text{Monopole induced at M}} = -\frac{h_{qp}}{2}\frac{a^2}{L^2}\cos 2\alpha_A(2 - \ln\frac{(x_A - L)^2 + {y_A}^2}{{R_M}^2}) \tag{A.31}$$

$$h_{\text{Monopole induced at M}}\big|_{r_A=0} = -\frac{h_{qp}}{2}\frac{a^2}{L^2}\cos 2\alpha_A(2 - \ln\frac{L^2}{{R_M}^2}) \tag{A.32}$$

Compute $\nabla h_{\text{Monopole induced at M}}$,

$$\nabla h_{\text{Monopole induced at M}} = h_{qp}\frac{a^2}{L^2}\cos 2\alpha_A\frac{1}{(x_A - L)^2 + {y_A}^2}((x_A - L)\delta_X + y_A\delta_Y) \tag{A.33}$$

$$\mathbf{r}\cdot\nabla h_{\text{Monopole induced at M}}\big|_{0_A} = -h_{qp}\frac{a^3}{L^3}\cos 2\alpha_A\frac{r_A}{a}\cos\varphi \tag{A.34}$$

To find $\nabla\nabla h_{\text{Monopole induced at M}}$, we need to find the second derivatives,

$$\frac{\partial}{\partial x}\Big(\frac{(x_A - L)}{(x_A - L)^2 + {y_A}^2}\Big) = -\frac{2(x_A - L)^2}{((x_A - L)^2 + {y_A}^2)^2} + \frac{1}{(x_A - L)^2 + {y_A}^2} \tag{A.35}$$

$$\frac{\partial}{\partial y}\Big(\frac{(x_A - L)}{(x_A - L)^2 + {y_A}^2}\Big) = -\frac{(x_A - L)2y_A}{((x_A - L)^2 + {y_A}^2)^2} \tag{A.36}$$

$$\begin{aligned}\nabla\nabla h_{\text{Monopole indced at M}} &= h_{qp}\frac{a^2}{L^2}\cos 2\alpha_A\nabla\frac{((x_A - L)\delta_X + y_A\delta_Y)}{(x_A - L)^2 + {y_A}^2}\\ &= h_{qp}\frac{a^2}{L^2}\cos 2\alpha_A(\nabla A_x\delta_X + \nabla A_y\delta_Y)\end{aligned} \tag{A.37}$$

It is convenient to define the variables $\nabla A_x \delta_X$ and $\nabla A_y \delta_Y$

$$\begin{aligned}
\nabla A_x\delta_X &= \frac{\partial}{\partial x}\Big(\frac{(x_A - L)}{(x_A-L)^2+{y_A}^2}\Big)\delta_X\delta_X + \frac{\partial}{\partial y}\Big(\frac{(x_A-L)}{(x_A-L)^2+{y_A}^2}\Big)\delta_X\delta_Y \\
\nabla A_x\delta_X &= \Bigg[-\frac{2(x_A-L)^2}{((x_A-L)^2+{y_A}^2)^2} + \frac{1}{(x_A-L)^2+{y_A}^2}\Bigg]\delta_X\delta_X - \frac{(x_A-L)2y_A}{((x_A-L)^2+{y_A}^2)^2}\delta_X\delta_Y \\
\nabla A_x\delta_X\big|_{0_A} &= -\frac{1}{L^2}\delta_X\delta_X
\end{aligned} \tag{A.38}$$

$$\begin{aligned}
\nabla A_y\delta_y &= \frac{\partial}{\partial x}\frac{(y_A)}{(x_A-L)^2+{y_A}^2}\delta_X\delta_Y + \frac{\partial}{\partial y}\frac{(y_A)}{(x_A-L)^2+{y_A}^2}\delta_Y\delta_Y \\
\nabla A_y\delta_y &= -\frac{(y_A)(x_A-L)2}{((x_A-L)^2+{y_A}^2)^2}\delta_X\delta_Y + -\frac{2(y_A)(y_A)}{((x_A-L)^2+{y_A}^2)^2} + \frac{1}{(x_A-L)^2+{y_A}^2}\delta_Y\delta_Y \\
\nabla A_y\delta_y\big|_{0_A} &= \frac{1}{L^2}\delta_Y\delta_Y
\end{aligned} \tag{A.39}$$

The curvature evaluated at A is:

$$\begin{aligned}
\mathbf{r}\cdot\nabla\nabla h_{\text{Monopolee induced at M}}\big|_{0_A}\cdot\mathbf{r} &= -h_{qp}\frac{a^4}{L^4}\cos 2\alpha_A\frac{{r_A}^2}{a^2}(\cos^2\varphi_A - \sin^2\varphi_A) \\
&= -h_{qp}\frac{a^4}{L^4}\cos 2\alpha_A\frac{{r_A}^2}{a^2}\cos 2\varphi_A
\end{aligned} \tag{A.40}$$

where $\mathbf{r} = r_A\cos\varphi_A + r_A\sin\varphi_A$. The corresponding induced mode at A is:

$$\eta_{reaction\text{ to induced monopole}} = h_{qp}\frac{a^4}{L^4}\cos 2\alpha_A\frac{a^2}{{r_A}^2}\cos 2\varphi_A \tag{A.41}$$

With associated capillary energy:

$$E_{rxn,\text{ ind monopole at post}} = \gamma\pi a^2\frac{2h_{qp}}{{R_M}^2}\left[h_{qp}\frac{a^4}{L^4} - \frac{\Delta c_0 a^2}{4}\cos 2\alpha_A\right] \tag{A.42}$$

Dipole

In this section, we calculate the dipole reflected from the micropost changes the curvature near the particle. Evaluate the changes in height, slope and curvature near the particle.

$$h_{1 \text{ induced at M}} = 2h_{qp}\frac{a^2 R_M}{L^3}\frac{R_M}{r_M}\cos(\varphi_M + 2\alpha_A) \tag{A.43}$$

We define variables ξ and Υ to use in later derivation,

$$\xi = (x_A - L)^2 + {y_A}^2 \tag{A.44}$$

$$\Upsilon = \tan^{-1}\frac{y_A}{x_A - L} \tag{A.45}$$

The partial derivatives of the variables are

$$\frac{\partial\xi}{\partial x} = 2(x_A - L) \tag{A.46}$$

$$\frac{\partial\xi}{\partial y} = 2y_A \tag{A.47}$$

$$\frac{\partial\Upsilon}{\partial x} = \frac{\partial}{\partial x}\Big(\tan^{-1}\frac{y_A}{x_A - L}\Big) = \frac{1}{1+\left(\frac{y_A}{x_A-L}\right)^2}\frac{-y_A}{(x_A - L)^2} = \frac{-y_A}{\xi} \tag{A.48}$$

$$\frac{\partial\Upsilon}{\partial y} = \frac{\partial}{\partial y}\Big(\tan^{-1}\frac{y_A}{x_A - L}\Big) = \frac{1}{1+\left(\frac{y_A}{x_A-L}\right)^2}\frac{1}{(x_A - L)} = \frac{(x_A - L)}{\xi} \tag{A.49}$$

$$\frac{\partial}{\partial x}\left\{(\xi)^{-1/2}\cos(\Upsilon + 2\alpha_A)\right\} = -(\xi)^{-3/2}\left((x_A - L)\cos(\Upsilon + 2\alpha_A) - y_A\sin(\Upsilon + 2\alpha_A)\right) \tag{A.50}$$

$$\frac{\partial}{\partial y}\left\{(\xi)^{-1/2}\cos(\Upsilon + 2\alpha_A)\right\} = -(\xi)^{-3/2}\left(y_A\cos(\Upsilon + 2\alpha_A) + (x_A - L)\sin(\Upsilon + 2\alpha_A)\right) \tag{A.51}$$

Now, the height of the interface near the particle A due to the dipole, Eqn. A.43, becomes,

$$h_{1\text{ induced at M}} = \frac{2h_{qp}a^2R_M}{L^3}\frac{R_M}{(\xi)^{1/2}}\cos(\Upsilon + 2\alpha_A) \tag{A.52}$$

$$h_{1\text{ induced at M}}\big|_{0_A} = \frac{2h_{qp}a^2{R_M}^2}{L^4}\cos 2\alpha_A \tag{A.53}$$

Compute $\nabla h_{1\text{ induced at M near A}}$

$$\begin{aligned}\nabla h_{1\text{ induced at M near A}} = &-\frac{2h_{qp}a^2{R_M}^2}{L^3}(\xi)^{-3/2}\left((x_A - L)\cos(\Upsilon + 2\alpha_A) - y_A\sin(\Upsilon + 2\alpha_A)\right)\delta_X \\ &-\frac{2h_{qp}a^2{R_M}^2}{L^3}(\xi)^{-3/2}(y_A\cos(\Upsilon + 2\alpha_A) + (x_A - L)\sin(\Upsilon + 2\alpha_A))\delta_Y\end{aligned} \tag{A.54}$$

Upon evaluation at $x_A = y_A = 0$ this reduces to,

$$\nabla h_{1\text{ induced at M near A}}\big|_{0_A} = \frac{2h_{qp}a^2{R_M}^2}{L^5}\left(\cos 2\alpha_A\delta_X + \sin 2\alpha_A\delta_Y\right) \tag{A.55}$$

Note that $\mathbf{r_A} = r_A\cos\varphi_A\delta_X + r_A\sin\varphi_A\delta_Y$,

$$\mathbf{r_A}\cdot\nabla h_{1\text{ induced at M near A}}\big|_{0_A} = \frac{2h_{qp}a^3{R_M}^2}{L^5}\frac{r_A}{a}\left(\cos\varphi_A\cos 2\alpha_A + \sin\varphi_A\sin 2\alpha_A\right) \tag{A.56}$$

$$\mathbf{r_A}\cdot\nabla h_{1\text{ induced at M near A}}\big|_{0_A} = \frac{2h_{qp}a^3{R_M}^2}{L^5}\frac{r_A}{a}\cos(\varphi_A - 2\alpha_A) \tag{A.57}$$

Then, let's compute $\nabla\nabla h_{1\text{ induced at M near A}}$

$$\begin{aligned}\nabla\nabla h_{1\text{ induced at M near A}} &= A_0\nabla\Big((\xi)^{-3/2}(((x_A - L)\cos(\Upsilon + 2\alpha_A) - y_A\sin(\Upsilon + 2\alpha_A))\,\delta_X \\ &\quad + (y_A\cos(\Upsilon + 2\alpha_A) + (x_A - L)\sin(\Upsilon + 2\alpha_A))\,\delta_Y)\Big) \\ &= A_0\nabla\left(T_1\delta_X + T_2\delta_Y\right)\end{aligned} \tag{A.58}$$

where $A_0 = -\frac{2h_{gp}a^2{R_M}^2}{L^3}$. It is convenient to define variable T_1 and T_2,

$$\begin{aligned}
\frac{\partial T_1}{\partial x} &= \frac{\partial}{\partial x}(\xi)^{-3/2}\left((x_A - L)\cos(\Upsilon + 2\alpha_A) - y_A\sin(\Upsilon + 2\alpha_A)\right) \\
&= -3(\xi)^{-5/2}(x_A - L)\left((x_A - L)\cos(\Upsilon + 2\alpha_A) - y_A\sin(\Upsilon + 2\alpha_A)\right) \\
&\quad + (\xi)^{-5/2}\left(\xi\cos(\Upsilon + 2\alpha_A) + (x_A - L)y_A\sin(\Upsilon + 2\alpha_A) + {y_A}^2\cos(\Upsilon + 2\alpha_A)\right) \\
&= (\xi)^{-5/2}((-3(x_A - L)^2 + \xi + {y_A}^2)\cos(\Upsilon + 2\alpha_A) + 4y_A(x_A - L)\sin(\Upsilon + 2\alpha_A))
\end{aligned} \tag{A.59}$$

$$\begin{aligned}
\frac{\partial T_1}{\partial y} &= \frac{\partial}{\partial y}(\xi)^{-3/2}\left((x_A - L)\cos(\Upsilon + 2\alpha_A) - y_A\sin(\Upsilon + 2\alpha_A)\right) \\
&= -3(\xi)^{-5/2}y_A\left((x_A - L)\cos(\Upsilon + 2\alpha_A) - y_A\sin(\Upsilon + 2\alpha_A)\right) \\
&\quad + (\xi)^{-5/2}\Big(-(x_A - L)^2\sin(\Upsilon + 2\alpha_A) - \xi\sin(\Upsilon + 2\alpha_A) - y_A\,(x_A - L)\cos(\Upsilon + 2\alpha_A)\Big) \\
&= (\xi)^{-5/2}((3{y_A}^2 - (x_A - L)^2 - \xi)\sin(\Upsilon + 2\alpha_A) - 4y_A(x_A - L)\cos(\Upsilon + 2\alpha_A))
\end{aligned} \tag{A.60}$$

$$\begin{aligned}
\frac{\partial T_2}{\partial x} &= \frac{\partial}{\partial x}(\xi)^{-3/2}\left[y_A\cos(\Upsilon + 2\alpha_A) + (x_A - L)\sin(\Upsilon + 2\alpha_A)\right] \\
&= -3(\xi)^{-5/2}(x_A - L)\left[y_A\cos(\Upsilon + 2\alpha_A) + (x_A - L)\sin(\Upsilon + 2\alpha_A)\right] \\
&\quad + (\xi)^{-5/2}\left[{y_A}^2\sin(\Upsilon + 2\alpha_A) + \xi\sin(\Upsilon + 2\alpha_A) - y_A\,(x_A - L)\cos(\Upsilon + 2\alpha_A)\right] \\
&= (\xi)^{-5/2}(({y_A}^2 - 3(x_A - L)^2 + \xi)\sin(\Upsilon + 2\alpha_A) - 4y_A(x_A - L)\cos(\Upsilon + 2\alpha_A))
\end{aligned} \tag{A.61}$$

$$
\begin{aligned}
\frac{\partial T_2}{\partial y} &= \frac{\partial}{\partial y}(\xi)^{-3/2}\left[y_A\cos(\Upsilon+2\alpha_A)+(x_A-L)\sin(\Upsilon+2\alpha_A)\right] \\
&= -3(\xi)^{-5/2}y_A\left[y_A\cos(\Upsilon+2\alpha_A)+(x_A-L)\sin(\Upsilon+2\alpha_A)\right] \\
&\quad+(\xi)^{-5/2}\left[\xi\cos(\Upsilon+2\alpha_A)-y_A\,(x_A-L)\sin(\Upsilon+2\alpha_A)+(x_A-L)^2\cos(\Upsilon+2\alpha_A)\right] \\
&= (\xi)^{-5/2}(-4y_A(x_A-L)\sin(\Upsilon+2\alpha_A)-({3y_A}^2-\xi-(x_A-L)^2)\cos(\Upsilon+2\alpha_A))
\end{aligned}
\tag{A.62}
$$

Evaluating at the particle,

$$
\left.\frac{\partial T_1}{\partial x}\right|_{0_A} = \frac{-2}{L^3}\cos 2\alpha_A \tag{A.63}
$$

$$
\left.\frac{\partial T_1}{\partial y}\right|_{0_A} = -\frac{2}{L^3}\sin 2\alpha_A \tag{A.64}
$$

$$
\left.\frac{\partial T_2}{\partial x}\right|_{0_A} = -\frac{2}{L^3}\sin 2\alpha_A \tag{A.65}
$$

$$
\left.\frac{\partial T_2}{\partial y}\right|_{0_A} = \frac{2}{L^3}\cos 2\alpha_A \tag{A.66}
$$

Substituting:

$$
\begin{aligned}
\mathbf{r}\cdot\nabla\nabla h\cdot\mathbf{r} &= -\frac{2h_{qp}a^2{R_M}^2}{L^3}\left[\frac{-2}{L^3}\cos 2\alpha_A {r_A}^2(\cos^2\varphi_A-\sin^2\varphi_A)-\right. \\
&\qquad\left.-\frac{2}{L^3}\sin 2\alpha_A {r_A}^2\sin\varphi_A\cos\varphi_A-\frac{2}{L^3}\sin 2\alpha_A {r_A}^2\sin\varphi_A\cos\varphi_A\right] \\
&= -\frac{2h_{qp}a^2{R_M}^2}{L^3}\left[\frac{-2{r_A}^2}{L^3}\cos 2\alpha_A\cos 2\varphi_A-\frac{4{r_A}^2}{L^3}\sin 2\alpha_A\sin\varphi_A\cos\varphi_A\right] \\
&= \frac{2h_{qp}a^2{R_M}^2}{L^3}\left[\frac{2{r_A}^2}{L^3}(\sin 2\alpha_A\sin 2\varphi_A+\cos 2\alpha\cos 2\varphi_A)\right] \\
&= \frac{4h_{qp}a^4{R_M}^2}{L^6}\cos 2(\varphi_A-\alpha_A)\frac{{r_A}^2}{a^2}
\end{aligned}
\tag{A.67}
$$

They are the same as the angles on the particle-sourced distortion at A. The corresponding induced mode at the particle is:

$$
\eta_{1\text{ induced at M near A}} = -\frac{4h_{qp}a^4{R_M}^2}{L^6}\cos 2(\varphi_A-\alpha_A)\frac{a^2}{r^2}
$$

The energy should have the form:

$$E_{Dipole-particle} = \gamma\pi a^2 \frac{8h_{qp}a^2}{{R_M}^4}\left[h_{qp}\frac{{R_M}^6}{L^6} - \frac{\Delta c_0 a^2}{4}\cos\alpha_A\right] \tag{A.68}$$

Quadrupole

Expansion of the quadrupolar term reflected from the micropost to A

$$h_{2\ induced\ \text{from A on M}} = -6h_{qp}\frac{a^2{R_M}^2}{L^4}\frac{{R_M}^2}{{r_M}^2}\cos 2(\varphi_M + \alpha_A) \tag{A.69}$$

$$h_{2\ induced\ \text{from A on M expanded near A}} = -\left(6h_{qp}\frac{a^2{R_M}^2}{L^4}\right)\frac{{R_M}^2a^2}{L^4}\frac{{r_A}^2}{a^2}\cos 2(\varphi_A - \alpha_A) \tag{A.70}$$

$$\begin{aligned} h_{\text{induced term from (2 } induced \text{ from A on M expanded near A)}} &= h_{2,refl} \\ &= +\left(6h_{qp}\frac{a^2{R_M}^2}{L^4}\right)\left(6\frac{{R_M}^2a^2}{L^4}\right)\frac{a^2}{{r_A}^2}\cos 2(\varphi_A - \alpha_A) \end{aligned} \tag{A.71}$$

$$E = h_{2,refl} = +\gamma\pi a^2\left(6h_{qp}\frac{a^2{R_M}^2}{L^4}\right)\left(6\frac{{R_M}^2a^2}{L^4}\right)\left[h_{qp} - \frac{\Delta c_0 a^2}{4}\cos 2\alpha_A\right] \tag{A.72}$$

This has the same sign as the particle sourced term and interacts similarly either with the particle directly or with the host curvature. The picture that is emerging is:

$$E_{including\ reflection} = E_{\text{cap curv attraction}} + E_{2,ref,\Delta c_0} + E_{2,ref,h_A} + (E_{2,ref,2,ref}) + \sum_{other} E \tag{A.73}$$

$$
\begin{aligned}
E_{including\ reflection} = & -\gamma\pi h_{qp}\frac{a^2\Delta c_0}{2}\cos 2(\alpha_A) \\
& + \gamma\pi\left[h_{qp} - \frac{\Delta c_0 a^2}{4}\cos 2\alpha_A\right]\left(2h_{qp}\left(\frac{a}{R_M}\right)^4\right)\left(\frac{R_M}{L}\right)^4 \\
& \text{(reaction to reflected monopole at post)} \\
& + \gamma\pi\left[h_{qp} - \frac{\Delta c_0 a^2}{4}\cos 2\alpha_A\right]\left(2h_{qp}\left(\frac{a}{R_M}\right)^4\right)(2^2)\left(\frac{R_M}{L}\right)^6 \\
& \text{(reaction to reflected dipole at post)} \\
& + \gamma\pi\left[h_{qp} - \frac{\Delta c_0 a^2}{4}\cos 2\alpha_A\right]\left(2h_{qp}\left(\frac{a}{R_M}\right)^4\right)(2^2 3^2)\left(\frac{R_M}{L}\right)^8 \\
& \text{(reaction to reflected quadrupole at post)} \\
& + \sum_{other} E
\end{aligned}
\tag{A.74}
$$

The last term, $\sum_{other} E$, has contributions from the cross terms and self terms.

$$
\begin{aligned}
& \text{cross terms (which go as } \left(\frac{a}{R_M}\right)^8\text{):} \\
& \quad + \text{reflected monopole and reflected dipole } \sim \left(\frac{R_M}{L}\right)^{10} \\
& \quad + \text{reflected monopole and reflected quadrupole } \sim \left(\frac{R_M}{L}\right)^{12} \\
& \quad + \text{reflected dipole and reflected quadrupole) } \sim \left(\frac{R_M}{L}\right)^{14} \\
& \text{self terms (which go as } \left(\frac{a}{R_M}\right)^8\text{):} \\
& \quad + \text{reflected monopole self } \sim \left(\frac{R_M}{L}\right)^{8} \\
& \quad + \text{reflected dipole self } \sim \left(\frac{R_M}{L}\right)^{12} \\
& \quad + \text{reflected quadrupole self } \sim \left(\frac{R_M}{L}\right)^{16}
\end{aligned}
$$

Each reflected mode could contribute a change of height, slope and quadrupole as it is expanded near the particle. The addition of many such reflected terms could set equilibrium locations near the post. Analysis of the quadrupolar term alone would fix an equilibrium location very close to the post. The addition of many higher order terms could perturb this location.

A.2. Deformation around a large microdisk

In addition to Fig. 3a) in the main text, here we present the interferogram of another microdisk ($2a = 150\mu m$). Figure A.2 shows random puckering near the particle and only higher order modes evident at $170\mu m$ from particle center.

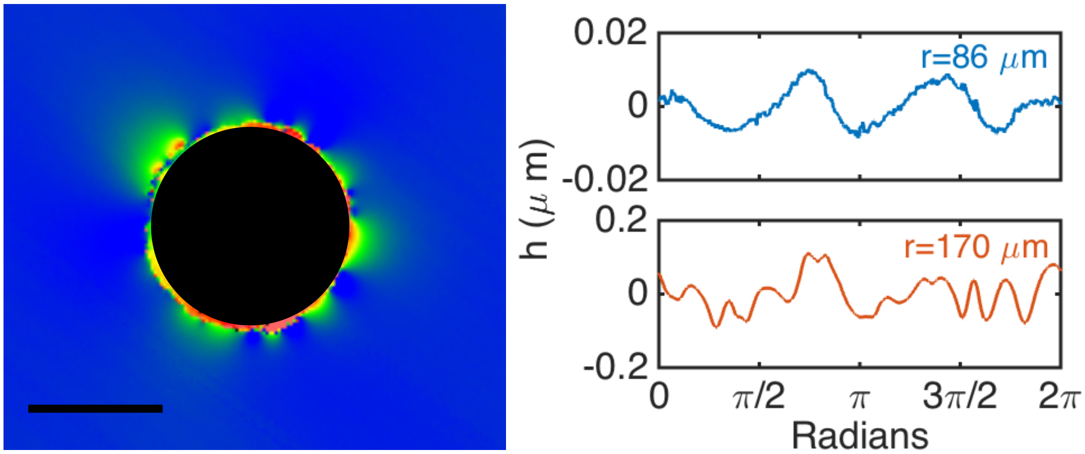

Figure A.2: Interferogram of a microdisk ($2a = 150\mu m$). Interferogram showing Top: hexapolar undulation of interface height along a circle of radius 170 μm from particle center. Bottom: undulated interface height along a circle of radius 86 μm from particle center.

A.3. Simulated studies on curvature capillary interactions with higher order modes

We extend our study on higher order mode interaction with curvature field by computing the capillary energy of a 25 μm diameter disk on a 57 μm diameter micropost. In this problem, we consider the disk particle carries two modes of with its undulated contact line: hexapole (HP) and quadrupole (QP) . We assume these modes have fixed relative orientation and we consider the case where the rise axis of the QP coincides with one rise point on the HP, as depicted in the Figure A.3. We plot energy landscapes for this particle in several orientations with respect to the post. First, we consider an orientation where the QP is attractive and the HP is repulsive. In this configuration, the two modes will frustrate each other when they are both significant. By assigning h_2 and h_3 with reasonable values, we calculate the capillary energy of the microdisk migration from $L_0 = 300\mu m$ to $L_0 = 41.5\mu m$, the center to center distance of a disk at the edge of a $57\mu m$ diameter post (Figure A.3a)). The capillary energy first decreases as the particle approaches the micropost, indicating the far field QP interaction. However, as the repulsive HP grows in importance, an energy well near $L_0 = 96.5\mu m$ defines the particle's equilibrium location. A second example trajectory is shown in Fig. A.3b) for this particle oriented so that both QP and HP are repulsive; the particle will migrate away from the micropost to minimize the energy of the system.

These simple examples demonstrate how a particle with different modes interacts with the curvature field when there are strong energy barriers to particle rotation owing to the rugged contact line. Figure A.3c) shows the energy barriers to rotation at two L_0 locations on the curved interface as a function of α_2 for this example particle, noting that $\alpha_2 = 0°, 180°$ or $-180°$ are the preferred QP alignment. The dotted line far from the post ($L_0 = 300\ \mu m$) resembles a $\cos 2\alpha_2$ which suggests the strong quadrupole interaction in the far field. However, close to the post, the blue line, ($L_0 = 96.5\ \mu m$), the energy barriers are more significant and the angular dependence is more complex. This significant rotational barrier in the high curvature region prevents particles from finding their global minimum, which is why we have a zoo of observations of particles equilibrating at various locations, repelled from high curvature region, or migrating to the post. In the main text, we present data that supports this interpretation for a particle that is repelled from near the post, rotates in the far field, and follows by attraction to the micropost following a quadrupolar dominated trajectory.

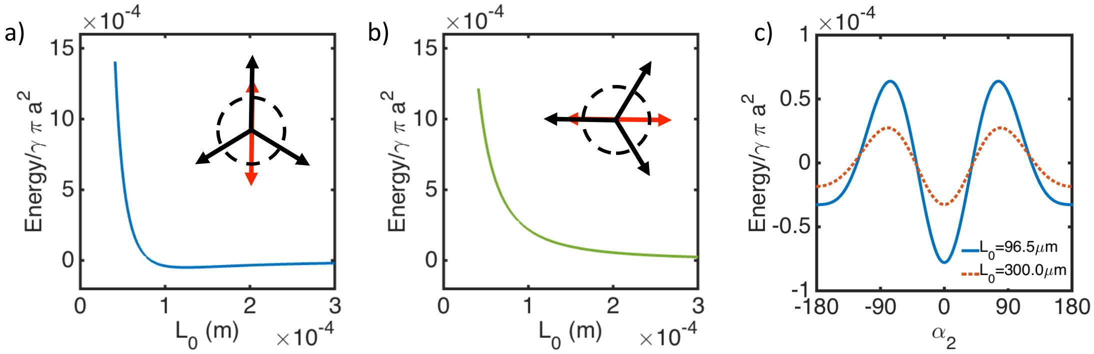

Figure A.3: Curvature capillary energy of a 25 μm diameter disk with hexapolar (HP) and quadrupolar (QP) modes. Simulated trajectory of a disk with hexapole ($h_2 = 300$ nm) and quadrupole ($h_3 = 2000$ nm) deformation. a) Energy profile for a particle trajectory with QP aligned and misaligned HP on a curved interface. b) Energy landscape of a trajectory for misaligned HP and QP. In a) and b), the micropost (not shown) is located directly above the particle in the schematic. c) Energy profile as a function of QP alignment (α_2) with respect to the principal curvature of the interface at $L_0 = 96.5$ μm and $L_0 = 300$ μm.

APPENDIX B

B.1. Data analysis

Data analysis plays an important role in my research for the past five years. In this section focuses on how the I use particle tracking to analyze experimental data. The steps listed here are the general steps I took in my data analysis for all of the projects in previous chapters. Parameters may vary slightly in order to obtain the most accurate particle position.

B.2. Particle tracking

Experiments are taken under an upright microscope (Zeiss M1m) in either reflective or transmitted mode. Particle trajectories are recorded using a high resolution camera in a black and white setting at a certain frame rate per second. After converting the raw video into a readable format, e.g., avi, png, tif..., I import the video or the image sequence into ImageJ. Selecting IMAGE-TYPE-8-bit, I convert the video into 8-bit. Here, in ANALYZE tab, I enter the pixel to unit conversion in SET SCALE such that my final output will have the unit of microns. In the experiments where micropost is present, I use OVAL to fit the edges of the micropost to find the center location, which will be used later to calculate the separation distance. In order to use the ANALYZE PARTICLE mode in the software, the video needs to be adjusted to have a better contrast between the particle and the background. This is done by selecting IMAGE-ADJUST-THRESHOLD and manually changing the min/max values so that the video has minimal background noise and still maintains a strong contrast between the particles and its surroundings. Next, the video is converted into Binary by selecting PROCESS-BINARY-MAKE BINARY. Based on the quality of the video, there are a few tabs under BINARY might come useful. Under ANALYZE-SET MEASUREMENT, we could select the quantities that we want to measure. Lastly, we run ImageJ to analyze the particle by clicking ANALYZE-ANALYZE PARTICLE and entering the range of particle size and circularity.

B.3. Matlab

This section describes the steps I take using Matlab to analyze data. Once I obtain the particle location (x, y) at each frame from particle tracking, I compute the separation distance (L) between the micropost and particle at each time time. To simplify the analysis, I fit this time and separation distance with a polynomial using *polyfit* to get $L(t)$. The degree of polynomial varies from trajectory to trajectory; however, the general rule is that the fit captures the trend without overfitting the data. Next, I evaluate the distance at each time step from polynomial using *polyval*. From the polynomial $L(t)$, I can calculate the local deviatoric curvature at each frame t. The velocity is computed by finding the derivative of $L(t)$ using *polyder* and evaluating at each time frame, $v(t)$. Finally, with velocity $(v(t))$, distance $(L(t))$, and drag coefficient (C_D), I use Stokes law by summing energy dissipated at each time step to find the total energy dissipated along a path.

BIBLIOGRAPHY

[1] S. C. Glotzer, M. J. Solomon, Anisotropy of building blocks and their assembly into complex structures, Nat. Mater. 6 (7) (2007) 557–562.

[2] F. Romano, F. Sciortino, Colloidal self-assembly: Patchy from the bottom up, Nat. Mater. 10 (3) (2011) 171–173.

[3] P. F. Damasceno, M. Engel, S. C. Glotzer, Predictive self-assembly of polyhedra into complex structures, Science 337 (6093) (2012) 453–457.

[4] E. G. Teich, G. van Anders, D. Klotsa, J. Dshemuchadse, S. C. Glotzer, Clusters of polyhedra in spherical confinement, Proc. Natl. Acad. Sci. USA 113 (6) (2016) E669–E678.

[5] S. Sacanna, W. T. M. Irvine, P. M. Chaikin, D. J. Pine, Lock and key colloids, Nature 464 (7288) (2010) 575–578.

[6] Y. Wang, Y. Wang, X. Zheng, É. Ducrot, M.-G. Lee, G.-R. Yi, M. Weck, D. J. Pine, Synthetic strategies toward dna-coated colloids that crystallize, J. Am. Chem. Soc. 137 (33) (2015) 10760–10766.

[7] W. B. Rogers, W. M. Shih, V. N. Manoharan, Using dna to program the self-assembly of colloidal nanoparticles and microparticles, Nat Rev Mater 1 (2016) 16008.

[8] M.-P. Valignat, O. Theodoly, J. C. Crocker, W. B. Russel, P. M. Chaikin, Reversible self-assembly and directed assembly of dna-linked micrometer-sized colloids, Proc. Natl. Acad. Sci. USA 102 (12) (2005) 4225–4229.

[9] N. Geerts, E. Eiser, Dna-functionalized colloids: Physical properties and applications, Soft Matter 6 (2010) 4647–4660.

[10] A. J. Kim, R. Scarlett, P. L. Biancaniello, T. Sinno, J. C. Crocker, Probing interfacial equilibration in microsphere crystals formed by dna-directed assembly, Nat. Mater. 8 (1) (2009) 52–55.

[11] A. B. Pawar, I. Kretzschmar, Patchy particles by glancing angle deposition, Langmuir 24 (2) (2008) 355–358.

[12] A. B. Pawar, I. Kretzschmar, Multifunctional patchy particles by glancing angle deposition, Langmuir 25 (16) (2009) 9057–9063.

[13] B. J. Park, D. Lee, Configuration of nonspherical amphiphilic particles at a fluid-fluid interface, Soft Matter 8 (2012) 7690–7698.

[14] B. J. Park, C.-H. Choi, S.-M. Kang, K. E. Tettey, C.-S. Lee, D. Lee, Geometrically and chemically anisotropic particles at an oil-water interface, Soft Matter 9 (2013) 3383–3388.

[15] S. L. Biswal, A. P. Gast, Rotational dynamics of semiflexible paramagnetic particle chains, Phys. Rev. E 69 (2004) 041406.

[16] S. L. Biswal, A. P. Gast, Mechanics of semiflexible chains formed by poly(ethylene glycol)-linked paramagnetic particles, Phys. Rev. E 68 (2003) 021402.

[17] P. Liu, J. W. J. de Folter, A. V. Petukhov, A. P. Philipse, Reconfigurable assembly of superparamagnetic colloids confined in thermo-reversible microtubes, Soft Matter 11 (2015) 6201–6211.

[18] E. M. Furst, A. P. Gast, Dynamics and lateral interactions of dipolar chains, Phys. Rev. E 62 (2000) 6916–6925.

[19] P. Dommersnes, Z. Rozynek, A. Mikkelsen, R. Castberg, K. Kjerstad, K. Hersvik, J. Otto Fossum, Active structuring of colloidal armour on liquid drops, Nat. Commun. 4 (2013) 2066.

[20] M. Cavallaro, L. Botto, E. P. Lewandowski, M. Wang, K. J. Stebe, Curvature-driven capillary migration and assembly of rod-like particles, Proc. Natl. Acad. Sci. USA 108 (52) (2011) 20923–20928.

[21] N. Li, N. Sharifi-Mood, F. Tu, D. Lee, R. Radhakrishnan, T. Baumgart, K. J. Stebe, Curvature-driven migration of colloids on tense lipid bilayers, Langmuir 33 (2) (2017) 600–610.

[22] Y. Luo, F. Serra, K. J. Stebe, Experimental realization of the "lock-and-key" mechanism in liquid crystals, Soft Matter 12 (28) (2016) 6027–6032.

[23] I. B. Liu, M. A. Gharbi, V. L. Ngo, R. D. Kamien, S. Yang, K. J. Stebe, Elastocapillary interactions on nematic films, Proc. Natl. Acad. Sci. USA 112 (20) (2015) 6336–6340.

[24] M. Cavallaro, M. A. Gharbi, D. A. Beller, S. Čopar, Z. Shi, T. Baumgart, S. Yang, R. D. Kamien, K. J. Stebe, Exploiting imperfections in the bulk to direct assembly of surface colloids, Proc. Natl. Acad. Sci. USA 110 (47) (2013) 18804–18808.

[25] E. Lee, Y. Xia, R. C. Ferrier, H.-N. Kim, M. A. Gharbi, K. J. Stebe, R. D. Kamien, R. J. Composto, S. Yang, Fine golden rings: Tunable surface plasmon resonance from assembled nanorods in topological defects of liquid crystals, Adv. Mater. 28 (14) (2016) 2731–2736.

[26] S. U. Pickering, Cxcvi.-emulsions, J. Chem. Soc. 91 (0) (1907) 2001–2021.

[27] S. Crossley, J. Faria, M. Shen, D. E. Resasco, Solid nanoparticles that catalyze biofuel upgrade reactions at the water/oil interface, Science 327 (5961) (2009) 68–72.

[28] F. Tu, D. Lee, Shape-changing and amphiphilicity-reversing janus particles with ph-responsive surfactant properties, J. Am. Chem. Soc. 136 (28) (2014) 9999–10006, pMID: 24791976.

[29] P. J. Yunker, M. Gratale, M. A. Lohr, T. Still, T. C. Lubensky, A. G. Yodh, Influence of particle shape on bending rigidity of colloidal monolayer membranes and particle deposition during droplet evaporation in confined geometries, Phys. Rev. Lett. 108 (2012) 228303.

[30] P. Pieranski, Two-dimensional interfacial colloidal crystals, Phys. Rev. Lett. 45 (1980) 569–572.

[31] D. M. Hall, I. R. Bruss, J. R. Barone, G. M. Grason, Morphology selection via geometric frustration in chiral filament bundles, Nat. Mater. 15 (2016) 727–732.

[32] A. D. Dinsmore, M. F. Hsu, M. G. Nikolaides, M. Marquez, A. R. Bausch, D. A. Weitz, Colloidosomes: Selectively permeable capsules composed of colloidal particles, Science 298 (5595) (2002) 1006–1009.

[33] W. T. M. Irvine, V. Vitelli, P. M. Chaikin, Pleats in crystals on curved surfaces, Nature 468 (7326) (2010) 947–951.

[34] M. E. Leunissen, A. van Blaaderen, A. D. Hollingsworth, M. T. Sullivan, P. M. Chaikin, Electrostatics at the oil-water interface, stability, and order in emulsions and colloids, Proc. Natl. Acad. Sci. USA 104 (8) (2007) 2585–2590.

[35] M. E. Leunissen, C. G. Christova, A.-P. Hynninen, C. P. Royall, A. I. Campbell, A. Imhof, M. Dijkstra, R. van Roij, A. van Blaaderen, Ionic colloidal crystals of oppositely charged particles, Nature 437 (7056) (2005) 235–240.

[36] R. Aveyard, B. P. Binks, J. H. Clint, P. D. I. Fletcher, T. S. Horozov, B. Neumann, V. N. Paunov, J. Annesley, S. W. Botchway, D. Nees, A. W. Parker, A. D. Ward, A. N. Burgess, Measurement of long-range repulsive forces between charged particles at an oil-water interface, Phys. Rev. Lett. 88 (2002) 246102.

[37] F. Ghezzi, J. Earnshaw, Formation of meso-structures in colloidal monolayers, J. Phys. Condens. Matter 9 (1997) L517–L523.

[38] R. McGorty, J. Fung, D. Kaz, V. N. Manoharan, Colloidal self-assembly at an interface, Mater. Today 13 (6) (2010) 34 – 42.

[39] P. A. Kralchevsky, K. Nagayama, Capillary interactions between particles bound to interfaces, liquid films and biomembranes, Adv. Colloid Interface Sci. 85 (2–3) (2000) 145 – 192.

[40] D. L. Hu, B. Chan, J. W. M. Bush, The hydrodynamics of water strider locomotion, Nature 424 (6949) (2003) 663–666.

[41] D. Vella, L. Mahadevan, The “Cheerios effect”, Am. J. Phys. 73 (9) (2005) 817–825.

[42] D. Chan, J. Henry, L. White, The interaction of colloidal particles collected at fluid interfaces, J. Colloid Interface Sci. 79 (2) (1981) 410 – 418.

[43] D.-G. Lee, P. Cicuta, D. Vella, Self-assembly of repulsive interfacial particles via collective sinking, Soft Matter 13 (1) (2017) 212–221.

[44] J. Voise, M. Schindler, J. Casas, E. Raphaël, Capillary-based static self-assembly in higher organisms, J. R. Soc. Interface 8 (62) (2011) 1357–1366.

[45] D. L. Hu, J. W. M. Bush, Meniscus-climbing insects, Nature 437 (7059) (2005) 733–736.

[46] N. Bowden, A. Terfort, J. Carbeck, G. M. Whitesides, Self-assembly of mesoscale objects into ordered two-dimensional arrays, Science 276 (5310) (1997) 233–235.

[47] N. Bowden, I. S. Choi, B. A. Grzybowski, G. M. Whitesides, Mesoscale self-assembly of hexagonal plates using lateral capillary forces: synthesis using the "capillary bond", J. Am. Chem. Soc. 121 (23) (1999) 5373–5391.

[48] N. Bowden, F. Arias, T. Deng, G. M. Whitesides, Self-assembly of microscale objects at a liquid/liquid interface through lateral capillary forces, Langmuir 17 (5) (2001) 1757–1765.

[49] N. Sharifi-Mood, I. B. Liu, K. J. Stebe, Capillary interactions on fluid interfaces: Opportunities for directed assembly, in: C. N. Likos, F. Sciortino, P. Ziherl (Eds.), Soft Matter Self-Assembly, Vol. 193 of Proceedings of the International School of Physics "Enrico Fermi", IOS Press, Varenna on Lake Como, Villa Monastero, 2016, pp. 165–215.

[50] C. Zeng, F. Brau, B. Davidovitch, A. D. Dinsmore, Capillary interactions among spherical particles at curved liquid interfaces, Soft Matter 8 (2012) 8582–8594.

[51] J. Guzowski, M. Tasinkevych, S. Dietrich, Capillary interactions in pickering emulsions, Phys. Rev. E 84 (3) (2011) 031401.

[52] C. Blanc, D. Fedorenko, M. Gross, M. In, M. Abkarian, M. A. Gharbi, J.-B. Fournier, P. Galatola, M. Nobili, Capillary force on a micrometric sphere trapped at a fluid interface exhibiting arbitrary curvature gradients, Phys. Rev. Lett. 111 (2013) 058302.

[53] D. M. Kaz, R. McGorty, M. Mani, M. P. Brenner, V. N. Manoharan, Physical ageing of the contact line on colloidal particles at liquid interfaces, Nat. Mater. 11 (2) (2012) 138–142.

[54] G. Boniello, C. Blanc, D. Fedorenko, M. Medfai, N. B. Mbarek, M. In, M. Gross, A. Stocco, M. Nobili, Brownian diffusion of a partially wetted colloid, Nat. Mater. 14 (9) (2015) 908–911.

[55] A. Wang, R. McGorty, D. M. Kaz, V. N. Manoharan, Contact-line pinning controls how quickly colloidal particles equilibrate with liquid interfaces, Soft Matter 12 (43) (2016) 8958–8967.

[56] L. Chen, L.-O. Heim, D. S. Golovko, E. Bonaccurso, Snap-in dynamics of single particles to water drops, Appl. Phys. Lett. 101 (3) (2012) 031601.

[57] C. E. Colosqui, J. F. Morris, J. Koplik, Colloidal adsorption at fluid interfaces: Regime crossover from fast relaxation to physical aging, Phys. Rev. Lett. 111 (2013) 028302.

[58] P. Singh, D. D. Joseph, S. K. Gurupatham, B. Dalal, S. Nudurupati, Spontaneous dispersion of particles on liquid surfaces, Proc. Natl. Acad. Sci. USA 106 (47) (2009) 19761–19764.

[59] R. G. Cox, The dynamics of the spreading of liquids on a solid surface. Part 1.Viscous flow, J. Fluid Mech. 168 (1986) 169–194.

[60] T. Blake, J. Haynes, Kinetics of liquidliquid displacement, J. Colloid Interface Sci. 30 (3) (1969) 421 – 423.

[61] D. Stamou, C. Duschl, D. Johannsmann, Long-range attraction between colloidal spheres at the air-water interface: The consequence of an irregular meniscus, Phys. Rev. E 62 (2000) 5263–5272.

[62] K. D. Danov, P. A. Kralchevsky, B. N. Naydenov, G. Brenn, Interactions between particles with an undulated contact line at a fluid interface: Capillary multipoles of arbitrary order, J. Colloid Interface Sci. 287 (1) (2005) 121 – 134.

[63] E. P. Lewandowski, C. M., L. Botto, J. C. Bernate, V. Garbin, K. J. Stebe, Orientation and self-assembly of cylindrical particles by anisotropic capillary interactions, Langmuir 26 (19) (2010) 15142–15154.

[64] L. Botto, E. P. Lewandowski, M. Cavallaro, K. J. Stebe, Capillary interactions between anisotropic particles, Soft Matter 8 (2012) 9957–9971.

[65] L. Botto, L. Yao, R. L. Leheny, K. J. Stebe, Capillary bond between rod-like particles and the micromechanics of particle-laden interfaces, Soft Matter 8 (2012) 4971–4979.

[66] J. C. Loudet, B. Pouligny, How do mosquito eggs self-assemble on the water surface?, Eur. Phys. J. E Soft Matter 34 (8) (2011) 76.

[67] A. Wang, W. B. Rogers, V. N. Manoharan, Effects of contact-line pinning on the adsorption of nonspherical colloids at liquid interfaces, In progress.

[68] J. C. Loudet, A. M. Alsayed, J. Zhang, A. G. Yodh, Capillary interactions between anisotropic colloidal particles, Phys. Rev. Lett. 94 (2005) 018301.

[69] J. C. Loudet, A. G. Yodh, B. Pouligny, Wetting and contact lines of micrometer-sized ellipsoids, Phys. Rev. Lett. 97 (2006) 018304.

[70] E. P. Lewandowski, J. A. Bernate, A. Tseng, P. C. Searson, K. J. Stebe, Oriented assembly of anisotropic particles by capillary interactions, Soft Matter 5 (2009) 886–890.

[71] E. L. Sharp, H. Al-Shehri, T. S. Horozov, S. D. Stoyanov, V. N. Paunov, Adsorption of shape-anisotropic and porous particles at the air-water and the decane-water interface studied by the gel trapping technique, RSC Adv. 4 (5) (2014) 2205–2213.

[72] Z. Zhang, P. Pfleiderer, A. B. Schofield, C. Clasen, J. Vermant, Synthesis and directed self-assembly of patterned anisometric polymeric particles, J. Am. Chem. Soc. 133 (3) (2011) 392–395.

[73] H. Lehle, E. Noruzifar, M. Oettel, Ellipsoidal particles at fluid interfaces, Eur. Phys. J. E Soft Matter 26 (1-2) (2008) 151–160.

[74] G. Soligno, M. Dijkstra, R. van Roij, Self-assembly of cubes into 2D hexagonal and honeycomb lattices by hexapolar capillary interactions, Phys. Rev. Lett. 116 (2016) 258001.

[75] J. Lucassen, Capillary forces between solid particles in fluid interfaces, Colloids and Surfaces 65 (2–3) (1992) 131 – 137.

[76] L. Yao, L. Botto, M. Cavallaro, Jr, B. J. Bleier, V. Garbin, K. J. Stebe, Near field capillary repulsion, Soft Matter 9 (2013) 779–786.

[77] S. Kim, S. J. Karrila, Microhydrodynamics: Principles and selected applications, Dover Publications, 2005.

[78] J. Happel, H. Brenner, Low Reynolds number hydrodynamics, Springer, 1983.

[79] G. B. Arfken, H. J. Weber, F. E. Harris, Mathematical methods for physicists, Academic Press, Waltham, Massachusett, USA, 2005.

[80] S. Dasgupta, M. Katava, M. Faraj, T. Auth, G. Gompper, Capillary assembly of microscale ellipsoidal, cuboidal, and spherical particles at interfaces, Langmuir 30 (40) (2014) 11873–11882.

[81] J. C. Loudet, B. Pouligny, Self-assembled capillary arrows, EPL 85 (2) (2009) 28003.

[82] E. A. van Nierop, M. A. Stijnman, S. Hilgenfeldt, Shape-induced capillary interactions of colloidal particles, EPL 72 (4) (2005) 671.

[83] B. Madivala, J. Fransaer, J. Vermant, Self-assembly and rheology of ellipsoidal particles at interfaces, Langmuir 25 (5) (2009) 2718–2728.

[84] R. Aveyard, B. P. Binks, J. H. Clint, Emulsions stabilised solely by colloidal particles, Adv. Colloid Interface Sci 100–102 (2003) 503 – 546.

[85] A. W. Adamson, A. P. Gast, Physical chemistry of surfaces, Wiley, New York, NY, USA, 1997.

[86] D. Ershov, J. Sprakel, J. Appel, M. A. Cohen Stuart, J. van der Gucht, Capillarity-induced ordering of spherical colloids on an interface with anisotropic curvature, Proc. Natl. Acad. Sci. USA 110 (23) (2013) 9220–9224.

[87] A. Tao, P. Sinsermsuksakul, P. Yang, Tunable plasmonic superlattices of silver nanocrystals, Nat. Nanotechnol 2 (435).

[88] K. D. Danov, P. A. Kralchevsky, Capillary forces between particles at a liquid interface: General theoretical approach and interactions between capillary multipoles, Adv. Colloid Interface Sci 154 (1–2) (2010) 91 – 103.

[89] A. Domínguez, M. Oettel, S. Dietrich, Force balance of particles trapped at fluid interfaces, The Journal of Chemical Physics 128 (11) (2008) 114904.

[90] B. J. Park, T. Brugarolas, D. Lee, Janus particles at an oil-water interface, Soft Matter 7 (2011) 6413–6417.

[91] E. P. Lewandowski, J. A. Bernate, P. C. Searson, K. J. Stebe, Rotation and alignment of anisotropic particles on nonplanar interfaces, Langmuir 24 (17) (2008) 9302–9307.

[92] A. Würger, Curvature-induced capillary interaction of spherical particles at a liquid interface, Phys. Rev. E 74 (2006) 041402.

[93] J. Léandri, A. Würger, Trapping energy of a spherical particle on a curved liquid interface, J. Colloid Interface Sci. 405 (2013) 249–255.

[94] P. Galatola, J.-B. Fournier, Capillary force acting on a colloidal particle floating on a deformed interface, Soft Matter 10 (2014) 2197–2212.

[95] B. J. Park, E. M. Furst, Attractive interactions between colloids at the oil-water interface, Soft Matter 7 (2011) 7676–7682.

[96] B. J. Park, J. Vermant, E. M. Furst, Heterogeneity of the electrostatic repulsion between colloids at the oil-water interface, Soft Matter 6 (2010) 5327–5333.

[97] S. Razavi, I. Kretzschmar, J. Koplik, C. E. Colosqui, Nanoparticles at liquid interfaces: Rotational dynamics and angular locking, J. Chem. Phys. 140 (1) (2014) 014904.

[98] H.Lamb, Hydrodynamics, Dover Publications, 1945.

[99] H. Brenner, Effect of finite boundaries on the stokes resistance of an arbitrary particle, Journal of Fluid Mechanics 12 (1) (1962) 35–48.

[100] L. Yao, N. Sharifi-Mood, I. B. Liu, K. J. Stebe, Capillary migration of microdisks on curved interfaces, J. Colloid Interface Sci. 449 (2015) 436 – 442.

[101] F. Gibbs, S. Kermasha, I. Alli, C. N. B. Mulligan, Encapsulation in the food industry: a review, Int. J. Food. Sci. Nutr. 50 (1999) 213–224.

[102] R. G. Willaert, G. V. Baron, Gel entrapment and micro-encapsulation: methods, aapplications and engineering principles, Rev. Chem. Eng. 22 (1996) 1–205.

[103] A. Bhargava, A. Francis, B. A.K., Interfacial studies related to the recovery of mineral slimes in a water—hydrocarbon liquid-collector system, J. Colloid Interface Sci. 64 (1978) 214 – 227.

[104] A. P. Sullivan, P. K. Kilpatrick, The effects of inorganic solid particles on water and crude oil emulsion stability, Ind. Eng. Chem. Res. 41 (2002) 3389–3404.

[105] T. Young, An essay on the cohesion of fluids, Phil. Trans. R. Soc. Lond. 95 (1805) 65–87.

[106] E. J. Hinch, Perturbation methods, Cambridge University Press, New York, NY, USA, 1991.

[107] A. H. Nayfeh, Purturbation methods, Wiley, New Yrok, NY, USA, 2000.

[108] N. Sharifi-Mood, I. B. Liu, K. J. Stebe, Curvature capillary migration of microspheres, Soft Matter 11 (2015) 6768–6779.

[109] A. J. Goldman, R. G. Cox, H. Brenner, The slow motion of two identical arbitrarily oriented spheres through a viscous fluid, Chem. Eng. Sci. 21 (1966) 1151 – 1170.

[110] I. B. Liu, N. Sharifi-Mood, K. J. Stebe, Curvature-driven assembly in soft matter, Phil. Trans. R. Soc. A 374 (2072).

[111] D. J. Griffiths, Introduction to electrodynamics, 3rd Edition, Prentice Hall, Upper Saddle River, New Jersey, USA, 1999.

[112] N. Sharifi-Mood, I. B. Liu, K. J. Stebe, Reply to the comments on ”curvature capillary migration of microspheres” by P. Galatola and A. Wurger, Soft Matter 12 (2016) 333–336.

[113] W.-S. Wei, M. A. Gharbi, M. A. Lohr, T. Still, M. D. Gratale, T. C. Lubensky, K. J. Stebe, A. G. Yodh, Dynamics of ordered colloidal particle monolayers at nematic liquid crystal interfaces, Soft Matter 12 (2016) 4715–4724.

[114] I. B. Liu, N. Sharifi-Mood, K. J. Stebe, Capillary driven assembly on liquid surfaces, Annual Review of Condensed Matter Physics.

[115] V. N. Manoharan, Colloids at interfaces: Pinned down, Nat. Mater. 14 (9) (2015) 869–870.

[116] J. F. Trahan, R. G. Hussey, R. P. Roger, The velocity of a circular disk moving edgewise in quasi-steady stokes flow toward a plane boundary, Phys Fluids 11 (9) (1999) 2463–2470.

[117] M. M. Nicolson, The interaction between floating particles, Math Proc Cambridge 45 (2) (1949) 288–295.

[118] D. Wong, I. B. Liu, E. B. Steager, K. J. Stebe, V. Kumar, Directed micro assembly of passive particles at fluid interfaces using magnetic robots, in: 2016 International Conference on Manipulation, Automation and Robotics at Small Scales (MARSS), 2016, pp. 1–6.

[119] P. Poulin, H. Stark, T. C. Lubensky, D. A. Weitz, Novel colloidal interactions in anisotropic fluids, Science 275 (5307) (1997) 1770–1773.

[120] U. Ognysta, A. Nych, V. Nazarenko, M. Škarabot, I. Muševič, Design of 2D binary colloidal crystals in a nematic liquid crystal, Langmuir 25 (20) (2009) 12092–12100.

[121] C. P. Lapointe, T. G. Mason, I. I. Smalyukh, Shape-controlled colloidal interactions in nematic liquid crystals, Science 326 (5956) (2009) 1083–1086.

[122] I. Muševič, M. Škarabot, U. Tkalec, M. Ravnik, S. Žumer, Two-dimensional nematic colloidal crystals self-assembled by topological defects, Science 313 (5789) (2006) 954–958.

[123] S. Sacanna, D. J. Pine, Shape-anisotropic colloids: Building blocks for complex assemblies, Curr. Opin. Colloid Interface Sci 16 (2) (2011) 96 – 105.

[124] R. Stannarius, Liquid crystals: More than display fillings, Nat. Mater. 8 (8) (2009) 617–618.

[125] O. D. Lavrentovich, Transport of particles in liquid crystals, Soft Matter 10 (2014) 1264–1283.

[126] C. Blanc, D. Coursault, E. Lacaze, Ordering nano- and microparticles assemblies with liquid crystals, Liq. Cryst. Rev. 1 (2) (2013) 83–109.

[127] P.-G. D. Gennes, J. Prost, The physics of liquid crystals, Oxford University Press, 1993.

[128] M. Škarabot, M. Ravnik, S. Žumer, U. Tkalec, I. Poberaj, D. Babič, N. Osterman, I. Muševič, Interactions of quadrupolar nematic colloids, Phys. Rev. E 77 (2008) 031705.

[129] U. Tkalec, I. Muševič, Topology of nematic liquid crystal colloids confined to two dimensions, Soft Matter 9 (2013) 8140–8150.

[130] D. A. Beller, M. A. Gharbi, I. B. Liu, Shape-controlled orientation and assembly of colloids with sharp edges in nematic liquid crystals, Soft Matter 11 (2015) 1078–1086.

[131] M. A. Gharbi, M. Cavallaro, G. Wu, D. A. Beller, R. D. Kamien, S. Yang, K. J. Stebe, Microbullet assembly: interactions of oriented dipoles in confined nematic liquid crystal, Liq. Cryst 40 (12) (2013) 1619–1627.

[132] S. M. Hashemi, M. R. Ejtehadi, Equilibrium state of a cylindrical particle with flat ends in nematic liquid crystals, Phys. Rev. E 91 (2015) 012503.

[133] C. Lapointe, A. Hultgren, D. M. Silevitch, E. J. Felton, D. H. Reich, R. L. Leheny, Elastic torque and the levitation of metal wires by a nematic liquid crystal, Science 303 (5658) (2004) 652–655.

[134] M. Cavallaro Jr, M. A. Gharbi, D. A. Beller, S. Čopar, Z. Shi, R. D. Kamien, S. Yang, T. Baumgart, K. J. Stebe, Ring around the colloid, Soft Matter 9 (2013) 9099–9102.

[135] U. Tkalec, M. Škarabot, I. Muševič, Interactions of micro-rods in a thin layer of a nematic liquid crystal, Soft Matter 4 (2008) 2402–2409.

[136] B. Senyuk, Q. Liu, S. He, R. D. Kamien, R. B. Kusner, T. C. Lubensky, I. I. Smalyukh, Topological colloids, Nature 493 (7431) (2013) 200–205.

[137] M. A. Gharbi, M. Nobili, M. In, G. Prevot, P. Galatola, J.-B. Fournier, C. Blanc, Behavior of colloidal particles at a nematic liquid crystal interface, Soft Matter 7 (2011) 1467–1471.

[138] M. A. Gharbi, M. Nobili, C. Blanc, Use of topological defects as templates to direct assembly of colloidal particles at nematic interfaces, J. Colloid Interface Sci. 417 (0) (2014) 250 – 255.

[139] P. A. Kralchevsky, N. D. Denkov, Capillary forces and structuring in layers of colloid particles, Curr. Opin. Colloid Interface Sci 6 (4) (2001) 383 – 401.

[140] M. Grzelczak, J. Vermant, E. M. Furst, L. M. Liz-Marzán, Directed self-assembly of nanoparticles, ACS Nano 4 (7) (2010) 3591–3605.

[141] J. Dobnikar, A. Snezhko, A. Yethiraj, Emergent colloidal dynamics in electromagnetic fields, Soft Matter 9 (2013) 3693–3704.

[142] T. D. Edwards, M. A. Bevan, Controlling colloidal particles with electric fields, Langmuir 30 (36) (2014) 10793–10803.

[143] M. Tintaru, R. Moldovan, T. Beica, S. Frunza, Surface tension of some liquid crystals in the cyanobiphenyl series, Liq. Cryst 28 (5) (2001) 793–797.

[144] E. P. Lewandowski, P. C. Searson, K. J. Stebe, Orientation of a nanocylinder at a fluid interface, J. Phys. Chem. B 110 (9) (2006) 4283–4290.

[145] I. I. Smalyukh, Liquid crystals enable chemoresponsive reconfigurable colloidal self-assembly, Proc. Natl. Acad. Sci. 107 (9) (2010) 3945–3946.

[146] G. M. Koenig, I.-H. Lin, N. L. Abbott, Chemoresponsive assemblies of microparticles at liquid crystalline interfaces, Proc. Natl. Acad. Sci. 107 (9) (2010) 3998–4003.

[147] A. Ortega, J. Garca de la Torre, Hydrodynamic properties of rodlike and disklike particles in dilute solution", J. Chem. Phys. 119 (18) (2003) 9914–9919.

[148] M. Kleman, O. D. Lavrentovich, Soft matter physics: An introduction, Springer Verlag, 2002.